E-760

UNIVERSITY OF CALIFORNIA

IRVINE

Two Body Electromagnetic Final States Produced in Antiproton-Proton Annihilations

DISSERTATION

submitted in partial satisfaction of the requirements for the degree of

DOCTOR OF PHILOSOPHY

in Physics

by

Daniel Robert Broemmelsiek

Dissertation Committee:

Professor Jonas Schultz, Chair

Professor Mark Mandelkern

Professor Herbert Hamber

1995

AAE2676

© 1995 by DANIEL ROBERT BROEMMELSIEK

All rights reserved.

The dissertation of Daniel Robert Broemmelsiek is approved,

and is acceptable in quality and form

for publication on microfilm:

_____

_____

_____

Committee Chair

University of California, Irvine

1995

Contents

List of Figures v

List of Tables vi

Acknowledgements viii

Curriculum Vitae ix

Abstract xi

Chapter 1 Historical Foundations and Physical Motivation 1
- 1.1 Previous Experiments 2
- 1.2 E760 Experimental Method 4
- 1.3 Charmonium 5
- 1.4 Exclusive Final States 13

Chapter 2 Experimental Apparatus 17
- 2.1 Fermi National Accelerator Laboratory 17
- 2.2 The Antiproton Source 19
  - 2.2.1 Accelerator Physics 21
  - 2.2.2 Deceleration of Antiprotons 27
  - 2.2.3 Beam Energy Measurement 29
- 2.3 E760 Detector 32
  - 2.3.1 Gas Jet Target 33
  - 2.3.2 Luminosity Monitor 35
  - 2.3.3 Charged Tracking 37
  - 2.3.4 Calorimetry 40

Chapter 3 Data Acquisition Hardware and Logic 51
- 3.1 Readout Electronics 52
- 3.2 Trigger Electronics 55
  - 3.2.1 The Gatemaster 55
  - 3.2.2 The Memory Lookup Unit 57
- 3.3 Detector Level Logic 58
- 3.4 Trigger Level Logic 59

Chapter 4 Neutral Event Selection and Efficiencies **63**
4.1 The Data 63
4.2 Selecting Events 64
4.2.1 CCAL Requirements 65
4.2.2 Background Rejection 66
4.2.3 Kinematical Consistency 70
4.3 Efficiencies 71
4.3.1 Selection Efficiencies 71
4.3.2 Trigger Efficiencies 75

Chapter 5 Background Estimation and Likelihood Analysis **79**
5.1 Measurement of The $\pi^0\pi^0$ and $\pi^0\gamma$ Differential Cross Sections 80
5.2 The $\gamma\gamma$ Background Differential Cross Section 83
5.3 Extended Maximum Likelihood and Fiducial Limits 86
5.3.1 What is EMLM? 87
5.3.2 Background Estimates in the EMLM 90
5.3.3 A Total Error on The Expected Signal 93
5.4 Background Estimation and Systematic Errors 94
5.4.1 CCAL Energy Threshold 95
5.4.2 $\pi^0\gamma$ Asymmetries 96
5.4.3 Development of The Error Matrix 99
5.5 Results for Fiducial Limits 101
5.6 Likelihood Function 102
5.6.1 η_c Resonance and $\gamma\gamma$ Continuum 105
5.6.2 η_c Resonance 106
5.6.3 Goodness-of-Fit 111

Chapter 6 Charged Event Selection and Likelihood Analysis . . . **113**
6.1 The Data 113
6.2 Selecting Events 114
6.3 Detection Efficiencies 116
6.3.1 H2 Detection Efficiency 117
6.3.2 Čerenkov Detection Efficiency 119
6.3.3 Hodoscope Multiplicities 121
6.3.4 PBG and Coplanarity Efficiencies 122
6.4 Trigger Efficiency 123
6.5 Backgrounds 123
6.5.1 Hadronic Rejection Factor 124
6.5.2 Estimation of $\pi^+\pi^-$ Background Cross Section 127
6.5.3 Tails of The J/ψ Distribution 132
6.5.4 Two Photon Conversions 133
6.6 Results and Likelihood Analysis 133

Chapter 7 Inferences and Comparisons **137**
7.1 η_c Results 137
7.2 Exclusive Electromagnetic Final States 141
7.3 Comparison of Exclusive Electromagnetic Final States 143

Bibliography **145**

List of Figures

1.1 Charmonium Spectrum 6
1.2 Diagrams for $c\bar{c} \to 2\gamma$ or 2 gluons. 10

2.1 Fermilab Footprint 18
2.2 Betatron Oscillations 23
2.3 Orbit Differential 25
2.4 E760 Detector 34
2.5 Luminosity Monitor 36
2.6 Moveable Base for Luminosity Monitor 36
2.7 Čerenkov Detector 39

3.1 Trigger Detector Coincidence for Charged Tracks 59

4.1 Invariant Mass Combinations, I 68
4.2 Invariant Mass Combinations, II 69
4.3 H1 Multiplicities 73
4.4 FCAL Multiplicities 74

5.1 $\gamma\gamma$ Background for $\sqrt{s} = 3097$ MeV 85
5.2 CCAL Threshold Error 97
5.3 Signed $\pi^0\gamma$ Asymmetries 98
5.4 $\pi^0\gamma$ Asymmetry Ideogram 100
5.5 Plot of Total Error vs. $|\cos(\vartheta^*)|$ 103
5.6 $B(\eta_c \to \gamma\gamma)$ vs. $\Gamma_{\gamma\gamma}$ Contours 108
5.7 $\Gamma_{\gamma\gamma}$ vs. M_R Contours 109
5.8 $B(\eta_c \to \gamma\gamma)$ vs. M_R Contours 110
5.9 Measured σ_{η_c} vs. E_{cm} with Fitted Lineshape 111

6.1 One Electron Detection Efficiency 120
6.2 Two Electron Detection Efficiency 120
6.3 Akinematic Variable for e^+e^- Final State 125
6.4 CCAL Hadronic Response 126
6.5 Scaled Differential Cross Sections for $\bar{p}p \to \pi^+\pi^-$ 130
6.6 Combined Scaled Differential Cross Sections for $\bar{p}p \to \pi^+\pi^-$ 131

7.1 η_c Mass Comparisons 139
7.2 η_c Partial Width Comparisons 140
7.3 $q^4|G_M|/\mu_p$ vs q^2 142

List of Tables

2.1 Accumulator Beam Momenta 20
2.2 Accumulator Devices 28
2.3 F2 Type Lead Glass 43
2.4 Block Dimensions and Positions 44
2.5 Photomultiplier Characteristics 45
2.6 CCAL Summing Pattern 45
2.7 CCAL Clustering Parameters 48

3.1 CAMAC Hardware Organization 52
3.2 VME Crate Configuration 54
3.3 Gatemaster Module Inputs 56
3.4 MLU Module Inputs 61
3.5 Trigger Readout 62

4.1 η_c Energies and Luminosities 64
4.2 Neutral Selection Efficiencies 72
4.3 Neutral Trigger Efficiencies 75

5.1 $\gamma\gamma$ Background Polynomials 84
5.2 η_c PDG Resonance Parameters 102
5.3 $\gamma\gamma$ Fiducial Volumes 104
5.4 η_c Resonance Parameters and $\gamma\gamma$ Continuum, I 106
5.5 η_c Resonance Parameters and $\gamma\gamma$ Continuum, II 106
5.6 Correlation Coefficients, I 107
5.7 Correlation Coefficients, II 107
5.8 η_c Resonance Parameters 107
5.9 K-S Test for η_c Fit 112

6.1 Charged Data Sample 114
6.2 Selected e^+e^- Events 116
6.3 Arm Topology Efficiency 119
6.4 Čerenkov Detection Efficiencies 120
6.5 Detector Level Logic 122
6.6 Trigger Level Logic 123
6.7 Pion Rejection Factors 127
6.8 $d\sigma/d(\cos\vartheta^*)$ for $\bar{p}p \to \pi^+\pi^-$, and $s = 6.42$ GeV^2 128
6.9 $d\sigma/d(\cos\vartheta^*)$ for $\bar{p}p \to \pi^+\pi^-$, and $s = 11.307$ GeV^2 129
6.10 $d\sigma/d(\cos\vartheta^*)$ for $\bar{p}p \to \pi^+\pi^-$, and $s = 13.546$ GeV^2 130

6.11 E760 Results for J/ψ 132
6.12 Measured Results for e^+e^- Events 134
6.13 E.M.L. Results for e^+e^- Events 136

7.1 Complete η_c Results 138
7.2 Strong Coupling Constant, $\alpha_s(m_c)$ 140

Acknowledgements

This work could not have been accomplished without the efforts of the E760 collaboration. Where possible, I have tried to cite specific people and results. Many of these citations are necessarily internal collaboration documents and can be found on file at the Fermilab Physics Department. The people working and living at Fermilab, and the E760 collaborators in particular, have taught me that experimental physics is a human endeavor fraught with all the familiar pitfalls.

During my stay at Fermilab, Dr. Michael Church put me to work. I was fortunate to be assigned, what I consider, some of the most interesting work available to a student member of the E760 collaboration. For this, and Dr. Church's friendship, I am grateful.

Professor Jonas Schultz deserves and receives my highest regard. I gladly add my testimonial to the numerous accolades Professor Schultz has received for his teaching abilities and his work as a professional physicist. I am sincerely honored to be one of his students.

This work was supported by Department of Energy grant DE-FG03-91ER40679 task B.

Curriculum Vitae

Daniel R. Broemmelsiek

1995 Ph.D. in Physics, University of California, Irvine
Dissertation: *Two Body Electromagnetic Final States Produced in Antiproton-Proton Annihilations*
Professor Jonas Schultz, Chair

1987 M.S. in Mathematics Louisiana State University, Baton Rouge

1985 B.S. in Physics, Louisiana State University, Baton Rouge

Publications

"Study of the $\eta_c(1^1S_0)$ State of Charmonium Formed in $\bar{p}p$ Annihilations and a Search for the $\eta_c'(2^1S_0)$ "
The E760 Collaboration (T.A. Armstrong *et al.*), *in preparation.*

"Study of the angular distribution of the reaction $\bar{p}p \to \chi_{c,2} \to J/\psi\gamma \to e^+e^-\gamma$"
The E760 Collaboration (T.A. Armstrong *et al.*), *Physical Review* D48, 3037 (1993).

"Production of the $f_2(1520)$ resonance in antiproton-proton annihilations at $\sqrt{s} = 2980$ and 3526 MeV"
The E760 Collaboration (T.A. Armstrong *et al.*), *Physics Letters* B307 (1993) 399-402.

"Evidence for $\eta\eta$ resonances in antiproton-proton annihilations at $2950 < \sqrt{s} < 3620$ MeV"
The E760 Collaboration (T.A. Armstrong *et al.*), *Physics Letters* B307 (1993) 394-398.

"Measurement of the $\gamma\gamma$ Partial Width of the χ_2 Charmonium Resonance"
The E760 Collaboration (T.A. Armstrong *et al.*), *Physical Review Letters* 70, 2988 (1993).

"Proton Electromagnetic Form Factors in the Time-Like Region from 8.9 to 13.0 GeV^2"
The E760 Collaboration (T.A. Armstrong *et al.*), *Physical Review Letters* 70, 1212 (1993).

"Measurement of the J/ψ and ψ' Resonance Parameters in $\bar{p}p$ Annihilation"
The E760 Collaboration (T.A. Armstrong *et al.*), *Physical Review* D47, 772 (1993).

"Observation of the $^1P_1$ State of Charmonium"
The E760 Collaboration (T.A. Armstrong *et al.*), *Physical Review Letters* 69, 2337 (1992).

"Precision Measurements of Charmonium States Formed in $\bar{p}p$ Annihilation"
The E760 Collaboration (T.A. Armstrong *et al.*), *Phys. Rev. Lett.* 68(1992)1468.

"Study of the χ_1 and χ_2 charmonium states formed in $\bar{p}p$ annihilations"
The E760 Collaboration (T.A. Armstrong *et al.*), *Nucl. Phys.* B373(1992)35.

"A technique for measuring the beam energy of the Fermilab Antiproton Accumulator and a determination of the proton electromagnetic form factor at $|q^2| = 12.4$ GeV/c^2"
The E760 Collaboration (presented by D.R. Broemmelsiek), 1992 Joint April Meeting of the American Physical Society and the American Association of Physics Teachers, Washington, D.C., *Bulletin of the American Physical Society* 37(1992)867.

"The E760 Lead Glass Central Calorimeter: Design and Initial Test Results"
L. Bartoszek *et al.*, *Nucl. Instrum. Meth.* A301(1991)47.

Abstract of the Dissertation

Two Body Electromagnetic Final States Produced in Antiproton-Proton Annihilations

by

Daniel Robert Broemmelsiek

Doctor of Philosophy in Physics

University of California, Irvine, 1995

Professor Jonas Schultz, Chair

Fermilab Experiment 760 (E760) is designed to study proton-antiproton interactions using a hydrogen gas-jet target in the Fermilab Antiproton Accumulator ring. The E760 detector is optimized for the detection of electromagnetic final states and the antiproton beam energy and width are precisely measured. In this thesis, the reactions $\bar{p}p \rightarrow \eta_c(^1S_0) \rightarrow \gamma\gamma$, $\bar{p}p \rightarrow \gamma\gamma$, and $\bar{p}p \rightarrow e^+e^-$ are studied.

The mass of the η_c resonance and the decay width into two photons are found to be $2988.1^{+3.1}_{-2.6}$ MeV/c^2 and $6.9^{+2.3}_{-1.6} \pm 2.3$ KeV respectively. The $\gamma\gamma$ final state continuum cross section is found to be $\sigma(|\cos(\vartheta^*)| \leq 0.030) < 29$ pb. The e^+e^- final state continuum cross section for s =8.82, 12.43, and 12.85 (GeV)^2 is found to be $\sigma_{\text{total}} = 6.5^{+2.3}_{-1.8}$, $1.5^{+0.5}_{-0.3}$, and $2.0^{+.9}_{-0.7}$ pb respectively.

Chapter 1

Historical Foundations and Physical Motivation

With the advent of high energy proton accelerators, many previously unassailable topics in particle physics came within the scope of experimental science. The development of Stochastic Cooling [1], which made collection of antiprotons feasible, expanded an already broad experimental program studying the standard model of particle physics and, in particular, the strong interaction.

While the success of the standard model is amazing, several fundamental questions involving the strong interaction remain. The generally accepted theory of the strong interaction is quantum chromodynamics (QCD). In the QCD Lagrangian the basic coupling g is dimensionless. When vacuum polarization corrections to the quark gluon coupling are calculated, the result diverges and the renormalization procedure is forced to introduce a scale into the definition of the effective coupling. The strong coupling then depends on the scale relevant to the QCD subprocess. The effective coupling is written to first order as

$$\alpha_s(Q^2) = \frac{4\pi}{\beta_0 \ln(Q^2/\Lambda^2)} \tag{1.1}$$

where Λ is the renormalization scale and $\beta_0 = 11 - \frac{2}{3}n_f$ with n_f the number of quark flavors available to the QCD subprocess. As $Q^2 \to \infty$ the coupling

approaches zero making the quarks asymptotically free. The magnitude of Λ can be expected to be set by the size of a typical hadron. Taking the proton radius as ~ 1 fm, Λ is found to be ~ 200 MeV. This magnitude for Λ is also indicated by deep inelastic scattering experiments and Υ annihilation rates.

Since the strong coupling is small in the large Q^2 limit, perturbation theory can be expected to make reliable predictions. In the low Q^2 limit, the interaction of gluons with one another leads to an increase of the strong coupling. This and the lack of experimental evidence for free quarks leads to the concept of confinement of quarks to colorless hadrons. Critical tests of the non-perturbative or confining aspects of QCD must involve lower energies and momentum transfers than the perturbative aspects such as asymptotic freedom and parton distribution functions.

Antiproton-proton annihilations provide an important test bed for QCD. Measurement of exclusive electromagnetic final states, $\gamma\gamma$ and e^+e^-, at the intermediate energies available in this experiment address both perturbative and non-perturbative aspects of QCD. A brief historical interlude will put this experiment along with the theoretical predictions addressed in proper perspective.

1.1 Previous Experiments

Within the Weinberg-Salam formalism [2] of the weak interactions, first introduced in 1967-68, the predictions for strangeness changing weak neutral currents were too large. A solution to this problem was proposed by Glashow, Iliopoulos, and Maiani [3]. A new "charmed" quark, c, with weak isospin partner $s_\theta = s\cos\theta_C - d\sin\theta_C$, where θ_C is the Cabbibo angle, was proposed to make the hadronic neutral current diagonal with respect to quark flavors. With the discovery of the J/ψ vector meson [4, 5] and the subsequent evidence for the ψ' with radiative

transitions [6, 7, 8] to several metastable states having properties compatible with states of bound fermions, and a spectrum of charmed mesons, a new quark with mass ~ 1.5 GeV/c^2 was confirmed.

The J/ψ vector meson was initially observed in the energy dependence of the cross section for $e^+e^- \rightarrow$hadrons at SPEAR [4] and the e^+e^- invariant mass distribution from the reaction $p + Be \rightarrow e^+e^-X$ at Brookhaven [5]. Until the advent of Stochastic Cooling and antiproton storage rings, subsequent formation experiments at e^+e^- colliders were limited to the $J^{PC} = 1^{--}$ resonant states of charmonium. The masses of the $J^{PC} = 1^{--}$ states in e^+e^- collisions are directly related to the beam energy, whereas the measured masses and widths of the other resonant states depend on the detector resolutions.

The idea of charmonium formation by antiproton-proton annihilation was first put forward by P. Dalpiaz [9]. With a minimum of 2 or 3 gluons in the intermediate state, any J^{PC} combination allowed for a fermion-antifermion system can be formed in strong proton-antiproton annihilations. Thus, the mass and width of each resonance produced is determined directly from the beam energy and width measurements. Experiment R704 [10] at the CERN ISR was the first experiment to demonstrate this technique. R704, a two arm spectrometer optimized for the detection of electromagnetic final states, operated in the spring of 1984. With only a few weeks of efficient data taking before the ISR was permanently closed, significant results from R704 justified the building of a new detector at the only remaining source of antiprotons.

1.2 E760 Experimental Method

The Fermilab Antiproton Source provides an antiproton beam with precise knowledge of the beam energy and energy spread. An internal molecular hydrogen gas jet [11] is the fixed target. The beam and target provide instantaneous luminosities of 10^{-30} cm^{-2}·s^{-1} and a small interaction region, $\sim$1 cm^3. The detector for Fermilab Experiment 760 (E760) is a cylindrically symmetric large acceptance non-magnetic spectrometer. The detector design stresses the detection of electrons and photons. In this way, the electromagnetic final states of charmonium can be distinguished from the large hadronic part of the proton antiproton interaction cross section. Further details of the Fermilab Antiproton Source and the E760 detector are provided in Chapter 2.

With such a well defined initial state, spectroscopy becomes almost trivial. A plot of the cross section versus the center of mass energy yields an excitation curve which is the convolution of the Breit-Wigner resonance and the beam profile. The width of the beam profile is comparable to the ψ' total width. Except for the J/ψ and ψ' resonances, deconvolution of the resonance line shape is straightforward. In the case of the η_c resonance, Chapter 5, the beam profile is nearly 2 orders of magnitude less than the resonance width so that unfolding the beam energy profile does not affect the resonance parameter results. The cross sections are measured by using the E760 detector to count the number of events which satisfy a particular final state at each energy. Independent total luminosity measurements are based on forward elastic scattering of antiprotons and are used to scale the number of events.

For exclusive non-resonant or continuum electromagnetic final states, the interesting measurements are the differential and total cross sections. While E760 was able to collect 30 pb^{-1} during 1991, only $\sim$ 1 pb^{-1} was taken at any beam

energy setting. Due to the small total cross sections involved, ≤ 10 pb, the data from several runs are grouped together to improve the statistics for the e^+e^- non-resonant final state, Chapter 6. An upper limit on the $\gamma\gamma$ continuum cross section is given for the data taken during the η_c resonance scan, Chapter 5.

1.3 Charmonium

Charmonium spectroscopy and decay widths are successfully described in the context of non-relativistic $c\bar{c}$ potential models [12]. This idea is based on the observation that quarks should form positronium-like bound states if their mass is much larger than the perturbative QCD scale Λ [13]. The asymptotic behaviour of the potential is determined by quark confinement at large distances and asymptotic freedom at short $c\bar{c}$ separations,

$$r \gg \frac{1}{\Lambda} \quad V(r) \sim kr \text{ and } r \ll \frac{1}{\Lambda} \quad V(r) \sim -\frac{4}{3}\frac{\alpha_s(r)}{r},$$

where $\alpha_s(r)$ is the running strong coupling constant evaluated at a mass scale appropriate to the $c\bar{c}$ separation and k a spring constant. The structure of the charmonium spectrum, Figure 1.1, is qualitatively somewhere between a Coulomb potential, $V(r) \sim \frac{1}{r}$, and a harmonic oscillator spectrum, $V(r) \sim r^2$. The "Cornell Potential" [12],

$$V(r) = -\frac{4}{3}\frac{\alpha_s(r)}{r} + kr\,,$$

where k is a free parameter determined by fits to the charmonium spectrum, incorporates these phenominological considerations. The parameters of this model are $(4/3)\alpha_s(r) = 0.19 =$ const., k=$(1/1.95)^2$ GeV^2, and the charm quark mass, $m_c = 1.85$ GeV/c^2.

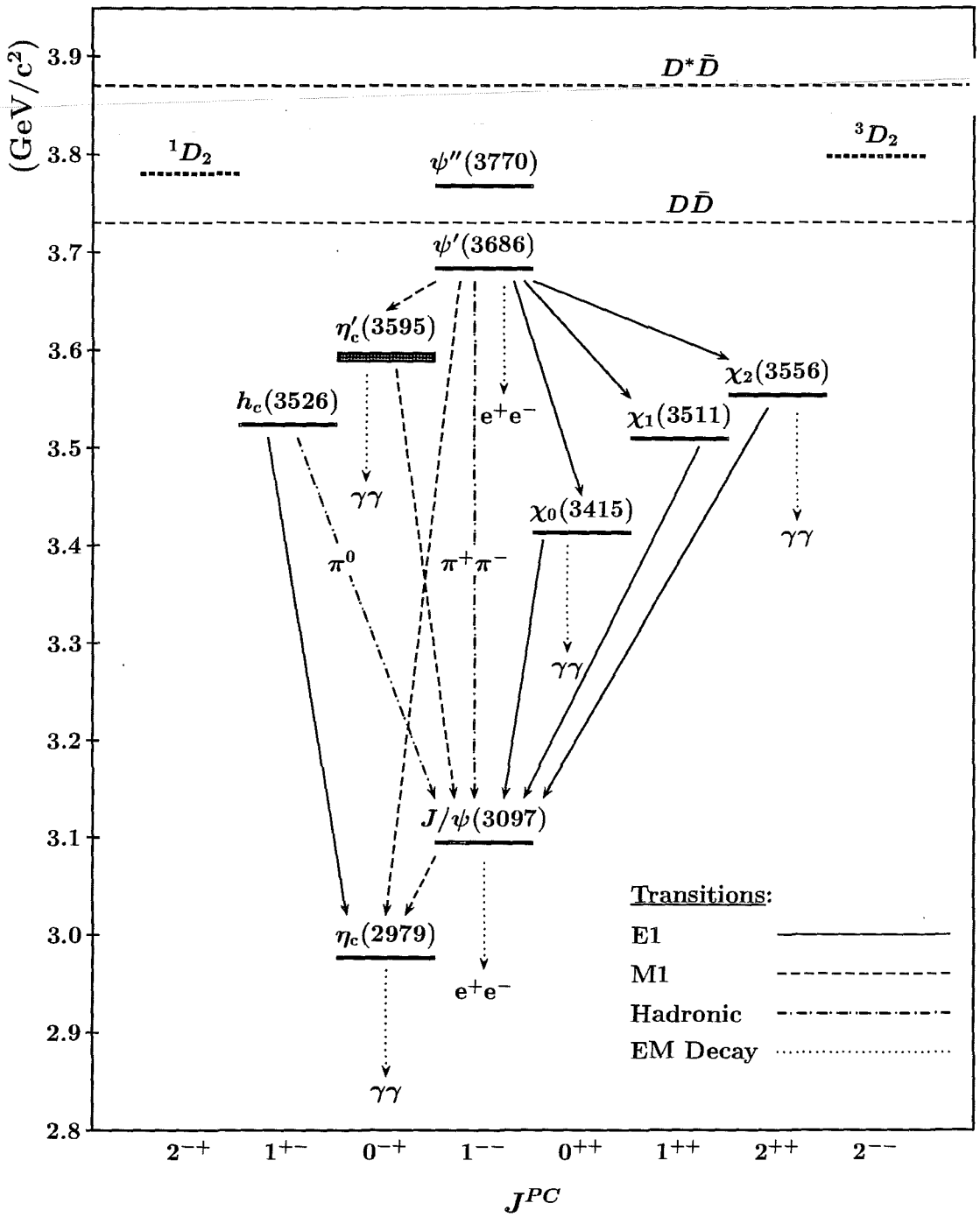

Figure 1.1: Charmonium Spectrum

For any fermion-antifermion system, the parity and charge conjugation quantum numbers are given by

$$P = (-1)^{L+1} \quad \text{and} \quad C = (-1)^{L+S}$$

where L and S are the total angular momentum and spin quantum numbers. In addition to the standard spectroscopic notation, $n^{2S+1}J_L$, where $\vec{J} = \vec{L} + \vec{S}$ and n is the principal quantum number, the resonances can be characterized by the notation J^{PC}, Figure 1.1.

Consideration of the virial theorem in the form

$$2 < T > = < \vec{r} \cdot \vec{\nabla} V(\vec{r}) > ,$$

where $< T >$ is the expectation of the kinetic energy, will lead to an estimate of the velocity scales in charmonium. Supposing that the linear term of the "Cornell Potential" dominates at the length scale of the charmonium systems, the immediate conclusion is that $2 < T > = < V >$. Using $E = < T > + < V >$, the average kinetic energy is proportional to the total energy of the system. The non-relativistic expression for the kinetic energy, $< T > = 2 \times 1/2\, m_c < v^2 >$, gives a rough estimate of the velocity scale as $< v^2 > = E/3m_c$. With a charm quark mass of 1.85 GeV/c^2 and the binding energy of the $c\bar{c}$ potential approximated by the mass difference $M_{\psi'} - M_{J/\psi} \approx 589 MeV$, a rough estimate of the average square velocity is $< v^2 > \sim 0.11c^2$. A non-relativistic approach will, in large part, describe the principle features of the charmonium spectrum. Analogous to the Hydrogen atom, the fine and hyperfine structures are calculated from the spin-spin, spin-orbit, and tensor interactions which are found by taking a non-relativistic limit of the relativistic Hamiltonian [14]. Such potential model approaches give phenomenological understanding of $q\bar{q}$ or quarkonia systems. Precision measurements of the charmonium spectrum by E760 have not only refined potential

models, but have helped to stimulate progress in theoretical QCD calculations. In particular, lattice QCD and effective field theories have benefitted from the challenge of describing these precision measurements.

Mass Spectrum

While potential models will give phenomenological descriptions of the QCD potential, lattice field theory offers a systematic first principles approach to solving QCD [15]. Lattice QCD calculations begin with a formulation of an action representing the QCD fields. Formulation of a QCD action suitable for lattice calculations is the realm of effective field theories which are used primarily for calculational convenience. However, lattice QCD calculations of quarkonia, and charmonium in particular, have yielded accurate determinations of the strong coupling and heavy quark masses [16, 17].

One method for determining a quark mass is done by tuning the bare lattice quark mass so that the observed J/ψ mass is reproduced. By comparing lattice QCD results with the potential models for the charmonium spectrum, the systematic errors involved in lattice calculations may be estimated. Several systematic effects associated with the complete or partial exclusion of the sea quark content of the $c\bar{c}$ bound state have yet to be studied fully. Sea quark effects are expected to explain some of the differences between the observed charmonium mass spectrum and that calculated on the lattice. Recently, the inclusion of vacuum polarization [17] due to light quarks into the effective field theory describing the QCD action has reduced the systematic error in the charmonium mass spectrum calculation. Simulation costs have also been reduced.

There are two steps in a determination of the coupling constant. The first is to determine accurately the lattice spacing. Spin-averaged mass splittings, 1P-1S and 2S-1S, have been identified as quantities insensitive to lattice-spacing errors. Demanding that the calculated mass splittings reproduce the observed splittings sets the lattice spacing in physical units. Comparison with the perturbative expansion for the same quantity fixes the coupling.

Accurate predictions of the charmonium mass spectrum have direct implications for future charmonium formation experiments. The η_c' resonance has yet to be confirmed and accurate predictions of the η_c' mass will enable the efficient use of available luminosity. Measurements of the strong coupling at any momentum scale are of general interest.

Decay Rates

The dominant decays of charmonium are electromagnetic and hadronic. Weak effects would give rise to decays via, for example, an intermediate Z^0 boson, the weak decay of one or both constituent quarks, or t-channel W exchange. These effects become more important for larger quark masses and are irrelevant for charmonium [18].

Decay rates for non-relativistic fermion-antifermion systems involve only the wave function or its higher derivatives evaluated at the origin and are independent of the QCD potential model employed. The formula for positronium annihilation into photons for the $L = 0$ singlet state is

$$\Gamma(^1s_0 \to \gamma\gamma) = \frac{4\alpha^2}{M^2} 4\pi |\Psi_{nl}(0)|^2 \,, \tag{1.2}$$

where M is the resonance mass, and $\Psi_{nl}(0)$ is the non-relativistic radial wave function evaluated at the origin. With the full wave function given by $\Psi_{nlm}(r,\theta,\phi) = R_{nl}(r)Y_{lm}(\theta,\phi)$, $|\Psi_{nl}(0)|^2$ is equivalent to $|R_{nl}(0)|^2/(4\pi)$

The decay rate for $\eta_c \to gg$ can be obtained to leading order in α_s from Equation 1.2 by replacing α by α_s and multiplying by an overall color factor. By comparing the two diagrams in Figure 1.2, the two photon and two gluon rates can be compared to first order. The differences in the matrix elements for the two

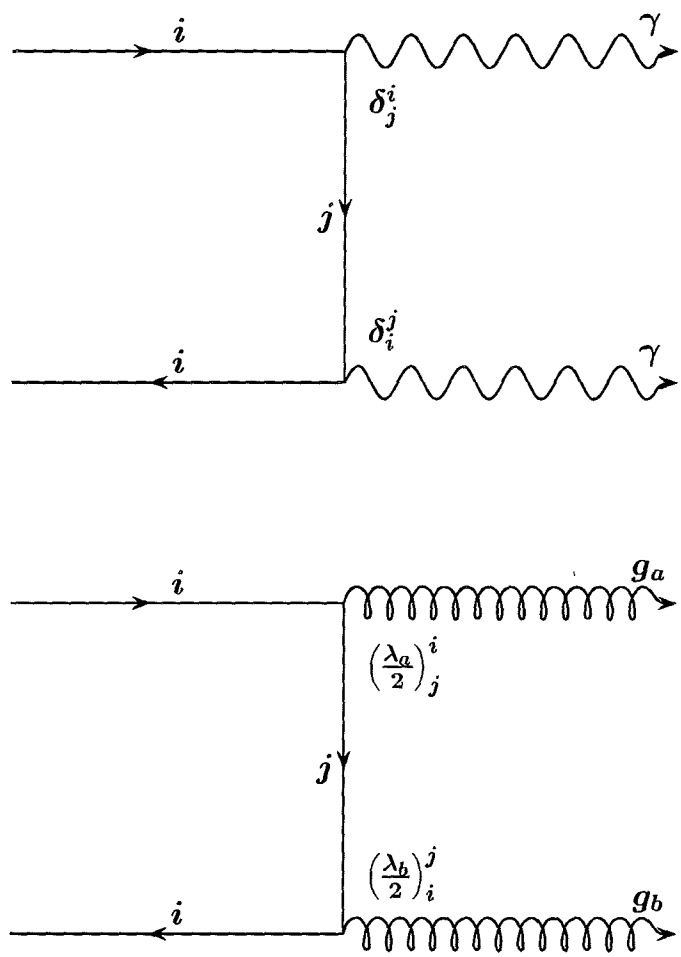

Figure 1.2: Diagrams for $c\bar{c} \to 2\gamma$ or 2 gluons.

diagrams are the coupling strengths and color factors.

$$\begin{aligned}\frac{M(gg)}{M(\gamma\gamma)} &= \frac{\alpha_s}{e_q^2\alpha}\frac{(\lambda_a/2)^i_j(\lambda_b/2)^j_i}{\delta^i_j\delta^j_i} \\ &= \frac{\alpha_s}{e_q^2\alpha}\frac{\frac{1}{2}\delta_{ab}}{3}\end{aligned}$$

Each vertex for the 2γ graph is weighted by the quark charge fraction, e_q, and the electromagnetic coupling, α. The number of colors is 3 ($\delta^i_j\delta^j_i = 3$) and there are eight gluons (a,b = 1,...,8) represented by the Gell-Mann matrices with trace

$$\mathrm{Tr}(\frac{\lambda_a}{2},\frac{\lambda_b}{2}) = \frac{1}{2}\delta_{ab}\,.$$

Since both final states contain 2 identical particles, the ratio of rates is just the square of the ratio of matrix elements,

$$\frac{\Gamma(gg)}{\Gamma(\gamma\gamma)} = \frac{9}{8}\left(\frac{\alpha_s}{\alpha}\right)^2\left(\frac{2/3}{e_q}\right)^4 . \tag{1.3}$$

Since there are only 3 light intermediate fermions, u, d, and s quarks, the rate for $\eta_c \to \gamma\gamma$ to first order in the QCD coupling is

$$\Gamma(\eta_c \to \gamma\gamma) = \frac{12\alpha^2 e_q^4}{M^2}|R(0)|^2\,,$$

where M is the η_c mass in analogy with the $^1S_0$ positronium decay rate. Following the prescription for changing $\Gamma(\eta_c \to \gamma\gamma)$ to $\Gamma(\eta_c \to gg)$ represented by Equation 1.3, $\alpha^2 e_q^4$ is replaced by $\frac{2}{9}\alpha_s^2$ so that the annihilation rate of the η_c into two gluons is

$$\Gamma(\eta_c \to gg) = \frac{8}{3}\frac{\alpha_s^2}{M^2}|R(0)|^2\,.$$

The incorporation of relativistic corrections to the decay rates in a consistent manner poses non-trivial problems associated with gauge invariance and multiple counting with higher-order contributions in the strong coupling. Estimates [19] indicate that relativistic corrections have a small influence on $\eta(^1S_0)$ decays. In

particular, the ratio $\Gamma_{gg}/\Gamma_{\gamma\gamma}$ is free from relativistic corrections up to order $\alpha_s\epsilon/m_c$. Here, ϵ is the binding energy in a non-relativistic Schroedinger model, $M = 2m_c + \epsilon$, where M is the η_c mass.

Next-to-leading order corrections to the photonic annihilation rate are readily obtained from the known electromagnetic corrections to the same process in positronium [20]. The prescription is the replacement $\alpha \to \alpha_s e_q^2$ and an additional factor of 3 to correctly account for the number of light fermions.

$$\Gamma(\eta_c \to \gamma\gamma) = \frac{12\alpha^2 e_q^4}{M^2}|R(0)|^2 \left[1 + \frac{\alpha_s(\mu)}{\pi}\left(\frac{\pi^2}{3} - \frac{20}{3}\right)\right] \tag{1.4}$$

Contributions to next-to-leading order in the hadronic width, Γ_{gg}, are from three-gluon and $q\bar{q}g$ final states. The hadronic width can then be represented by

$$\begin{aligned}\Gamma_{gg} &= \to \Gamma_{gg}^{(0)} + \Gamma_{ggg} + \sum_q \Gamma_{q\bar{q}g} \\ &= \Gamma_{gg}^{(0)}\left[1 + \frac{\alpha_s(\mu)}{\pi}\left(\beta_0 \ln(\frac{\mu}{m_c}) + C[^1S_0]\right)\right] ,\end{aligned} \tag{1.5}$$

where μ is the renormalization scale and the form of $\alpha_s(\mu)$ and β_0 are dependent on the renormalization scheme. The correction, $C[^1S_0]$, is known from the calculation of Barbieri *et al.* [20].

The running strong coupling in Equation 1.5 is evaluated from the two-loop expression, i.e. $\mathcal{O}(\alpha_s^3)$ contributions included, at a scale $\mu = M/2 \approx m_c$. In the modified minimal subtraction scheme, $\overline{MS}$, the corrections for the $\Gamma_{\gamma\gamma}$ and Γ_{gg} widths are $(1 - 3.4\frac{\alpha}{\pi})$ and $(1 + 4.8\frac{\alpha}{\pi})$ respectively [21]. With these corrections and approximating Γ_{gg} by the total width, E760 measures the ratio

$$\frac{\Gamma_{gg}}{\Gamma_{\gamma\gamma}} \approx \frac{2}{9}\left(\frac{\alpha_s}{\alpha}\right)^2 \frac{1}{e_q^4}\frac{(1 + 4.8\frac{\alpha}{\pi})}{(1 - 3.4\frac{\alpha}{\pi})} . \tag{1.6}$$

Both radiative correction factors are large and dependent on the renormalization scheme [21].

Recent developments in effective field theories promise the consistent treatment of relativistic and radiative corrections [22]. Equations 1.4 and 1.5 represent a factorization theorem unproven for higher order calculations. Bodwin *et al.* report a factorization theorem proven in a non-relativistic effective field theory. Others [23] have approached the problem from the perspective of preserving gauge invariance and have produced similar results for $\Gamma_{\gamma\gamma}/\Gamma_{gg}$.

1.4 Exclusive Final States

A significant program in high energy physics has been the study of the electromagnetic structure of the proton. Rosenbluth [24] first described the electromagnetic current structure of the proton in terms of the electric charge, e, and the proton anomalous magnetic moment in units of the Bohr magneton, μ_p,

$$-ie\left[\gamma^\alpha F_1(q^2) + \frac{\mu_p}{2m_p}F_2(q^2)i\sigma^{\alpha\beta}q_\beta\right],$$

where $q^2(<0)$ is the space-like momentum transfer of the electron. $F_1(q^2)$ and $F_2(q^2)$ are the Dirac and Pauli form factors representing the internal structure of the proton, with $F_1(0) = F_2(0) = 1$.

The cross section for the process $ep \to ep$ is then written as

$$\frac{d\sigma}{d\Omega} = \frac{\alpha^2\cos^2(\theta/2)}{4E^2\sin^4(\theta/2)[1+(2e/m_p)\sin^2(\theta/2)]}$$
$$\times\left\{\left[F_1(q^2) - \frac{\mu_p^2}{4m_p^2}q^2F_2^2(q^2)\right] - \frac{q^2}{2m_p^2}[f_1(q^2)+\mu_pF_2(q^2)]^2\tan^2(\theta/2)\right\} .$$

Here $E(>> m_e)$ is the energy of the incident electron and θ the electron scattering angle as measured in the system where the proton is initially at rest. The cross section can be rewritten in terms of the Sachs form factors, G_E and G_M, which are

related to F_1 and F_2 by

$$G_E(q^2) = F_1(q^2) + \frac{q^2}{4m_p^2}\mu_p F_2(q^2) \text{ and } G_M(q^2) = F_1(q^2) + \mu_p F_2(q^2)\,.$$

A large body of data [25] for space-like momentum transfers, $q^2 < 0$, exists for values of $|q^2| \leq 31$ GeV/c^2. Data for time-like momentum transfers [26] from the reaction $p\bar{p} \to e^+e^-$ have been obtained near the threshold for this reaction, $4m_p^2c^4 \leq s \leq 5.6$ GeV^2. Enough integrated luminosity was taken in E760 at $s \approx 9$, 12, and 13 GeV^2 to make total cross section measurements for $p\bar{p} \to e^+e^-$ feasible.

One of the challenges to perturbative QCD (pQCD) is the calculation of nucleon structure. The proton magnetic form factor, G_M, at large momentum transfer has been extensively studied within the framework of the hard-scattering picture (HSP) [27, 28]. The HSP formulation of the proton form factor is expressed as a convolution of a hard-scattering amplitude, T_H, and a proton distribution amplitude, Φ, which represent the valence quark wave functions integrated over quark transverse momenta.

$$G_M(q^2) = \int_0^1 [dx] \int_0^1 [dx'] |f_N(\mu_F)|^2 \Phi^*(x', \mu_F) T_H(x, x', q, \mu) \Phi(x, \mu_F)$$

Here, $[dx] = dx_1 dx_2 dx_3 \delta(1 - \sum x_i)$, x_i being the momentum fractions carried by the valence quarks, and μ is the renormalization scale. The factorization scale, μ_F, defines the interface between soft physics and hard physics. Soft physics is absorbed into the wave function Φ while hard physics is explicitly treated in pQCD. f_N is a dimensional constant that represents the proton wave function evaluated at the origin of the configuration space and has been determined nonperturbatively [29, 30, 31].

While the proton distribution amplitude is known in the limit of large momentum transfers [27], there are several models [29, 30, 31, 32] for Φ at

$q^2 \simeq 1 - 2$ GeV^2/c. However, at the momentum transfers of this experiment, the asymptotic form for $G_M(q^2)$ is assumed to be valid,

$$G_M(q^2) \sim \frac{\alpha_s^2(q^2)}{q^4} \left(\ln \frac{q^2}{\Lambda^2} \right)^{-4/27} \quad . \tag{1.7}$$

The above equation was derived considering space-like momentum transfers.

Similar calculations [33, 34] which include Sudakov suppression factors and proton distribution functions with explicit dependence on the transverse momentum of the valence quarks, have been made for time-like momentum transfers. Point-like color singlets are effectively colorless and will not radiate gluons. The Sudakov corrections account for the physical size of the proton by suppressing contributions to the hard scattering amplitude when the transverse momenta(separations) of the quarks are not large(small) enough to keep exchanged gluons hard. The purpose of these calculations is to extend perturbative QCD predictions for the proton form factor to momentum transfers as low as a few GeV/c.

Bilenky *et al.* [35] have commented that, due to the Phragmén-Lindelöf theorem [36], the proton form factors have the same asymptotic behaviour for space- and time-like momentum transfers. The same asymptotic values for the form factors in the space- and time-like regions up to a correction of order α_s is a particular prediction of pQCD [37]. While the functional form may well be the same, the measurements of G_M for $|q^2| \sim 10$ (GeV/c)^2 in the space- and time-like regions are different by a factor of 3. The current discrepancy between pQCD predictions and the experimental results for the time-like proton form factor is not yet accounted for in a theoretically consistent manner.

Hyer [33] has indicated that the ratio,

$$R_{\gamma\gamma/e^+e^-} \equiv \frac{\sigma(\bar{p}p \to \gamma\gamma)}{\sigma(\bar{p}p \to e^+e^-)} ,$$

is sensitive to the model chosen for the proton distribution amplitude. In addition, the process $\gamma\gamma \to \bar{p}p$, related to $\bar{p}p \to \gamma\gamma$ by detailed balance, has been measured by the CLEO collaboration at $\sqrt{s} \simeq 3.0$ GeV. The $\gamma\gamma$ cross section is subject to sizable backgrounds and onlv $\sim 1/10$ the total integrated luminosity available for experiment E760 was at $\sqrt{s} \sim 2.97$ GeV. For these reasons, only an upper limit is found for the $\gamma\gamma$ total cross section.

Chapter 2

Experimental Apparatus

Experiment E760 was performed at the Fermi National Accelerator Laboratory (FNAL) in Batavia, Illinois. Located in the Antiproton Source, the detector was a non-magnetic spectrometer optimized for the detection of photons and electrons. With a gas jet target, the experiment was able to form each resonance in the charmonium spectrum by tuning the beam energy. With instantaneous luminosities of 10^{-30} $cm^{-2} \cdot s^{-1}$ and a precise beam energy measurement, E760 was a high rate charmonium spectroscopy experiment.

2.1 Fermi National Accelerator Laboratory

The FNAL accelerator complex was built to provide high energy proton beams for colliding and fixed target experimental programs. Figure 2.1 is a schematic of the accelerator beamlines.

Antiprotons are produced by bombarding a target with protons that have been accelerated to 120 GeV in the Main Ring. The source of protons, which is an electrical arc in hydrogen gas, is located in the high-voltage electrode of a Cockcroft-Walton accelerator. The Cockcroft-Walton accelerator produces a 750 KeV beam which is transported to the linear accelerator. The protons are then

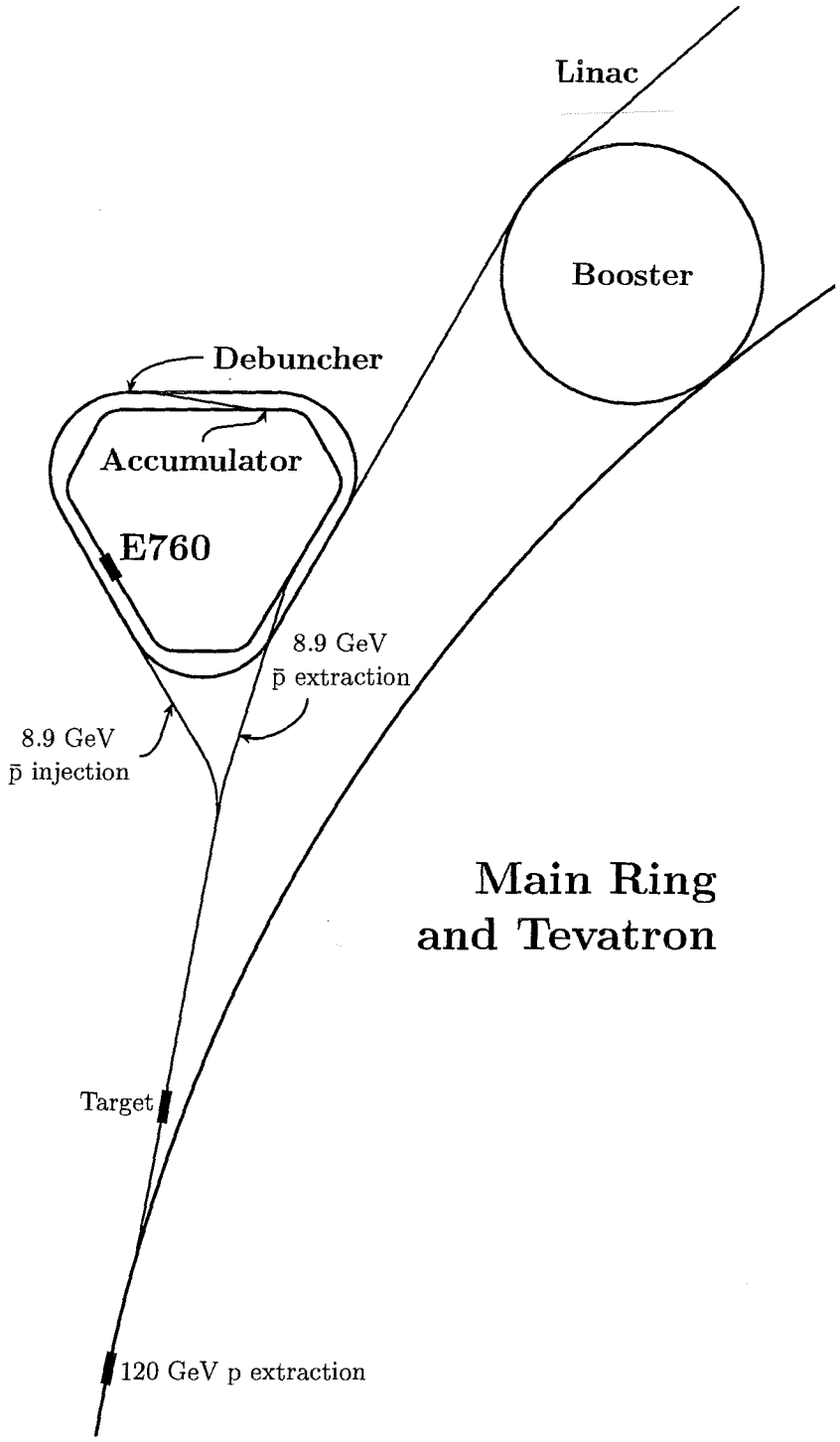

Figure 2.1: Diagram of the Fermilab accelerator complex.

accelerated to 200 MeV and injected into a booster synchrotron which is 150 m in diameter. The protons are accelerated in the booster to 10 GeV and phase matched to the Main Ring RF before being injected. The acceleration of protons to 120 GeV in the Main Ring takes $\approx$ 2 seconds.

2.2 The Antiproton Source

The Antiproton Source [38] consists of a target system, a large aperture ring for RF bunch manipulations, and a storage ring. Once extracted from the Main Ring, the 120 GeV protons are transported to the target assembly. Initial collection of antiprotons is done using a lithium lens. The lens is a lithium cylinder $\approx$ 15 cm long and 2 cm in diameter. A pulsed longitudinal 0.5 MA current produces a radial gradient of 1000 T/m which focuses the negatively charged particles toward a pulsed dipole magnet which selects particles with energy near 8.9 GeV. These particles are transported to the Debuncher for phase space manipulations.

The antiprotons are produced with a large momentum spread. The Debuncher reduces the momentum spread by RF bunch rotation and adiabatic debunching after injection of the antiproton beam. The transverse emittances of the beam are also reduced with stochastic cooling of the betatron amplitudes. These procedures prepare the antiproton beam for injection into the Accumulator, a smaller aperture storage ring.

The Accumulator must accept a pulse of antiprotons from the Debuncher every 2 seconds. Each injected pulse of antiprotons is bunched adiabatically and then decelerated to the edge of the previously injected pulse. The antiprotons are then stochastically cooled to the core orbit or energy. During the 1991 Fermilab fixed target running period, the Accumulator was able to stack a 40 mA beam in

$\approx$ 1 day. The Accumulator is $\approx$ 474 m in length so that 40 mA corresponds to $\approx 4 \times 10^{11}$ antiprotons. Several equipment modifications were needed for the particular use of the Antiproton Source by E760.

To form the charmonium resonances, the Accumulator needed to be operated at several beam momenta, Table 2.1, less than the designed beam momentum of 8.9 GeV/c. An existing serial CAMAC link made software control of the power supplies and RF systems the most inexpensive option. The primary equipment modifications needed were,

- mechanical tuners to the high level RF system,
- programmable frequency synthesizer to the low level RF system,
- and setable delays for the stochastic cooling.

Accumulator Beam Momenta

State	J^{PC}	mass GeV	p_{beam} GeV/c
η_c	0^{-+}	2.981	3.679
J/ψ	1^{--}	3.097	4.066
χ_{c0}	0^{++}	3.415	5.192
χ_{c1}	1^{++}	3.511	5.552
h_c	1^{+-}	3.525	5.605
χ_{c2}	2^{++}	3.556	5.724
η_c'	0^{-+}	3.595*	5.874
ψ'	1^{--}	3.686	6.232

Table 2.1: The Charmonium states and the Accumulator beam momenta. *The η_c' mass has not been confirmed.

Software control of $\approx$ 90 devices was implemented to decelerate the antiproton beam.

2.2.1 Accelerator Physics

The Fermilab Antiproton Accumulator not only provides a source of antiprotons, but also the energy measurement for E760. Several topics from accelerator physics are central to the successful operation of the Antiproton Accumulator for E760. More detailed information can be found in References [39], [40], [41], and [42].

Transverse Motion

Particles in a circular magnetic accelerator are confined to the vicinity of the equilibrium orbit by magnetic focusing. The field gradient index,

$$n \equiv -\frac{r}{B}\frac{\partial B}{\partial r}$$

is a measure of these focusing forces. Large positive values of n indicate strong vertical focusing and radial defocusing. A "strong focusing" accelerator is built by alternating n between large positive and negative values at suitable azimuthal intervals. The FNAL Antiproton Source is a strong focusing accelerator.

In a strong focusing accelerator, the ideal particle follows a path called the equilibrium or closed orbit. The coordinates and momenta of actual particles in a beam are usually expressed relative to the equilibrium orbit. The equations of motion are the Lorentz force equation

$$\frac{d\vec{P}}{dt} = e\left(\vec{E} + \frac{\vec{v}}{c} \times \vec{B}\right) \quad ,$$

which, in this form, has time as the independent variable. The motion of the ideal particle with momentum p_0 in an accelerator is periodic. A particle with momentum p_0 which is started with a small initial displacement and angle from the equilibrium

orbit will remain near the equilibrium orbit so that a more convenient independent parameter is the arc length s along the reference trajectory. The position of a particle near the equilibrium orbit is characterized by

s the arc length along the equilibrium orbit as measured from a fixed reference to the point of closest approach

x the horizontal displacement in the plane of the equilibrium orbit with the positive direction outward

y the vertical displacement from the equilibrium orbit.

The characteristics of the transverse motion of the beam particles are well described by the Lorentz force equation linearized in the coordinates x and y and their derivatives. Equivalently, the displacements x and y are taken to be small with respect to the radius of curvature, $\rho(s) = p_0 c/eB_z(s,0,0)$, and the momenta, p_x and p_y, are small with respect to p_0. The additional assumptions of no electric fields, only external magnetic fields transverse to the equilibrium orbit, and negligible particle interactions leads to a description of the transverse motion by Hill's equation

$$\frac{d^2x}{ds^2} + k(s)x = 0\,, \tag{2.1}$$

where $k(s + C_0) = k(s)$, where C_0 is the total path length of the equilibrium orbit. With these simplifying assumptions, the equation for x is adequate for the treatment of the betatron oscillations. The function k is dependent on the strength and position of the quadrupole magnets.

The general solution to Hill's equation is

$$x = \sqrt{\epsilon\beta(s)}\cos[\psi(s) + \delta]$$

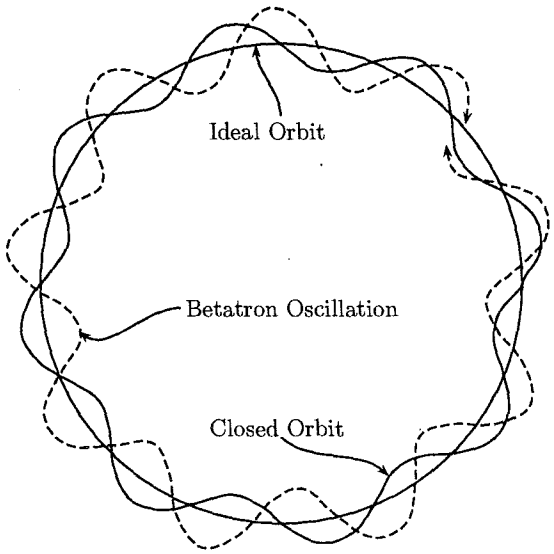

Figure 2.2: The figure indicates the ideal circular path, closed equilibrium orbit, and betatron oscillation with non-integral tune for a strong focusing accelerator.

$$\psi(s) = \int_{s_0}^{s} \frac{ds'}{\beta(s')} \quad .$$

The function, $\beta(s)$, is dependent on the accelerator lattice (where magnets are placed in the beam line) and satisfies the equation

$$2\beta\frac{d^2\beta}{ds^2} - \left(\frac{d\beta}{ds}\right)^2 + 4k\beta^2 = 4 \quad .$$

The function $\psi(s)$ is the phase advance from a fixed reference point on the equilibrium orbit, s_0. The value of ϵ is independent of s and is the 2-dimensional phase-space area occupied by the trajectory of the particle.

Under the Courant-Snyder transformation,

$$\zeta = \frac{x}{\sqrt{\beta}}, \quad \phi = \int \frac{ds}{\nu\beta},$$

Equation 2.1 becomes

$$\frac{d^2\zeta}{d\phi^2} + \nu^2\zeta = 0,$$

where $\nu = (2\pi)^{-1} \oint ds/\beta$ is the tune of the machine and is the number of betatron oscillations in one turn around the machine lattice. Because of the natural periodicity of a synchrotron, a non-integral tune is necessary to keep the betatron amplitude from growing resonantly due to perturbations from magnet imperfections. Simply stated, the particle trajectory can not be a closed path and still remain in the physical confines of the vacuum chamber.

Momentum Compaction

A particle with $\delta p = p - p_0 \neq 0$ will satisfy the inhomogeneous equation,

$$\frac{d^2x}{ds^2} + k(s)x = \frac{1}{\rho(s)}\frac{\delta p}{p_0},$$

where the momentum dependence is suppressed as in Equation 2.1 due to the smallness of p_x with respect to p_0. The particular solution is written as

$$x_D(s) = D(s)\frac{\delta p}{p_0}$$

where the dispersion function, D, is periodic, $D(s + C) = D(s)$, and satisfies the equation

$$\frac{d^2D(s)}{ds^2} + k(s)D(s) = \frac{1}{\rho(s)}.$$

The path length for a particle on the dispersion trajectory, $x_D(s)$, is

$$C = \oint ds \left(1 + \frac{x_D(s)}{\rho(s)}\right) = C_0 + \delta C$$

where the differential is shown in Figure 2.3. The above equation indicates that momentum differences will cause the total path length to change which introduces the momentum compaction factor,

$$\alpha = \frac{\delta C/C_0}{\delta p/p_0} = \frac{1}{C_0}\oint ds \frac{D(s)}{\rho(s)}.$$

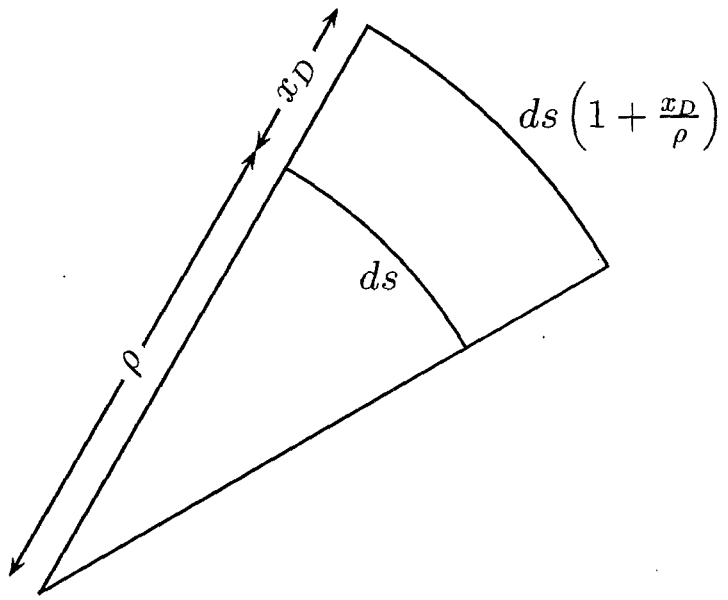

Figure 2.3: Orbit Differential

The frequency of particle rotation around the accelerator may be related to the momentum using the momentum compaction factor, α. A particle travels around the accelerator lattice with a frequency $f = v/C$ where v is the velocity and C the total path length. The fractional variation in the frequency is

$$\frac{\delta f}{f_0} = \frac{\delta v}{v_0} - \frac{\delta C}{C_0}$$

or in terms of the momentum fraction and the relativistic γ for the beam,

$$\frac{\delta f}{f_0} = \left(\frac{1}{\gamma^2} - \alpha\right)\frac{\delta p}{p_0}.$$

The "frequency slip" factor is defined as

$$\eta \equiv -\frac{\delta f/f_0}{\delta p/p_0} = \left(\frac{1}{\gamma_{\rm tr}^2} - \frac{1}{\gamma^2}\right)$$

with $1/\gamma_{\rm tr}^2 = \alpha$ and $\gamma_{\rm tr}$ is the relativistic gamma for the "transition" beam energy. Below the transition energy, velocity changes dominate and therefore particles with

momentum larger than p_0 circulate with higher frequency while above the transition energy the particles would circulate with lower frequency. The transition energy for the FNAL Accumulator is ≈ 4.7 GeV ($\gamma_{\rm tr} \approx 5$) and must be crossed for beam energies corresponding to the J/ψ and η_c resonances.

Stochastic Cooling

The beam current in a circular particle accelerator exhibits a random component called Schottky noise which results from the individual particles in the beam. At a particular location in the accelerator, the beam current from a single particle is a train of delta pulses separated in time by $1/f_i$, $f_i \equiv$ the frequency of rotation for the $i^{\rm th}$ particle. Considering only the positive frequencies, $\omega_i = 2\pi f_i$, the current pulse train can be expanded in a Fourier series as,

$$\iota_i(t) = ef_i + 2ef_i \sum_{n=1}^{\infty} \cos(n\omega_i t)\,.$$

The average, $< \iota^2 >$, does not vanish because of $\cos^2(n\omega_i t)$ terms and $\iota_{\rm rms} = 2ef_0\sqrt{N/2}$. Here, N is the number of particles and f_0 is the circulation frequency of a particle on the equilibrium orbit. Since the spectral power density, $P(f)$, is proportional to $< \iota^2 >$, measurement of the Schottky spectrum measures particle densities.

The transverse motions of the beam particles also have a Schottky component. Replacing the beam current by the dipole moment, $d_i(t) = a_i(t) \cdot \iota_i(t)$, where $a_i(t)$ is the transverse displacement , or betatron motion, gives $d_{\rm rms} = ef_0 a_{\rm rms}\sqrt{N/2}$. Again, the spectral power density is proportional to the number of particles. Particle densities may be measured for both the longitudinal and transverse directions.

The simple case of a single particle and a "pickup" which consists of a plate on either side of the beam provides a conceptual understanding of stochastic cooling. As the particle passes through the pickup, a current is induced on each plate. The difference between the two signals is a measure of the "position error" of the particle or the displacement from the center of the pickup. A "kicker" is a similar arrangement of plates on which an electromagnetic field is created that deflects the particle by an angle proportional to the position error.

Signals from the pick-up will need to travel along a shorter path than the particle trajectory since the particles have velocities near the speed of light. Ideally, the distance between the pickup and kicker is $(2k+1)\lambda_\beta/4$ where λ_β is the wavelength of the betatron oscillations. At a quarter wavelength separation, a particle that passes through the pickup at a maximum of the betatron oscillation will cross the kicker with no position error and be deflected onto the correct orbit.

Momentum cooling at the FNAL Accumulator is done using a notch filter. The simplest case of a notch filter is a low loss transmission line that has a length such that a pulse from a particle with the nominal frequency will be cancelled by the reflected pulse from the previous revolution. The signals from particles which are too fast or slow will be imperfectly cancelled and the particles are accelerated accordingly.

2.2.2 Deceleration of Antiprotons

The deceleration of antiprotons [43] at a rate of $\sim$ 20 MeV/s is managed by a dedicated computer running a program that sequentially changes the settings of the ramped devices according to interpolation of an input file or "ramp table." The ramp tables were constructed empirically. A first guess was made by taking the 8.9

GeV/c starting beam momentum and extrapolating to 0 GeV/c. Since there is a transition energy where the RF accelerating frequency must undergo a phase change, at least 3 ramp tables are needed. A ramp table for above transition, the actual transition crossing, and below transition.

At each "ramp point", several accelerator parameters were measured and corrected until they agreed with their target values. The parameters were the closed orbit, the horizontal and vertical tunes including their coupling, the horizontal and vertical chromaticity, and the dispersion of the beam. The revolution frequency after these adjustments was measured for the RF frequency ramp. This procedure required a large number of iterations until a working ramp table was completed.

Each of the ramped devices has a particular update frequency of which several are shown in Table 2.2. The natural time constants of the power supplies are

Device Type	Quantity	Update Frequency (Hz)
Dipole Bus	1	60
Quadrupole Bus	1	60
Sextupole	5	7.5
Skew Quads	2	7.5
Octupoles	2	7.5
Horiz. trims	8	0.5
Vert. trims	24	0.5
Dipole shunts	30	0.5
Damper timing	4	0.5

Table 2.2: For the different types of magnets, "Quantity" refers to the number of power supplies.

relied upon to filter the steps generated by the digital ramp table. Due to the 60 Hz update frequency, the power supply ramps are digitally filtered to smaller step sizes. This is accomplished by a dedicated microcomputer which is programed with a filter time constant approximately equal to the natural step response time constant of the dipole bus.

Actual deceleration of the antiprotons begins after an appropriate amount have been accumulated or "stacked." The phase space of the antiproton beam is first reduced with the stochastic cooling. The transverse dimensions of the beam prepared for deceleration are 1 - 2 π mm-mrad while the beam momentum spread, $\delta p/p$, is $\approx 10^{-4}$. The beam is then decelerated to just above the transition energy. To decelerate below transition, the RF is first turned off and the focusing characteristics of the quadrupole magnets are changed in order to raise the transition energy to a value greater than the beam energy. The beam is recaptured with the RF and decelerated with the focusing characteristics being gradually changed back to their nominal values.

2.2.3 Beam Energy Measurement

Precision measurement [44] of charmonium masses is dependent on the beam energy measurement. The energy is measured by calculating the mean particle velocity, $\beta = fC/c$, where f is the mean revolution frequency and C is the orbit length at the mean frequency. The Schottky beam power spectrum is detected by a coaxial 1/4 wavelength resonant pickup. The spectrum is analyzed by a Hewlett-Packard 8568B Spectrum Analyzer which determines the average frequency to 1 part in 10^7.

Orbit Length

Any orbit length, C, is given by the equation

$$C = C_{\text{ref}} + \Delta C$$

where C_{ref} is the orbit length for a known energy and ΔC is the deviation from the reference orbit length. From special relativity,

$$\gamma = \frac{E}{m}$$

where E is the beam energy, γ the Lorentz factor, and m the mass of the proton. Since $\gamma = 1/\sqrt{1-\beta^2}$,

$$\delta\gamma = \gamma^3\beta^2\frac{\delta C_{\text{ref}}}{C_{\text{ref}}} = \frac{\delta E}{m}$$

The beam energy may also be written in terms of E_{cm}, the total energy in the center of momentum frame.

$$E = \frac{{E_{\text{cm}}}^2}{2m} - m$$

This formula implies that $\delta E = E_{\text{cm}}\delta E_{\text{cm}}/m$. The variation of the orbit length may now be related to the variation in the center of momentum energy by,

$$\delta C_{\text{ref}} = \frac{C_{\text{ref}}E_{\text{cm}}\delta E_{\text{cm}}}{\gamma p^2}$$

where the relativistic expression for the magnitude of the beam momentum, $p = \gamma\beta m$, has been used to simplify the equation.

For E760, the reference orbit is taken at the ψ' resonance. The systematic uncertainty in the reference orbit length due to uncertainty in the resonance mass is

$$\delta C_{\text{ref}} = \frac{C_{\text{ref}}M_{\psi'}}{\gamma p^2}\delta M_{\psi'}$$

where γ and p^2 are the relativistic factor and momentum of the beam. For the case of the ψ', $\delta M_{\psi'} \approx 100$ KeV which gives $\delta C_{\text{ref}} = 0.7$ mm.

Using the differential shown in Figure 2.3 to estimate the orbit path length and taking into account the 30 main dipoles in the Accumulator [45], the path length can be well approximated by

$$C = C_{\text{ref}} + \sum_{i=1}^{30} \frac{x_i}{r} l_{\text{dipole}} \,.$$

The displacement at the ith dipole from the reference orbit is x_i with r the local radius of curvature and l_{dipole} the dipole length. Beam Position Monitors (BPMs) measure the displacement from the reference orbit at ~ 49 positions around the orbit. The displacement at each BPM is treated as a superposition of dipole kicks from all the horizontal bending dipole magnets written as

$$x_j(\vec{\theta}) = \frac{\sqrt{\beta_j}}{2 \sin \pi\nu_x} \sum_{i=1}^{N_d} \sqrt{\beta_i}\theta_i \cos(\pi\nu_x - \Delta\phi_{ij})$$

where,

N_d is the number of horizontal dipole elements,

ν_x the horizontal tune,

β_j the horizontal beta function at the jth BPM,

β_i the horizontal beta function at the ith dipole element,

$\Delta\phi_{ij}$ the absolute value of the phase advance from the ith dipole to the jth BPM,

θ_i the angular kick due to the ith dipole.

The vector $\vec{\theta} = (\theta_1, \ldots, \theta_{N_d})$ is determined by a least squares fit to the BPM measurements. Deviations at the center of the dipoles, x_i, are then calculated using the best fit results.

Beam Width

The beam width is important for the measurement of the resonance widths. Scans of the charmonium resonances are performed by stepping the beam in energy

and counting the number of events to determine the effective cross sections at each energy. The effective cross section is a convolution of the beam energy spectrum and a Breit-Wigner resonance.

The beam momentum spectrum is obtained from the beam revolution spectrum measurement by equation

$$\Delta p/p = \frac{1}{\eta} \cdot \Delta f/f \, .$$

Uncertainty in the frequency slip factor is the primary contribution to the uncertainty in the determination of the beam momentum spectrum. For a stationary beam with an RF modulation, η is related to the synchrotron oscillation frequency, Ω_s, by,

$$\eta = \frac{2\pi H \Omega_s^2 \beta^2 E_{\text{beam}}}{f_{\text{RF}}^2 (eV_{\text{RF}})}$$

where, for the Accumulator, the RF frequency is set at the second harmonic, $H = 2$, of the average rotation frequency and is well known. The beam energy, E_{beam}, is also well known compared to the measurement of the RF voltage. The synchrotron frequency is measured as a function of the RF voltage, V_{RF}. High voltage probes measure the RF gap voltage directly to reduce this primary source of error in the measurement. This measurement is assigned a 10% uncertainty.

2.3 E760 Detector

The E760 detector is designed primarily for the detection of two and three body electromagnetic final states of charmonium resonances formed in antiproton proton annihilations. Two electrons from J/ψ decay is the principal signal for radiative transitions. Two and three final state photons will also occur from resonant decays and radiative transitions. These electromagnetic final states are

present in a large hadronic background which produces both charged and neutral particles. Because the target is located in a storage ring, events are produced continuously. These considerations require that the detector be designed with the following abilities.

- fast trigger formation
- electron - pion separation
- differentiation of single photons and the symmetric decays of π^0s
- good energy resolution for electrons and photons
- low energy response (20 - 50 MeV) for photons
- both charged and neutral tracking

The detector, Figure 2.4, is a cylindrically symmetric non-magnetic spectrometer. The size of the detector hall prohibited the use of a magnet. Presentation of the different detector subsystems will begin with the target and proceed radially outward.

2.3.1 Gas Jet Target

The target for E760 is a hydrogen gas target inside the Accumulator vacuum chamber. The beam storage lifetime, size and momentum characteristics of the beam are affected adversely by the introduction of gas into the vacuum chamber. These adverse effects are largely countered by the stochastic cooling systems leaving the advantages of high luminosity, continuous operation, and small target area.

A molecular beam target assembly [11] provides a flow of supersonic gas. The 'jet' is made by the expansion of gas from a vessel at high pressure (10 - 15 bar) and low temperature (77° K) into the vacuum through an injector. The injector, which

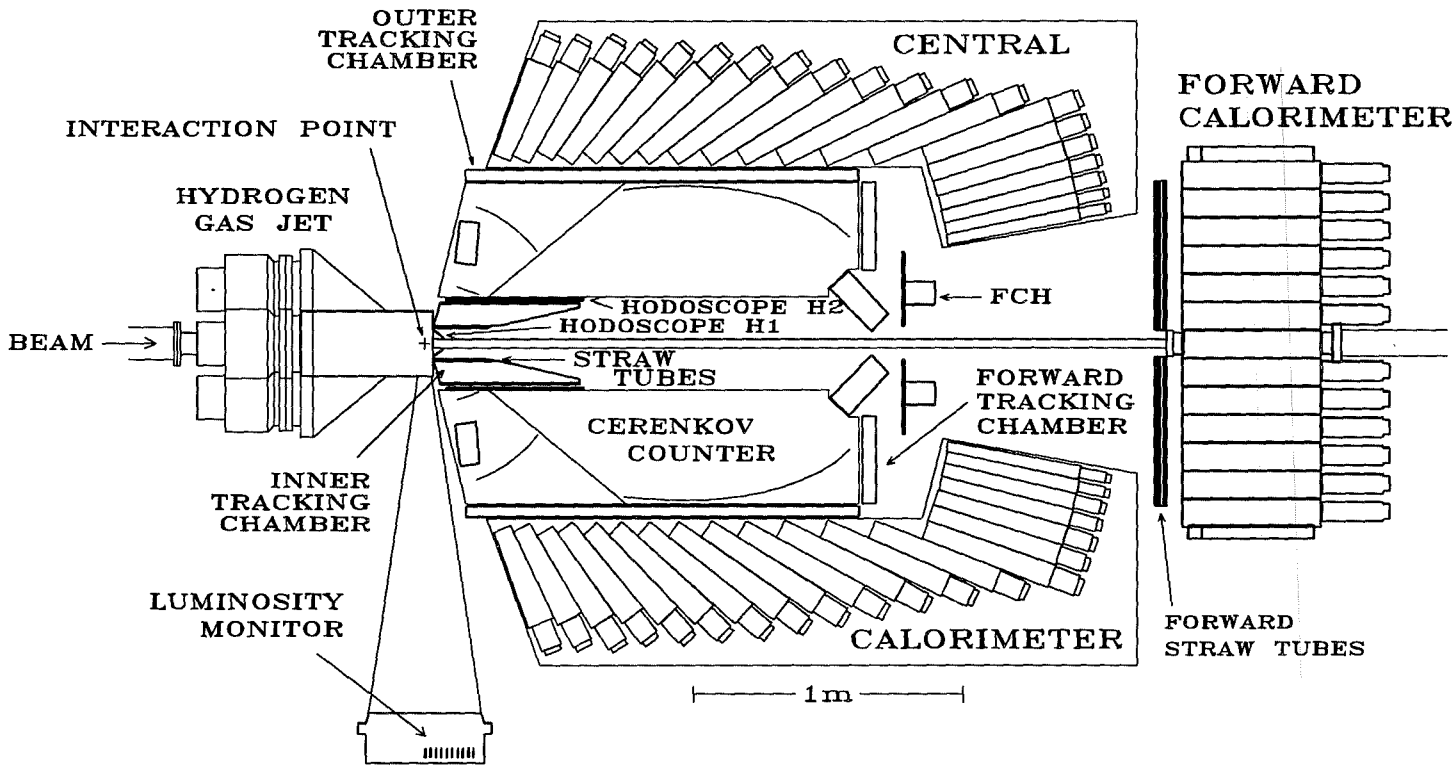

Figure 2.4: A side view of the spectrometer for experiment E760.

provides the highest intensity, has a trumpet shaped geometry. Such a geometry slows the rate of expansion allowing for a supersaturation condition to be present in the jet within the throat diameter of the nozzle. With appropriate densities and pressures, clusters of $\approx 10^6$ hydrogen molecules will form. These clusters form the target material. Collimators ensure that only the molecular clusters enter the vacuum chamber. The unused gas is absorbed after traversal of the vacuum chamber by another pumping system. The interaction region for E760 had a volume ≈ 1 cm^3 and a target density of $\approx 10^{14}$ atoms/cm^3. With such a target, instantaneous luminosities of $\sim 10^{31}$ cm$^{-2}\cdot$s^{-1} are obtained.

2.3.2 Luminosity Monitor

The luminosity measurement [46] for E760 is based on forward elastic scattering of antiprotons. The cross section is measured by counting the recoiling protons at nearly 90°. The recoil counts S are related to the integrated luminosity L by

$$S = L \int \frac{d\sigma}{d\Omega}\, d\Omega\,,$$

where the integral extends over the active area of the detector.

The detector is an ion-implanted solid state detector with a depletion depth of 500 μm which will stop protons with kinetic energy ≤ 8.1 MeV. The manufacturer specified active area is 12 mm $\times$ 48 mm. Placed at 86.5^o with respect to the antiproton beam, the detector stops the recoil proton for any available antiproton energy, see Figures 2.5, 2.6.

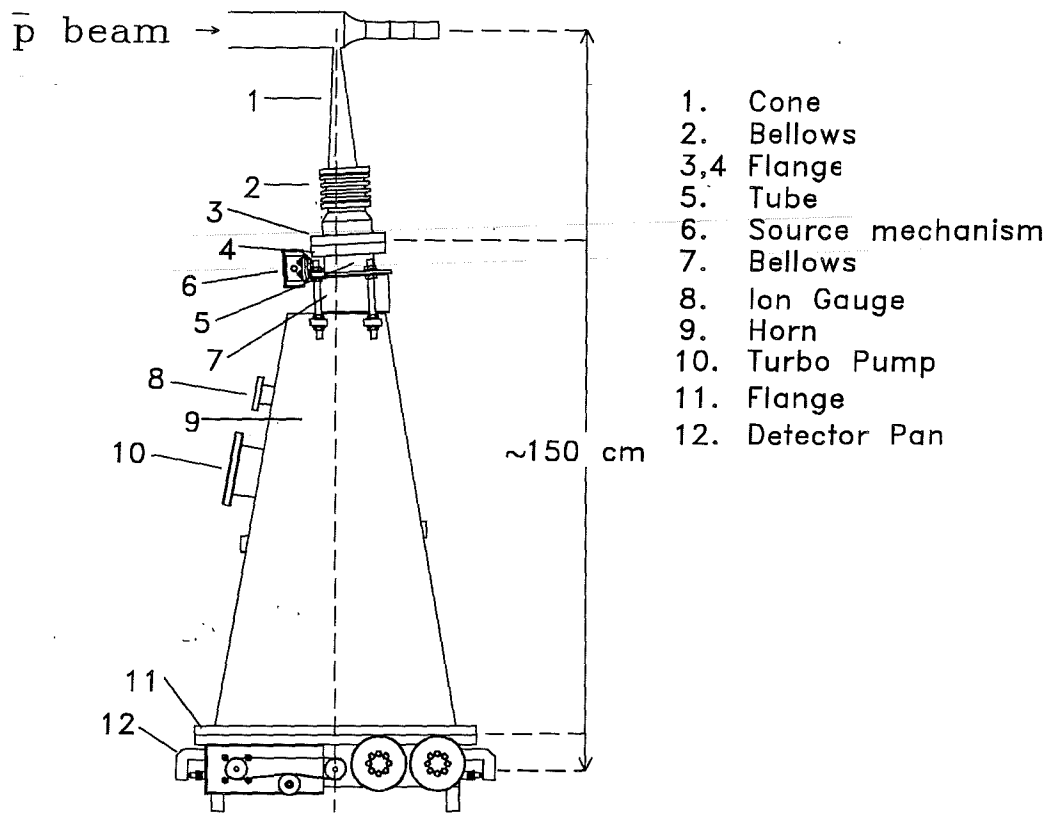

Figure 2.5: Schematic view of the luminosity monitor.

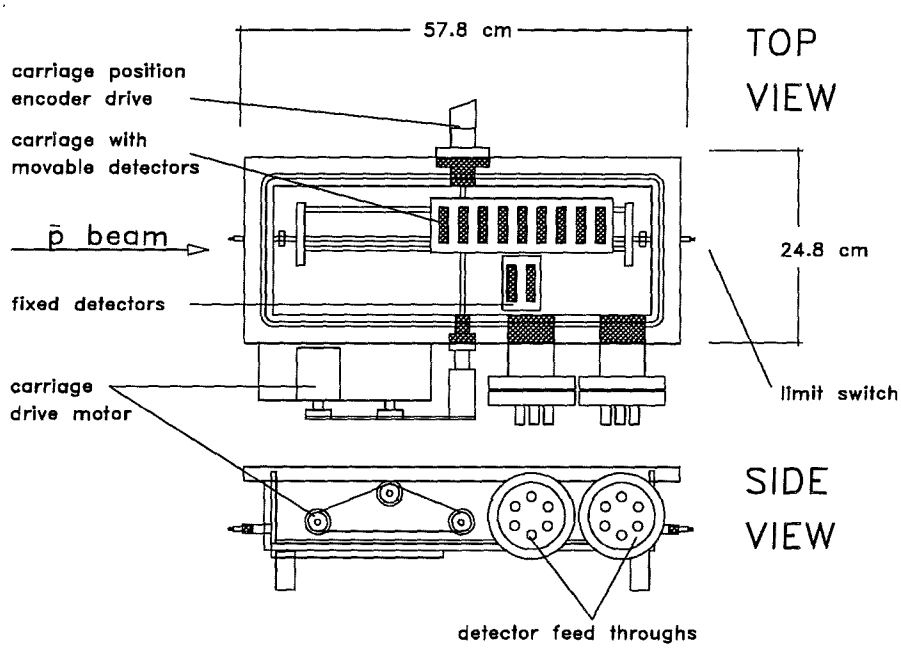

Figure 2.6: Schematic view of the moveable base for the luminosity monitor.

At a recoil angle of 3.5^o, the differential cross section for forward elastic scattering is approximately linear in momentum transfer t,

$$\frac{d\sigma}{dt} \approx \frac{\sigma_{\mathrm{T}}^2(1+\rho^2)}{16\pi(\hbar c)^2}(1-bt)\,,$$

where ρ and b are empirically determined parameters and σ_{T} is the total $\bar{p}p$ cross section. The Coulomb scattering and interference terms are negligible. The integral, S, may be approximated to an accuracy of 0.1% as

$$S \approx L\langle\frac{d\sigma}{dt}\frac{dt}{d\Omega}\rangle \int d\Omega\,,$$

or,

$$L = S/\left(\Omega\langle\frac{d\sigma}{dt}\frac{dt}{d\Omega}\rangle\right)$$

where $\langle(d\sigma/dt)(dt/d\Omega)\rangle$ represents the quantity evaluated at the center of the detector. The two sources of systematic errors are the solid angle Ω and the differential cross section $d\sigma/dt$. The systematic errors in the final luminosities are estimated to be $\pm 2\%$ due to σ_{T} and $< \pm 2\%$ due to the solid angle calibration.

2.3.3 Charged Tracking

The charged tracking subsystems consists of two hodoscopes, an atmospheric pressure threshold Čerenkov detector, and several wire chambers. These subsystems provided charged particle tracking, fast triggering capabilities, electron/pion separation and dE/dx information for the experiment.

Hodoscopes

The hodoscopes are made of scintillating plastic (NE102) counters. H1 is the nearest to the interaction region and is azimuthally segmented into 8 counters. The

counters are 2 mm thick and shaped so that charged particles pass through the same amount of material, 0.005 L/X_0 in units of radiation length, regardless of polar angle. The H1 hodoscope covers the polar angle region 9° to 70°.

The H2 hodoscope is azimuthally segmented into 32 counters with the seams between elements aligned with those in the H1 hodoscope. H2 is 4 mm thick and is located at a radial distance of $\sim$ 16.5 cm which corresponds to a radiation length of $(0.012/\sin\theta)(L/X_0)$. The H2 hodoscope covers the polar angle region 12° to 70°.

Čerenkov Detector

A threshold Čerenkov light detector [47] is used for electron detection and electron/pion separation. The detector is cylindrically symmetric and has an active region covering the polar angles 15° to 70°. There are 8 azimuthal regions, each divided into 2 polar regions by a septum placed at $\vartheta = 38°$ in the lab system. Two types of gases, CO_2 downstream ($15° \leq \vartheta \leq 38°$) and Freon 13 upstream ($38° \leq \vartheta \leq 70°$), are used to optimize both electron detection and electron/pion separation. The CO_2(Freon 13) has a pion momentum threshold for Čerenkov light of 4.9(3.7) GeV/c. The Čerenkov light is reflected to a phototube using an ellipsoidal mirror in the downstream cells and a spherical mirror in the upstream cells, Figure 2.7.

Wire Chambers

Between the hodoscopes, H1 and H2, are the inner charged tracking chambers consisting of straw tubes, a radial projection chamber (RPC), and a cylindrical multiwire proportional chamber (MWPC) [48]. The straw tubes consist of two layers of 22 cm long mylar tubes with centers located at radial distances of

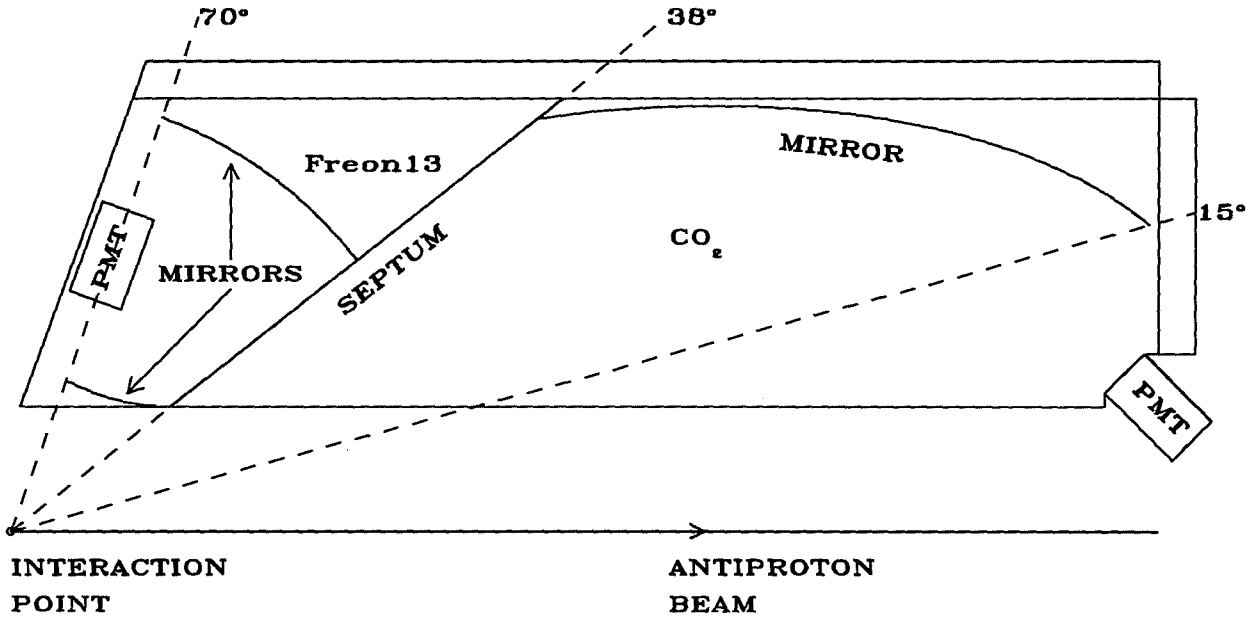

Figure 2.7: A theta view of the atmospheric Čerenkov detector for experiment E760.

5.52 cm and 6.35 cm. The gas is a Ar-$C0_2$-CH_4 mixture and the wires are 25 μm in diameter with a resistance of 850 Ω. The drift time measurement gives a spatial resolution of $\sim$ 200 μm and the charged division measurement a resolution in the z coordinate of $\sim$ 3 mm.

The RPC and MWPC are in a cylindrical volume 542 mm long and 314 mm in diameter, 25 mm downstream of the interaction region. The detectors are coaxial with the cylindrical coordinates (ρ, z, ϕ) and dE/dx measurement for 16 samples on each track recorded. The azimuthal coordinate is given by the RPC wire number and drift time of the first sample with the outer MWPC used to remove the left right ambiguity. The radial component and the longitudinal component for each of the 16 samples are measured using the drift time and charge division on the RPC wires respectively.

The RPC is equipped with 80 sense wires 20 μm in diameter separated by 80 field wires 100 μm in diameter. The sense wires are made of a Fe-Ni-Cr compound with a 3300 Ω/m linear resistance. The multiplication region is separated from the drift volume by a cylindrical grid of 240 wires 100 μm in diameter which is kept at a lower voltage than the field wires.

The MWPC consists of 320 sense wires, 20 μm diameter gold-plated tungsten, and 300 pads etched on the external cathode which provide a measurement of the longitudinal coordinate. The wire pitch is such that four MWPC wires cover each 3 wire drift cell of the RPC.

2.3.4 Calorimetry

There are two calorimeters in the E760 detector, Fig. 2.4. The forward calorimeter (FCAL) [49] is a sampling electromagnetic calorimeter used primarily

for the rejection of forward going background photons. The central calorimeter (CCAL) [50] is the primary detector for electrons and photons. A clustering algorithm for the CCAL and the resulting energy and position resolutions are also discussed.

FCAL

The FCAL is located 340 cm downstream from the interaction region covering the polar angle from 2° to 12°. There are 144 square modules arranged in a 13×13 array with 6 modules on each corner and 1 module for the beampipe removed. Each 10 cm × 10 cm module is 50 cm in length and consists of 148 layers alternating between lead and scintillating plastic. The lead plates are 1 mm thick with the first 32 scintillating plates 0.64 cm thick and the remaining 42 plates alternating between 0.64 cm and 0.32 cm thickness. The active length of each module is 48.4 cm which corresponds to 14.7 radiation lengths.

The higher sampling ratio at the front gives a better low energy response while the lower sampling ratio at the back of the module gives better energy resolution for higher energy photons. The calibration of the FCAL was obtained by minimizing the π^0 width observed at a beam momentum of 8.9 GeV/c. The energy resolution was found to be

$$\frac{\sigma}{E} = \left(\frac{0.19}{\sqrt{E\,(\mathrm{GeV})}}\right)$$

and a transverse position resolution of 3 cm for photons with energy greater than 1 GeV.

CCAL Mechanical Properties

The CCAL was designed to detect electrons and photons as well as distinguish them from π^0s. The symmetric decay of a π^0 into two photons and the loss of the low energy photon in an asymmetric π^0 decay were the two backgrounds taken into primary consideration in the design of the CCAL. Adequate granularity and low energy response provided the capability to distinguish these backgrounds.

The CCAL covers the polar angle region from 10° to 70° and consists of 1280 lead glass blocks situated with a geometry pointing to the interaction region. Two "wedges" are shown in Figure 2.4. There are 64 identical azimuthal wedges which are segmented into 20 elements, each a different size glass block, in the polar angle. Each set of 64 identical blocks sharing the same polar angle constitutes a "ring". The glass blocks are 30 cm to 50 cm long which is 12 to 16 radiation lengths for F2 type lead glass. The sizes are chosen to contain $\sim$ 95% of the electromagnetic shower in each block. Properties of F2 type lead glass and the dimensions for each block are in Tables 2.3 and 2.4.

Each CCAL wedge is a single mechanical and electrical unit which is a light tight container. The wedges are made of 0.735 mm thick stainless steel sides with 19, 0.245 mm thick, stainless steel partitions. Once the steel pieces are spot welded together, 20 lead glass/photomultiplier modules are placed into the slots. The photomultiplier tubes are glued to the end face of each block and wrapped in μmetal. The glue has the same index of refraction as the F2 lead glass. Table 2.5 summarizes the characteristics of the 4 different size Hamamatsu photomultiplier tubes used.

F2 Type Lead Glass

Composition by Weight		Transparency (10 cm)	
		Wavelength (nm)	Transmittance
Lead	42.2%	335-344	56.9%
Oxygen	29.5%	385-394	95.5%
Silicon	21.4%	435-444	97.9%
Potassium	4.2%	485-494	98.4%
Sodium	2.3%	535-544	98.9%
Arsenic	0.15%	585-594	99.4%

Bulk Properties:

Radiation Length	3.141 cm
Density	3.61 g/cm^3
Refractive Index at 404.7 nm	1.651

Table 2.3:

CCAL Triggering

The all-neutral cross section [51] at $E_{\rm cm} = 3.550$ GeV is expected to be 1-2% of the total annihilation cross section of 22 mb [52]. This will result in a $\sim$ 4.4 kHz neutral trigger rate for expected luminosities of 10^{31} cm$^{-2}\cdot$s^{-1}. While the errors on these numbers may be quite large, Monte Carlo studies [53] indicated that requiring two energy deposits or clusters with large transverse momentum should reduce the neutral trigger rate to $\sim$ 400 Hz.

The CCAL trigger groups the 1280 modules into 40 "super-clusters." Table 2.6 lists the wedges and rings in each super-cluster. 5% of each of the 1280 signals are first summed into 8 overlapping super-wedges and then amplified by a factor of 10. For each of the 8 super-wedges, there are 20 summed signals, one for each block shape. 2.5% of each of the 20 signals is given a weight relative to four other summed signals which are again summed to make a "super-ring" signal which is amplified by a factor of 20. The weighting factors are also found in Table 2.6.

Block Dimensions and Positions

Block #	Length (L/X_0)	$(\lvert\Delta\vartheta\rvert)^\circ$	$(\lvert\Delta\phi\rvert)^\circ$	Distance from target (cm)	Fractional PMT coverage
1	12.03	5.226	5.625	72.44	0.473
2	12.30	5.031	5.625	75.87	0.475
3	12.70	4.803	5.625	80.07	0.476
4	13.21	4.552	5.625	85.08	0.478
5	13.86	4.284	5.625	90.96	0.479
6	14.65	4.007	5.625	97.79	0.481
7	15.59	3.728	5.625	105.62	0.482
8	15.92	3.451	5.625	114.54	0.497
9	15.92	3.183	5.625	124.66	0.520
10	15.92	2.925	5.625	136.07	0.544
11	15.92	2.679	5.625	148.89	0.568
12	15.92	2.449	5.625	163.26	0.593
13	15.92	2.233	5.625	179.34	0.617
14	15.92	2.033	5.625	197.28	0.641
15	15.92	1.848	5.625	197.29	0.546
16	15.92	1.678	5.625	197.30	0.664
17	15.92	1.522	5.625	197.30	0.527
18	15.92	1.380	5.625	197.30	0.644
19	15.92	1.250	5.625	197.30	0.543
20	15.92	1.131	5.625	197.30	0.543

Table 2.4:

Photomultiplier Characteristics

Photocathode Material	Bialkali
Window Material	Borosilicate Glass
Dynode Structure	Linear Focused
Sensitivity Range	300 - 650 nm
Peak Sensitivity	420 nm
Quantum Efficiency (450 nm)	0.15

Model(Wedges)	# Dynodes	Diameter (in)	Length (in)
R3036-02(1-14)	12	3.0	5.0
R3345-02(15,16)	12	2.5	5.0
R2154-04(17,18)	10	2.0	6.0
R580-13(19,20)	10	1.5	6.0

Table 2.5:

Another 2.5% of the 20 signals is again summed and amplified by a factor of 20. These 8 signals are again summed to represent the total energy in the CCAL. This total energy signal is then discriminated to form the ETOT trigger logic.

Super-Wedge Sums

Super-Wedge	Wedge #s
1	1-9
2	9-17
3	17-25
4	25-33
5	33-41
6	41-49
7	49-57
8	57-1

Super-Ring Sums

Super-Ring	Ring #s (Weights)
1	1-4 (1.1:1:.91:.81)
2	4-8 (1.21:1.1:1:.91:.83)
3	8-12 (1.19:1.07:1:.95:.91)
4	12-16 (1.1:1.05:1:.95:.93)
5	16-20 (1.05:1.02:1:.98:.95)

Table 2.6: The summing pattern for the CCAL trigger.

The five super-ring by eight super-wedge array results in 40 super-clusters which contain all of the energy deposited in the calorimeter. Each super-cluster has a one block overlap at all interior boundaries. The 40 super-cluster signals are fanned out 4 times to an integrator module, a FERA ADC, a FERA ADC after 100 ns of delay, and the fourth being unused. Once the super-cluster signals are integrated, the energy is then discriminated to select high transverse energy deposits. The discriminator levels are set according to the beam energy. The logical OR of the 5 super-ring signals for each super-wedge results in 8 logic signals. These CCAL octant signals are used to form topological trigger logic, e.g., 1 octant versus the OR of the opposite 3 octants. Further discussion of the trigger is found in Chapter 3.

The delayed super-cluster signals are used to determine the timing of CCAL signals. Each super-cluster event signal is timed to arrive 20 ns after the beginning of the 150 ns wide charge collection gate for the FERA ADCs. The charge in the delayed signals is collected for 100 ns with the last 50 ns overlapping the first 50 ns of the event gate. Comparison of the charge collected in both the delayed signal and event signal provides the basis for the timing of each event. A complete discussion of the pileup routines can be found in Gollwitzer's thesis [54, page 145].

CCAL Clustering

When a high energy electron or photon interacts with the lead glass of the calorimeter, a cascade or shower of photons and electrons is produced. The Čerenkov radiation produced in a block of glass is detected by the photomultiplier tube glued onto the back face of the block. The electromagnetic shower may produce signals in several blocks. A "cluster" is the set of signals produced by an electromagnetic shower. Cluster centers are single blocks with more energy than

their nearest neighbors. A cluster is a cluster center along with its 8 neighboring blocks which form a 3×3 grid.

The gains of the photomultiplier tubes were set so that the full scale on the FERA ADCs corresponded to $\sim$ 6 GeV. The nominal gain of the photomultiplier tubes found by requiring that π^0 masses be reconstructed for $\pi^0\pi^0$ events was $\sim$ 2.6 MeV/count. Pedestal events were taken with the beam on and the gas jet off to find the mean and full width at half the maximum value (FWHM) of the pedestal noise in each FERA ADC channel. Hardware pedestals were set at approximately twice the FWHM above the mean. Energies in each block were then calculated using the gain constants for each CCAL module.

All cluster position calculations are done in block units. The initial cluster position is found by taking the energy weighted position average for the 3×3 grid as in the equations

$$x = \frac{\sum_{i=1}^{9} E_i x_i}{\sum_{i=1}^{9} E_i} \quad y = \frac{\sum_{i=1}^{9} E_i y_i}{\sum_{i=1}^{9} E_i}$$

where $x(y)$ is the fractional ring(wedge) number and E_i is the energy deposited in the ith block. The origin, $(x, y) = (0, 0)$, corresponds to the center of the cluster center block. The coordinates, x_i and y_i, take on the values -1, 0, 1 which are the centers of the blocks surrounding the cluster center. Since most of the energy will be deposited in the central block, the distribution of shower positions determined by these averages will be biased toward the center of the central block.

The distributions of electrons and photons are not dependent on the block positions. Improvement of the energy weighted average position, (x, y), is obtained by a parameterization of the shower profiles,

$$|x'| = A_x(1 - e^{-\frac{|x|}{x_A}}) + B_x(1 - e^{-\frac{|x|}{x_B}})$$

$$|y'| = A_y(1 - e^{-\frac{|y|}{y_A}}) + B_y(1 - e^{-\frac{|y|}{y_B}}), \tag{2.2}$$

where A_x, A_y, B_x, B_y,x_A, x_B, y_A and y_B are determined by requiring that the x' and y' distributions are flat for each cluster from a sample of electrons from J/ψ events.

A correction for the energy lost in the steel between glass blocks is made using the formula,

$$E_{\text{corrected}} = \frac{E_{\text{measured}}}{(1 - C_{R\pm}e^{-|x''|/x_{R\pm}})(1 - C_{W1}e^{-|y''|/y_{W1}} - C_{W2}e^{-|y''|/y_{W2}})}, \tag{2.3}$$

with x'' and y'' the corrected cluster positions in block number measured from the edge of the block. The first term in the denominator corrects the shower energy in the ring direction with $C_{R+}(C_{R-})$ and $x_{R+}(x_{R-})$ are parameters for the upstream(downstream) edges of the block. The second term in the denominator corrects the shower energy in the wedge direction. All the parameters for the position and energy corrections are in Table 2.7.

CCAL Clustering Parameters

Parameter	Value	Parameter	Value
A_x	0.2601	A_y	0.3138
x_A	0.0321	y_A	0.0397
B_x	0.2574	B_y	0.1969
x_B	0.1860	y_B	0.1715
C_{R-}	0.0614	C_{W1}	0.1474
x_{R-}	0.1357	y_{W1}	0.0204
C_{R+}	0.0857	C_{W2}	0.1594
x_{R-}	0.0508	y_{W2}	0.0784

Table 2.7: See Equations 2.3.4 and 2.3.

The performance of the CCAL and the clustering algorithm was studied by comparing the charged tracking to the CCAL tracking [55]. Well defined electron

tracks are available from the interaction $\bar{p}p \rightarrow J/\psi \rightarrow e^+e^-$ and measured by the charged tracking with average resolutions of 2.5 mrad in both $\vartheta_{\rm lab}$ and $\phi_{\rm lab}$. Taking into account the charged tracking resolutions, the average position resolutions for the CCAL tracking are found to be 6.2 and 12.5 mrad for $\vartheta_{\rm lab}$ and $\phi_{\rm lab}$ respectively. Using the restrictions of two body kinematics to predict the energy of each electron from the angular measurements, the average CCAL energy resolution is found to be 4.3% for 2.5 GeV electrons.

Chapter 3

Data Acquisition Hardware and Logic

The E760 detector consists of many different detector subsystems with a variety of different readout electronics. The readout electronics, data pathway, and the higher level logic formed from the data for each event are described in this chapter.

Although many considerations drove the development of the data acquisition, the primary goals were to provide accurate and flexible triggering, event filtering, and performance monitoring. In addition, these goals were to be met on a time scale appropriate to the expected 750 KHz interaction rate while providing for the readout of a variety of electronics.

The hardware discussion consists of two sections, readout and trigger electronics. The discussion of the E760 trigger also consists of two sections, detector level and trigger level logic.

3.1 Readout Electronics

The readout electronics for the E760 detector are compatible with the CAMAC standard. With only a few exceptions, the digitization of the analog signals from the detectors is performed by TDCs, ADCs, and latches or pattern units. There are two parallel CAMAC branch highways for a total of 14 CAMAC crates. A listing of these crates with the electronics residing in them is found in Table 3.1.

CAMAC Hardware Organization

CAMAC Crate	RBUF Address	Devices
A-1	1	Gatemaster, MLU, and logic pattern units
A-2	2	Charged trigger logic pattern units
B-3	3	Pb glass ADCs
B-4	4	Pb glass ADCs
B-5	5	Pb glass ADCs
B-6	6	Pb glass ADCs
A-3	7	FCAL ADCs, event number and event time modules, Pb glass sum ADCs
A-4	8	Strawtube ADCs and drift time readout, H1, H2, and Čerenkov ADCs, Accelerator information data buffer, forward strawtube TDCs
A-5	8	MWPC ADCs
A-6	8	MHFD readout for the RPC
A-7	8	MHFD readout for the RPC
B-1	8	LST ADCs
B-2	8	LST ADCs, RMH, and event scalers
B-7	*	This crate contains the neutral trigger logic for the CCAL and is not read out by the data acquisition system.

Table 3.1: The CAMAC crates with associated readout electronics, and indentification of the 8 RBUFs which receive the data from the SCC.

In addition to an A2 crate controller, Fermilab Smart Crate Controllers (SCC) reside in 13 of the CAMAC crates. These are auxiliary crate controllers which perform the data readout during data acquisition. Each SCC contains a cpu which polls for triggers arriving on the front panel trigger port. Control of the CAMAC backplane is then passed to an internal sequencer which performs one of up to 32 different readout lists depending on the arriving trigger. Use of the SCCs provides the capability of performing more than one trigger type depending on the state of the E760 detector.

Data from an SCC is sent to one of 8 VME-based double-buffered memory modules called RBUFs. Out of the 13 SCCs, 6 use a token passing scheme to move the data from CAMAC into one RBUF. The other 7 SCCs move the CAMAC data into separate RBUFs. The organization of the VME crate is given in Table 3.2. Also resident in the VME crate are 23 computers or cpus. These cpus and buffers constitute the hardware of a Fermilab ACP I parallel processor. The cpus read the current event in the RBUFs into local memory for analysis and reformatting of the data [54, page 125]. The analysis program running in the ACP I parallel processor appends a block of summary data to each event. Offline filtering is done using this summary data. Once the cpu has finished with the data, it signals a program running on a μVax II that its output buffer is full. This program then writes events to tape and moves events to a local area Vax cluster for detector monitoring. The front end μVax II also runs an online monitor program which plots the performance of the Antiproton Source and the data acquisition.

VME Crate Configuration

VME crate-slot	Module	VME crate-slot	Module
1-1	-	2-1	-
1-2	VRM	2-2	HVE
1-3	BBC	2-3	CPU
1-4	BVI	2-4	CPU
1-5	BBT	2-5	CPU
1-6	CPU	2-6	CPU
1-7	CPU	2-7	CPU
1-8	CPU	2-8	CPU
1-9	CPU	2-9	CPU
1-10	CPU	2-10	CPU
1-11	CPU	2-11	CPU
1-12	CPU	2-12	CPU
1-13	RBUF	2-13	CPU
1-14	RBUF	2-14	CPU
1-15	RBUF	2-15	CPU
1-16	RBUF	2-16	CPU
1-17	RBUF	2-17	CPU
1-18	RBUF	2-18	CPU
1-19	RBUF	2-19	CPU
1-20	RBUF	2-20	CPU
1-21	HVE	2-21	CPU

Table 3.2: Equipment location in the VME crates containing the ACP I generation parallel processor used by E760.

3.2 Trigger Electronics

Formation of the E760 trigger is performed by two modules built 'in house.' These modules are the Memory Lookup Units (MLUs) and the Gatemaster. There were no modules on the market that used the fastest static memory available when the MLU module was designed. A device did not exist for the triggering of the SCCs based on multiple inputs before the Gatemaster was built.

3.2.1 The Gatemaster

To begin the readout of the detector electronics, the SCCs must receive a trigger mask and the electronics must be gated. These two tasks are performed by a Fermilab built device called the Gatemaster Module. The Gatemaster priority encodes 16 inputs into a 5 bit trigger mask which is read by each SCC at its front panel trigger port. The 16 triggers input to the Gatemaster are found in Table 3.3. Four of the trigger inputs are determined by two MLUs, a topic which will be discussed in §3.4.

The triggers GM1, GM2, and GM3 are timed triggers read at clocked intervals independent of the reaction rate. GM1 is triggered every 5 minutes and records the output of a multichannel charge analyzer attached to the luminosity monitor. GM2 is triggered every 3 minutes and records the current accelerator data on the beam energy, profile, and orbit. GM3 is triggered every 5 minutes and records many scaled quantities associated with the detector subsystems.

The interaction or minimum bias trigger is GM8. Due to priority encoding by the Gatemaster, GM8 is triggered only if none of the clocked or physics triggers have occurred. Pedestal triggers, GM9, are only requested at the beginning of

Gatemaster Module Inputs

Gatemaster Input	Trigger description
GM1	Luminosity Monitor Readout
GM2	Accelerator Data (ACNET) Readout
GM3	Scaler Readout
GM4	Charged Physics Readout
GM5	Two-Body Hadronic Readout
GM6	Alternate Physics Readout
GM7	Neutral Physics Readout
GM8	Interaction Trigger
GM9	Test/Pedestal Trigger
GM10	Unused
GM11	FCAL Cosmic Ray Trigger
GM12	Pb Glass Pulser Trigger
GM13	Unused
GM14	Strawtube Calibration Pulser
GM15	Unused
GM16	Čerenkov Detector OR

Table 3.3: The 16 different triggers used by E760. They are priority coded with GM1 having the highest priority.

runtime before the gas jet is turned on and data taking actually begins but after the requested beam energy has been achieved. GM12 is triggered at 1/6 Hz and is the CCAL calibration monitor trigger. These data consist of the CCAL response to a flashlamp whose output is always compared to a ^{207}Bi source. GM11 and GM14 are the calibration triggers for the FCAL and strawtubes respectively.

In addition to the 5 bit trigger mask, the Gatemaster outputs eight TTL levels that go low when the Gatemaster is disabled by a trigger. These levels are used to generate input gates for the different digitizing electronics. Each SCC has an overhead cost of 30 μs between the receipt of a trigger and the beginning of the data readout. This overhead allows more than enough time for the generation of

input gates appropriate to each detector's integration time. The Gatemaster remains disabled until each of the 13 SCCs has finished transferring data from CAMAC into the ACP.

3.2.2 The Memory Lookup Unit

The MLU is a single width CAMAC module which accepts ECLine compatible signals and provides four NIM signals as outputs. The central feature of the module consists of four static CMOS RAMs. These 64Kx1 memories have an access time of $\sim$ 12ns. The ECL input is strobed into latches which drive the address lines of the RAMs. A delayed version of the strobe gates the output of the memories. Internal potentiometers provide adjustments for the total time delay of the module and the width of the four output NIM signals. The minimum total board delay is 33ns with a 5 ns strobe. There is also a buffered output of the ECL inputs.

The 4 memories are programmed with 64K, four bit words from CAMAC. Each MLU module is tested by programming the memories, after which each memory address is accessed randomly and checked for the correct response. The MLU, when working, is 100% efficient, i.e. any failure of the MLU is catastrophic. The MLUs used in the E760 trigger used a 5ns strobe with the total board delay being set to 45ns. With these settings, the MLUs operate at a strobe rate of 1KHz with a live time factor of 99.995%.

Programming the E760 trigger into the MLU is simply done by deciding which of the 16 ECLine inputs the experimenter wants to be on, off, or not to matter. A program then calculates the subset of the 64K addresses that the experimenter wants to be defined as a trigger and writes a 1 to that memory

location. All other memory locations contain a zero. The 16 ECLine inputs represent detector level logic determined from coincidence of pattern unit data.

3.3 Detector Level Logic

The Detector Level Logic (DLL) for E760 exploits the azimuthal symmetry of the detector subsystems. By comparison of pattern unit data from the different detector subsystems, logic indicating tracks, clusters, coplanarity in the plane containing the beam direction, and electron tags can be developed. This logic is then used by the experimenter to design triggers for different event topologies.

h^+: This is the single arm topology, Figure 3.1, for charged particles as defined with the H1 and H2 hodoscopes. Four elements of the H2 hodoscope subtend the same azimuthal angle as one H1 element. Single arm topology is defined as the coincidence of an H1 element with any of the four corresponding H2 elements in addition to the two adjacent H2 elements. For h^+, this single arm topology is satisfied at least once.

h^+h^-: The single arm topology is satisfied at least twice.

#H1: The number of H1 elements that are above threshold in the event.

#H2: The number of H2 elements that are above threshold in the event.

e^+: Single arm topology with an associated Čerenkov element in coincidence.

e^+e^-: Same as e^+ satisfied at least twice.

COPL: An H2 element in coincidence with one of three H2 elements, the central one of the three being directly opposite in azimuthal angle.

FCHV: The forward charged veto detector logical OR is off.

FCAL: The forward calorimeter logical OR.

H1OR: The logical OR of all the H1 elements.

FCHOR: The logical OR of all the forward charged veto detector elements.

ETOT1: 80% of the total available energy is detected in the CCAL.

PBG1: One CCAL superwedge in coincidence with one of three other superwedges, the central one of the three being directly opposite in azimuthal angle.

PBG2: One CCAL superwedge in coincidence with the superwedge directly opposite in azimuthal angle.

CCAL: The logical OR of all the CCAL superblocks.

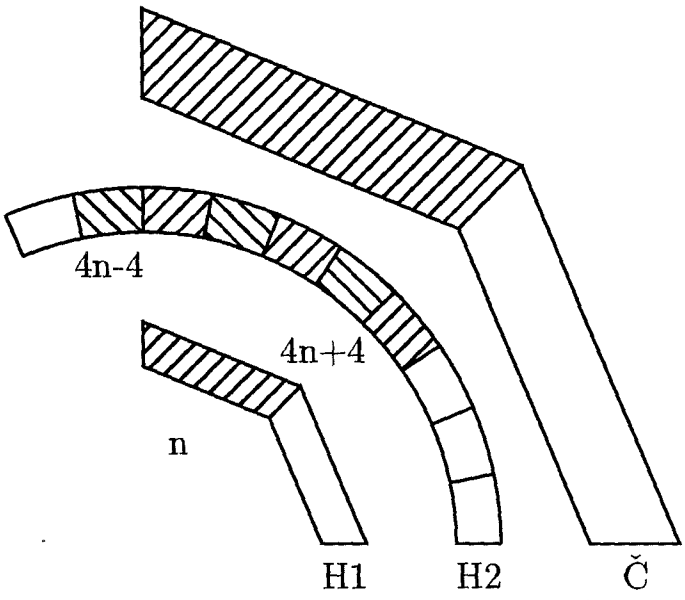

Figure 3.1: The coincidence between the hodoscopes and the Čerenkov detector which defines an electron track in the trigger.

3.4 Trigger Level Logic

The trigger level logic denotes the use of the detector level logic to develop the four different physics triggers. Two MLUs in series produce the four physics triggers GM4, GM5, GM6, and GM7. The 16 ECLine inputs for each MLU are

shown in Table 3.4. MLU1 has only charged detector level logic for inputs. The first eight inputs of MLU2 are the CCAL superwedge logic. There are several precalculated triggers based on these eight inputs that represent important expected event topologies.

- 1 opposite 1
- 1 opposite 3
- Any two adjacent superwedges.
- CCAL logical OR
- 1 e^+ psi trigger
- CCAL logical VETO
- unused
- no requirement on CCAL

Each of the MLUs has four outputs based on some logical combination of the detector level logic. Since the MLUs are connected in series, the final logic forming the four physics triggers can contain information from all the devices found in the trigger.

The first physics trigger, GM4, is designed for the detection of two large charged electromagnetic showers. At least one of the showers is required to be associated with a signal from the Čerenkov detector. In terms of detector level logic, GM4 is the logical OR of the following:

2Č: $(\mathrm{PBG1}) \otimes \#\mathrm{H1} \leq 4 \otimes \#\mathrm{H2} \leq 4 \otimes (\mathrm{h^+h^-}) \otimes (\mathrm{e^+e^-})$

1Č: $(\mathrm{PBG1}) \otimes \#\mathrm{H1} \leq 2 \otimes \#\mathrm{H2} = 2 \otimes (\mathrm{h^+h^-}) \otimes (\mathrm{e^+}) \otimes (\mathrm{COPL}))$

0Č: $\#\mathrm{H1} \leq 2 \otimes \#\mathrm{H2} = 2 \otimes \mathrm{FCHV} \otimes (\mathrm{h^+h^-}) \otimes (\mathrm{COPL})$

MLU ECLine Inputs

MLU1	MLU2
h^+	SUPERWEDGE # 1
h^+h^-	SUPERWEDGE # 2
#H2 = 2	SUPERWEDGE # 3
#H2 > 2	SUPERWEDGE # 4
#H2 = 2cluster	SUPERWEDGE # 5
#H2 > 4	SUPERWEDGE # 6
#H1 > 2	SUPERWEDGE # 7
#H1 > 4	SUPERWEDGE # 8
e^+	ETOT1
e^+e^-	unused
COPL	MLU1 #1
FCHOR	MLU1 #2
FCAL	MLU1 #3
unused	MLU1 #4
unused	FCHOR
unused	H1OR

Table 3.4: The detector level logic that is input to the MLUs.

The second physics trigger, GM5, is designed for the detection of hadronic two body final states. The CCAL responds poorly to hadrons and is not required in the trigger. A strict requirement on the multiplicity in H1 lowers the rate of this trigger. Still, GM5 is prescaled and is expressed in terms of detector level logic as:

- $h^+h^- \otimes \#\mathrm{H2} = 2 \otimes \#\mathrm{H1} \leq 2 \otimes (\mathrm{COPL}) \otimes \mathrm{FCHV} \otimes \overline{\mathrm{FCAL}}$

The third physics trigger, GM6, is reserved for trigger studies involving more complicated final state topologies of charged particles.

The fourth physics trigger, GM7, is designed for the detection of two large neutral electromagnetic showers or neutral events with more than 80% of the

available energy in the CCAL. By vetoing on the H1OR and the FCHOR, GM7 excludes most events with a charged particle in the final state. In terms of detector level logic, GM7 is the logical OR of the following:

- $(\mathrm{PBG1}) \otimes (\overline{\mathrm{FCHOR}}) \otimes (\overline{\mathrm{H1OR}})$
- $(\mathrm{ETOT1}) \otimes (\overline{\mathrm{ETOT2}}) \otimes (\overline{\mathrm{FCHOR}}) \otimes (\overline{\mathrm{H1OR}})$

Many of the triggers, GM1-GM16, have the same detector readout. But, for example, the neutral events do not readout each subsystem of the E760 detector. A list of the triggers and the CAMAC crates that are in the data readout is found in Table 3.5.

CAMAC Readout For Gatemaster Triggers

	CAMAC crate												
	A-1	A-2	B-3	B-4	B-5	B-6	A-3	A-4	A-5	A-6	A-7	B-1	B-2
GM1	√					√							√
GM2	√						√	√					√
GM3	√						√						√
GM4-6	√	√	√	√	√	√	√	√	√	√	√	√	√
GM7	√	√	√	√	√	√	√	√					
GM8,9	√	√	√	√	√	√	√	√	√	√	√	√	√
GM11	√						√						
GM12	√	√	√	√	√	√	√						
GM14	√						√	√					
GM16	√	√					√	√					

Table 3.5: The different triggers read out different CAMAC crates, Table 3.1. For GM7, only the H1, H2. and Čerenkov ADCs are read from crate A-4. GM10,13,15 are not used.

Chapter 4

Neutral Event Selection and Efficiencies

Experiment E760's scan of the η_c resonance consists of 11 sets of data taken at energies from 2.911 to 3.097 GeV. These neutral data are well understood with respect to trigger and selection efficiencies. This chapter discusses the selection criteria for $\gamma\gamma$ events. The resulting total efficiency, $\epsilon_{\text{total}} = \epsilon_{\text{selection}} * \epsilon_{\text{trigger}}$, for counting $\gamma\gamma$ events is presented.

4.1 The Data

The neutral trigger has both a software and hardware component. Written in terms of hardware logic, the hardware component of the neutral trigger is the logical OR of,

$$\text{PBG1} \otimes \overline{\text{H1OR}} \otimes \text{FCHV}$$

$$\text{ETOT} \otimes \overline{\text{H1OR}} \otimes \text{FCHV}\,.$$

The software component is a total energy calculation in the ACP processor which requires that ≈90% of the available energy is found in the central and forward calorimeters. Events with two clusters forming an invariant mass greater

than 2.5 GeV are written to the COM4 files. This selection criterion is calculated by the online filter routines and is represented by the first bit of the ACP neutral summary block in each event. The amount of data and the energy at which they were taken are found in Table 4.1

Energy and Luminosity

E_{cm} GeV	L (nb)$^{-1}$
2.9113	49.345
2.9501	197.845
2.9749	423.486
2.9792	163.482
2.9812	393.425
2.9855	201.151
2.9896	512.497
2.9940	310.126
3.0050	177.920
3.0497	119.863
3.0975	690.922

Table 4.1: The energies and luminosities for the data taken near the η_c resonance.

4.2 Selecting Events

The event selection is easily discussed in several parts. An event skimming procedure keeps events which have CCAL information consistent with two photons and enough information to safely calculate the twobody kinematics hypothesis. The SQUAW kinematic fitting program calculates the likelihood for the event to fit the twobody hypothesis. Background rejection is done by identifying π^0s and hodoscope multiplicity criteria.

The $\gamma\gamma$ events for each energy are counted. In the final sample

- CCAL Requirements

  1) there are only 2 clusters in the CCAL with energy greater than 100 MeV and labeled as ontime,
  2) the cluster masses of the two highest energy clusters are each consistent with a single photon, $20 \leq M_{cl} \leq 95\,\mathrm{MeV/c^2}$,

- Background Rejection

  3) there are no clusters found in the FCAL,
  4) the pattern unit data for hodoscope H1 indicates no signal,
  5) there are no combinations of the highest energy clusters with low energy clusters that have invariant masses consistent with the mass of the π^0, $80\,\mathrm{MeV/c^2} \leq M_{1\vee 2,j} \leq 170\,\mathrm{MeV/c^2}$,

- Kinematical Consistency

  6) all events fit to the twobody hypothesis with χ^2 fit probability at least 0.10.

The following sections describe these selection criteria in more detail.

4.2.1 CCAL Requirements

The data are analyzed using the standard E760 offline code with a cluster threshold of 20 MeV. An event must have at least two clusters with energies and angles measured by the CCAL to be minimally compatible with the twobody hypothesis. Events with

- at least two ontime clusters
- the two highest energy clusters having polar angles within the physical limits of the CCAL, $0.195 < \vartheta < 1.176$ radians

contain enough information to safely calculate the twobody hypothesis. This procedure also orders the found clusters in decreasing energy. The energies and angles of the two highest energy clusters are chosen to represent the two gamma rays. The cluster mass,

$$M_{cl} = \sqrt{\left(\sum_{i=1}^{9} E_i\right)^2 - \left(\sum_{i=1}^{9} \vec{p}_i\right)^2}$$

of each highest energy cluster is checked for consistency with a single photon. Here, E_i is the energy deposited in the ith block of the cluster and p_i is the momentum in the lab calculated using E_i and the laboratory coordinates of the center of the ith block. The test range of $20 - 95$ MeV/c^2 is empirically determined from a clean sample of $J/\psi \rightarrow e^+e^-$ events.

π^0 mesons which decay symmetrically into two photons are recognized with the cluster mass variable, M_{cl}. The upper limit of 95 MeV/c^2 removes events with symmetric π^0 decays and avoids splitting the cluster and then calculating the invariant mass of the resulting two clusters for the π^0 removal criterion.

The timing determination, as discussed on page 46, is accepted as correct for clusters with energy greater than 100 MeV. The accuracy of the pileup routines is found to be greater than 95% for clusters with energy greater than 100 MeV.

4.2.2 Background Rejection

Multiplicity requirements are made on the H1 hodoscope and the number of FCAL clusters. There must be no signals in the pattern unit for the H1 hodoscope

and no FCAL clusters above the standard 50 MeV threshold. The J/ψ data used for the efficiency calculation covers the same range of instantaneous luminosity as found in the η_c sample. As demonstrated in Reference [54, pp.182-196] thesis, the rate dependence of the H1 and FCAL is weak for the J/ψ data.

π^0 Removal

Any π^0s that populate an event are found by calculating a set of invariant masses and checking each element of this set for consistency with the mass of the π^0 meson. After the CCAL clusters are ordered by decreasing energy, the set of invariant masses,

$$\{M_{i \vee j} : i = 1, 2; j = 3, \ldots, \text{number of clusters}\},$$

is calculated by pairing each of the two high energy clusters with each of the lower energy clusters in the event regardless of the timing determination. The mass window for rejecting an event is 80 to 170 MeV/c^2.

A further consideration is the efficacy of rejecting an event where the invariant mass found to be consistent with a π^0 meson is calculated using a cluster labeled out of time. For clusters truly not part of the event, such a rejection will only remove real signal. The distributions of invariant masses calculated at $\sqrt{s} = 2.990$ GeV are examined for a statistically significant π^0 signal in Figures 4.1 and 4.2. This study also revealed that removal of π^0s by this method is not completely independent of the χ^2 fit probability requirement.

Figure 4.1 reiterates that there are indeed events which contain π^0s at all levels of χ^2 fit probabilities considering only the ontime or undetermined clusters. Figure 4.2 indicates that while out of time clusters do combine to form π^0 masses, the effect is much diminished for higher fit confidence levels.

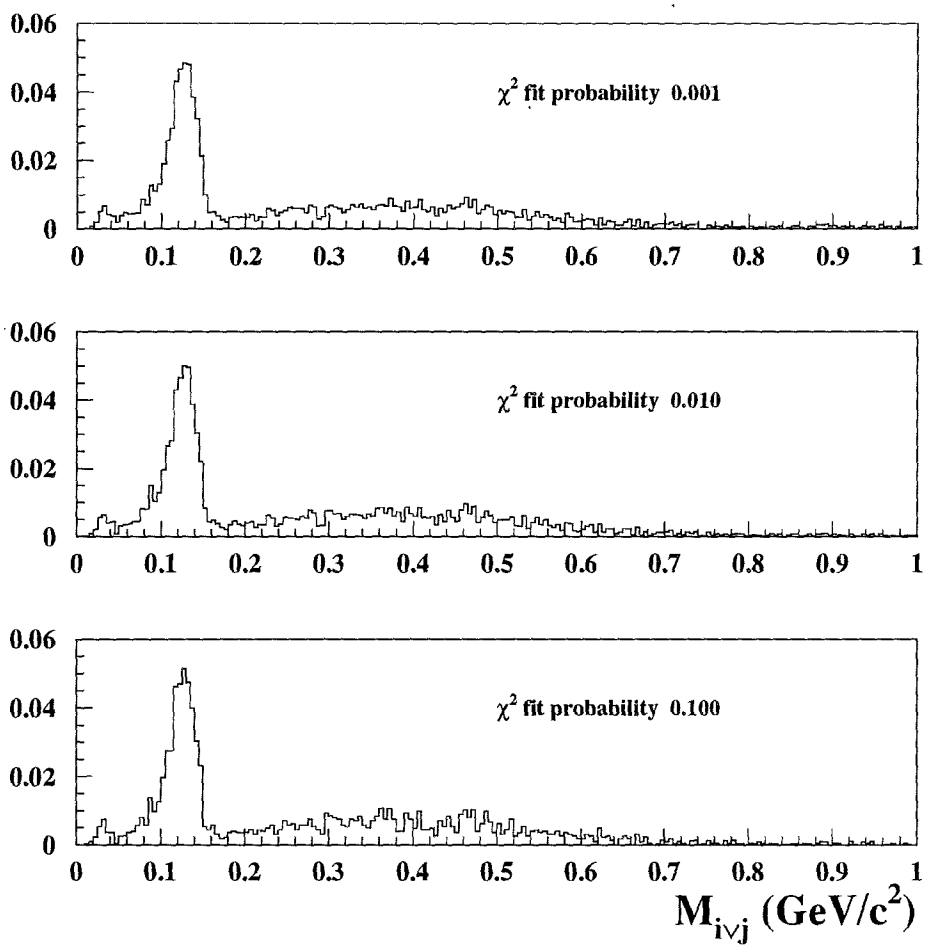

Figure 4.1: The distribution of the invariant mass combinations for ontime or undetermined clusters. The data are from the COM4 sample at $\sqrt{s} = 2.990$(GeV).

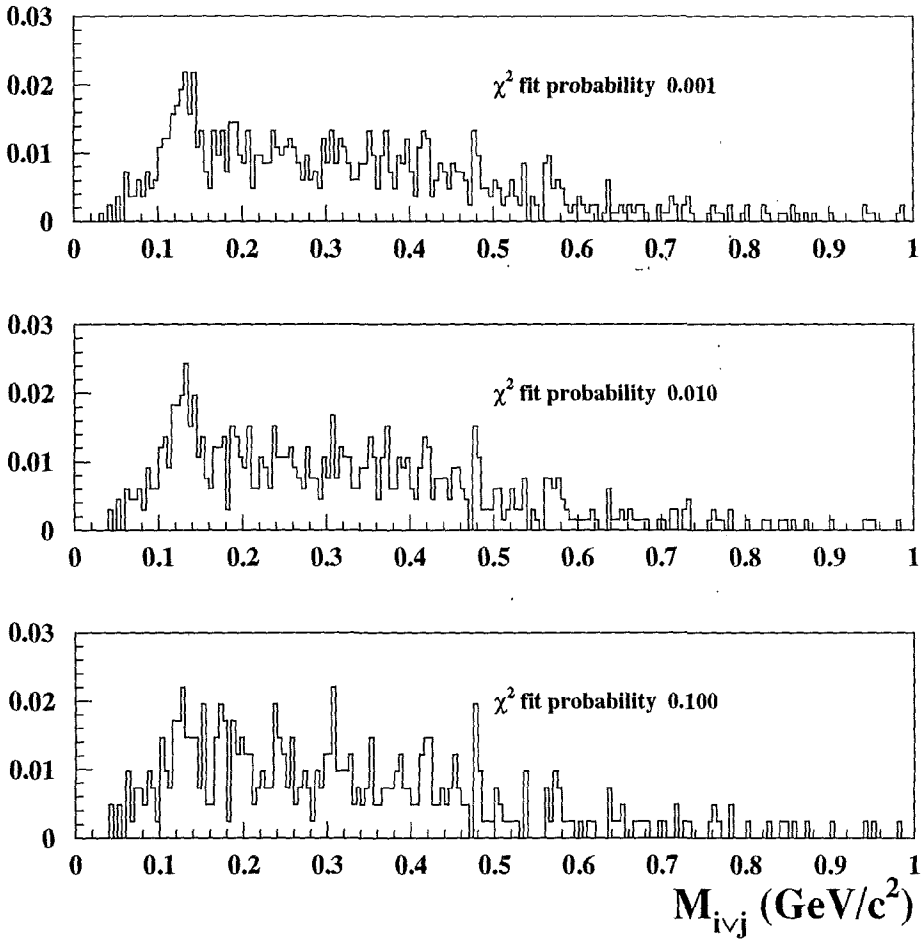

Figure 4.2: The distribution of the invariant mass combinations for out of time clusters. The data are from the COM4 sample at $\sqrt{s} = 2.990$(GeV).

4.2.3 Kinematical Consistency

The energies and angles of the two highest energy clusters in the event and the $\bar{p}$ laboratory momentum for the run containing the event represent the starting point for the SQUAW fitting routines. These routines were developed for bubble chamber experiments and modified to work for E760. The energy resolution and angular errors of the 6 CCAL measurements are supplied to SQUAW as a diagonal matrix.

$$\frac{\sigma_E}{E} = 0.30(Z_{\text{corr}} - 1) + \frac{0.05}{\sqrt{E}} + \frac{0.005}{E}$$

$$\sigma_\vartheta = 4 \text{ mrad}$$

$$\sigma_\phi = 7 \text{ mrad}$$

The term Z_{corr} is a multiplicative correction to the shower energy that compensates for losses in the steel between glass blocks. The $\bar{p}$ laboratory momentum is taken to be an exact measurement. The 4 constraint χ^2 fit probability is required to be at least 0.10. The absolute value of the polar angle in the center of mass is calculated using the best fit laboratory energies.

$$|\cos(\vartheta^*)| = \frac{1}{\beta}\frac{|E_1 - E_2|}{(E_1 + E_2)}$$

In the above equation, β is the magnitude of the velocity of the center of mass in the laboratory.

A fiducial limit of $x \equiv |\cos(\vartheta^*)| \leq 0.5$ is initially imposed on the data. This is the limit to the validity of the background determination presented in the next chapter.

4.3 Efficiencies

The combined selection and trigger efficiencies determine the effective luminosity of the final data sample. The invariant mass cut imposed on the raw data to make the COM4 data sample has a selection efficiency of one. The trigger efficiency is calculated at each energy. At each energy, the effective luminosity is a measured input of the likelihood function.

4.3.1 Selection Efficiencies

The study of the selection efficiency begins with the determination of an appropriate background free sample of J/ψ's. Such a background free sample can be made using the criteria:

- $0.01 \leq$ #H2mips ≤ 1.7, the number of minimum ionizing particles per large energy cluster as determined by the hodoscope H2 is consistent with one.
- $0.75 \leq$ #Čpes ≤ 30.0, the number of photo-electrons per large energy cluster as determined by the Čerenkov detector is consistent with a signal produced by one electron.
- both electrons have a measured polar angle in the lab within the range, $0.26 \leq \vartheta \leq 1.04$ radians.

The cuts were chosen to give a clean sample of J/ψs independent of any CCAL measurement. From a sample of 4583 J/ψ events, 3129 events pass the selection criteria for $\gamma\gamma$ events. The selection efficiency, $\epsilon_{\text{selection}}$, is 0.683 ± 0.007.

Criterion 4 in Table 4.2 corresponds to the fourth selection criterion for $\gamma\gamma$ events in the neutral trigger as stated in §4.2. The efficiencies of criteria 3 and 4 in

Selection Efficiencies

4583 J/ψ events total

Criterion	Number	Efficiency
1 (CCAL = 2)	4478	0.977
2 (single photons)	4532	0.989
3 (FCAL = 0)	4327	0.944
4 ($\#H1 \leq 2$)	4298	0.938
5 (π^0 removal)	4202	0.917
6 (fit prob > 0.10)	3779	0.825

Table 4.2: Comparing the product of the efficiencies, 0.647, to the whole selection efficiency, 0.683, indicates correlations between the criteria at the level of ~3%.

Table 4.2 are clearly dependent on the frequency of extra clusters or charged tracks which may be different for the charged and neutral triggers. Figures 4.3 and 4.4 show that the sample of clean J/ψs is relevant to the efficiency calculation for criteria 3 and 4.

More on π^0 Removal

The efficiency calculation for the π^0 removal criterion can be checked with a Monte Carlo simulation.

- Simulation Procedure

  1) analyze the η_c sample for events satisfying all the selection criteria
  2) generate 2 photons which satisfy 2 body kinematics for the event energy
  3) pair the generated photons with the lower energy clusters in the event

By counting the number of events with a π^0 mass found, the inefficiency for the π^0 removal criterion is determined to be 0.06 ± 0.02. This number is consistent with the efficiency calculated in Table 4.2 (criterion # 5).

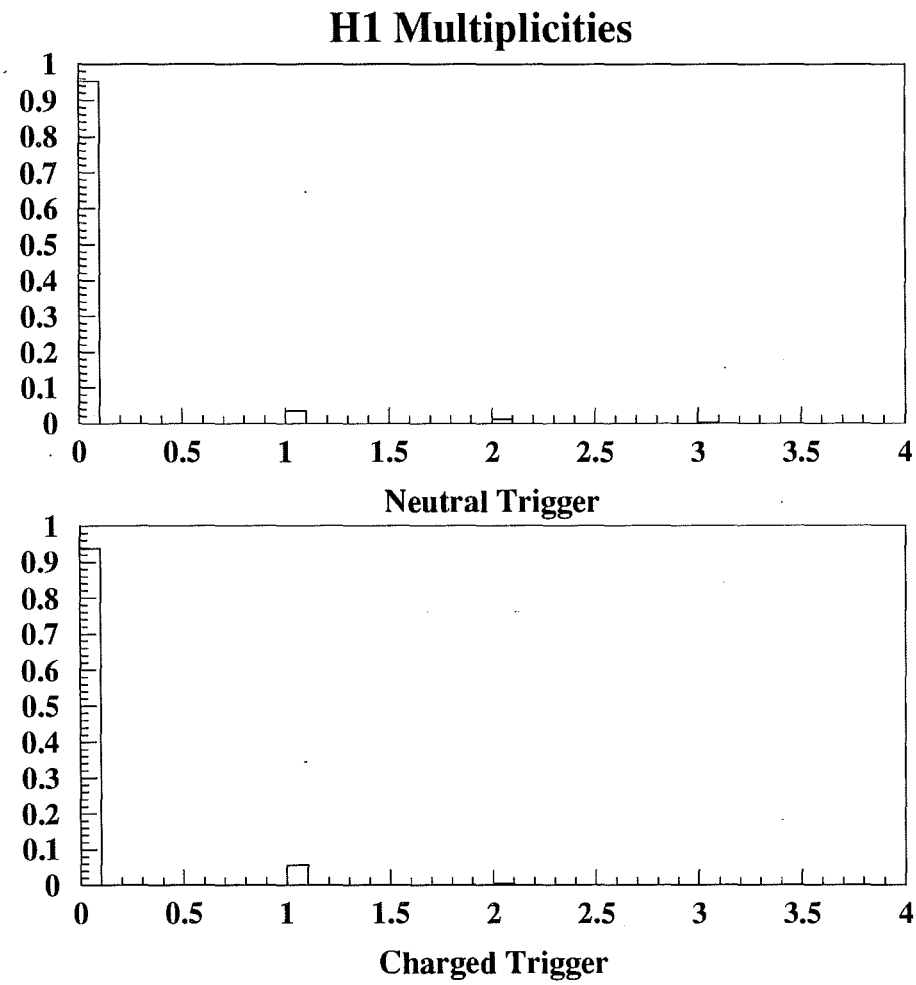

Figure 4.3: The sample of events consists of the neutral and charged trigger for all 1991 J/ψ runs. The events satisfy selection criteria 2 and 6. (#H1 - 2) is histogramed for the charged trigger.

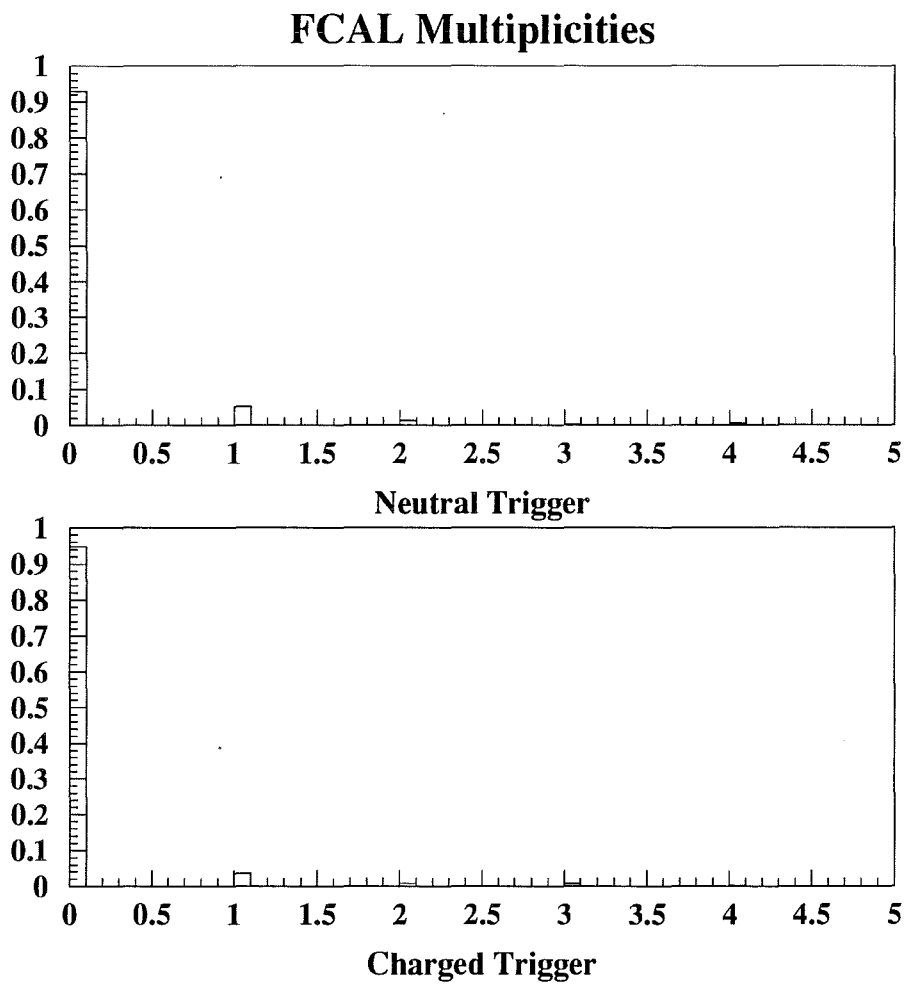

Figure 4.4: The sample of events consists of the neutral and charged trigger for all 1991 J/ψ runs. The events satisfy selection criteria 2 and 6.

4.3.2 Trigger Efficiencies

The neutral trigger can be divided into two subclasses of events, those satisfying the PBG1 logic and those satisfying the ETOT logic. The efficiency of the hardware and software logic is calculated from the tables in a previous memo [56]. This information is summarized in Table 4.3.

Neutral Trigger Efficiencies

$\sqrt{s}$(GeV)	ϵ_{PBG1}	ϵ_{ETOT}	ϵ_{ACP}	$\epsilon_{\text{trigger}}$	$\epsilon_{\text{total}} = \epsilon_{\text{selection}} * \epsilon_{\text{trigger}}$
2.9113	0.9895	0.7446	0.9859	0.928	0.634
2.9501	0.9937	0.9831	0.9842	0.934	0.638
2.9749	0.9957	0.9213	0.9751	0.932	0.637
2.9792	0.9952	0.9743	0.9864	0.934	0.638
2.9812	0.9950	0.9619	0.9765	0.933	0.637
2.9855	0.9953	0.9583	0.9808	0.933	0.637
2.9896	0.9968	0.7963	0.9672	0.927	0.633
2.9940	0.9957	0.9232	0.9876	0.933	0.637
3.0050	0.9952	0.9468	0.9591	0.832	0.568
3.0497	...	...	...	0.931	0.636
3.0975	0.995	0.929	0.958	0.931	0.636

Table 4.3: The trigger bit efficiencies for the ACP, PBG1, and ETOT trigger logic are tabulated. The efficiency of the FCHV bit based on random hits in the forward charged veto detector is 0.967 and is used along with the selection efficiency, 0.683, to calculate the total trigger efficiency, $\epsilon_{\text{trigger}}$.

A sample of $\pi^0\pi^0$ events is used to calculate the efficiency of the PBG1, ETOT, and ACP trigger logic found in Table 4.3. These $\pi^0\pi^0$ events satisfy the following criteria.

- only 4 CCAL clusters consistent with the timing of the event
- π^0 kinematics, $|\Delta\vartheta| < 0.020$ and $|\Delta\phi| < 0.040$ radians

The $\pi^0\pi^0$ events, for which the PBG1 trigger logic is reconstructed using the recorded information, are counted. The fraction of these events which also satisfy the hardware calculation of the PBG1 logic is the trigger efficiency for the PBG1 logic, ϵ_{PBG1}.

$$\epsilon_{\mathrm{PBG1}} = \frac{\#\pi^0\pi^0 \text{ reconstructed and hardware logic}}{\#\pi^0\pi^0 \text{ reconstructed logic}}$$

The ETOT trigger logic should be present in every $\pi^0\pi^0$ event. Specifically, the ETOT trigger logic should be present for those events which satisfy the PBG1 trigger logic. The fraction of these events with additionally satisfy the ETOT trigger logic is the trigger efficiency for the ETOT trigger logic, ϵ_{ETOT}.

$$\epsilon_{\mathrm{ETOT}} = \frac{\#\pi^0\pi^0 \text{ PBG1 and ETOT hardware logic}}{\#\pi^0\pi^0 \text{ PBG1 hardware logic}}$$

In addition to calculating a total energy, the ACP processor also tags events in which two π^0 masses are found. The π^0 mass test range is 105 to 165 MeV/c^2. The number of events in the $\pi^0\pi^0$ test sample with this tag are counted. The fraction which have the ACP total energy trigger logic is the trigger efficiency ϵ_{ACP}.

$$\epsilon_{\mathrm{ACP}} = \frac{\#\pi^0\pi^0 \text{ ACP two } \pi^0 \text{ and ACP total energy}}{\#\pi^0\pi^0 \text{ ACP two } \pi^0}$$

Another factor in the determination of the total trigger efficiency is the photon conversion probability in the material before the H1 hodoscope. A $\gamma\gamma$ event with both photons converting to e^+e^- pairs in this material will be lost to the charged trigger, GM4. A Monte Carlo simulation [57] has determined the conversion probability for each photon to be $\rho_{\mathrm{conv}} = 0.017$. Taking this consideration into account and making sure not to double count the PBG1 and ETOT classes of events, the neutral trigger efficiency is written as,

$$\epsilon_{\mathrm{trigger}} = (\epsilon_{\mathrm{PBG1}} * \epsilon_{\mathrm{ACP}} + \epsilon_{\mathrm{ETOT}} - \epsilon_{\mathrm{PBG1}} * \epsilon_{\mathrm{ACP}} * \epsilon_{\mathrm{ETOT}}) * \epsilon_{\mathrm{FCHV}} * (1 - \rho_{\mathrm{conv}})^2 .$$

The efficiency of the $\overline{\text{H1OR}}$ hardware logic is not included in the calculation of the neutral trigger efficiency. Selection criterion #4, no H1 hodoscope elements counted by the pattern unit, accepts the class of events that satisfy the $\overline{\text{H1OR}}$ hardware logic. The total efficiency would be underestimated by a factor of 0.933 were the efficiencies for both the H1 hardware trigger logic and selection criterion included.

The efficiency for the FCHV trigger logic is calculated using a clean sample of J/ψ events. For the same reason that the $\overline{\text{H1OR}}$ hardware logic is excluded from the calculation of the neutral trigger efficiency, the FCHV logic could also be excluded. The final sample of events does not change if a restriction on the FCHV pattern unit is imposed. Therefore, labelling the efficiency associated with the FCHV detector as trigger or selection is arbitrary.

The $\gamma\gamma$ events that are selected by the trigger and this offline analysis are contaminated with background events. These background processes have been estimated at each energy as differential cross sections which indicate that a limit to the fiducial volume in the form of a limit on the value of $|\cos(\vartheta^*)|$ is necessary to optimize the signals for $\eta_c \to \gamma\gamma$ and $\bar{p}p \to \gamma\gamma$. The next chapter discusses the background determination and how the $|\cos(\vartheta^*)|$ limit is chosen.

Chapter 5

Background Estimation and Likelihood Analysis

Extensive effort has been expended to determine the background contamination in the $\gamma\gamma$ differential cross section measured by E760. This background is found to consist primarily of the processes

$$\bar{p}p \rightarrow \pi^0\pi^0 \text{ , and } \bar{p}p \rightarrow \pi^0\gamma$$

being misidentified as $\bar{p}p \rightarrow \gamma\gamma$. The details of the cross section measurement of these processes at E760 are found elsewhere. Using a simulation of the CCAL, the feeddown into the $\gamma\gamma$ measured differential cross section is estimated. A history and some details of the feeddown calculation can be found in [58],[59], and [60].

The background differential cross sections are calculated at every energy for $|\cos(\vartheta^*)| \leq 0.5$ in bins of $\Delta|\cos(\vartheta^*)| = 0.05$. These histograms are well parameterized with a four parameter even polynomial. In addition to the statistical uncertainty on each bin due to the measured $\pi^0\pi^0$ and $\pi^0\gamma$ cross sections, there exists an uncertainty in the normalization of the background differential cross sections.

A crucial issue in the analysis of the E760 neutral data is the choice of fiducial volume. The E760 detector is azimuthally symmetric and the polar geometry was

selected to be symmetric around $\cos(\vartheta^*) = 0$ in the center of momentum coordinates at the J/ψ resonance. Therefore, the choice of fiducial volume is equivalent to the choice of an upper limit to $|\cos(\vartheta^*)|$, x_c. One choice of x_c would be the value of $|\cos(\vartheta^*)|$ at which the total expected signal to background ratio is maximized. This method does not take into account the errors in the estimation of the background differential cross section. By minimizing the total error on the best estimate of the signal with respect to x_c, the choice of x_c will be sensitive to the errors made in the estimation of the background differential cross sections.

Finally, a likelihood analysis for the η_c resonance parameters and the $\gamma\gamma$ continuum cross section is presented.

5.1 Measurement of the $\pi^0\pi^0$ and $\pi^0\gamma$ differential cross sections

The neutral E760 data are analyzed for $\pi^0\pi^0$ and $\pi^0\gamma$ events using a 50 MeV threshold on the total energy of CCAL clusters. Events satisfying the following criteria are labeled $\pi^0\pi^0(\pi^0\gamma)$ events.

- There are only 4(3) CCAL clusters labeled as ontime or undetermined.
- $|\Delta\phi| < 30$ mrad, $\Delta\phi = \pi - |\phi_1 - \phi_2|$ where ϕ_1 and ϕ_2 are the azimuthal angles of the two reconstructed final state bodies.
- $|\Delta\vartheta| < 11$ mrad, $\Delta\vartheta = \vartheta_1 - \vartheta_{1\,\mathrm{comp}}$ where ϑ_1 is the measured laboratory angle of the most energetic final state body and $\vartheta_{1\,\mathrm{comp}}$ is the same angle computed using the measured direction of the lower energy final state body.
- Coalesced photons, as determined by the criteria $M_{cl} > 100$ MeV/c^2, are always accepted as π^0s. Asymmetric decays of the π^0 into photons must

satisfy $|M_{\pi^0} - 135| < 35$ MeV/c^2 to be labeled as π^0s, where M_{π^0} is the invariant mass of two CCAL clusters in the event.

- A volume cut, $0.201 < \vartheta_{\text{clust}} < 1.13$ rad, eliminating clusters centered at the edges of the CCAL is made.

There are several possible assignments of clusters to the final state bodies. The assignment that minimizes,

$$(\Delta\vartheta)^2 + (\Delta\phi)^2$$

is taken to be the correct assignment.

$\partial\sigma_{\pi^0\pi^0}/\partial|\cos(\vartheta^*)|$

For the $\pi^0\pi^0$ sample, the distribution in the variable $\Delta\vartheta$ clearly shows a flat background. This background is estimated and the final event sample is corrected. Using this final event sample, the $\pi^0\pi^0$ differential cross section is calculated with Equation 5.1.

$$\frac{\partial\sigma_{\pi^0\pi^0}}{\partial|\cos(\vartheta^*)|} = \frac{\Delta N_{\pi^0\pi^0}}{L_{\pi^0\pi^0} P_{\pi^0\pi^0} F_{\pi^0\pi^0} \Delta|\cos(\vartheta^*)|} \tag{5.1}$$

Here, $L_{\pi^0\pi^0}$ is the integrated luminosity, $\Delta N_{\pi^0\pi^0}$ is the number of events in each $|\cos(\vartheta^*)|$ bin, and $F_{\pi^0\pi^0}$ is the total detection efficiency which is generally defined for both $\pi^0\pi^0$ and $\pi^0\gamma$ events in Equation 5.2.

$$F_{xx} = f_{\text{Dalitz}}(xx) \times f_{\text{conv}}(xx) \times f_{\text{trig}}(xx) \times f_{\text{pass}}(xx) \tag{5.2}$$

$f_{\text{Dalitz}}(xx)$ is the probability that the final state xx does not contain a Dalitz decay, $f_{\text{Dalitz}}(\pi^0\pi^0) = (1 - 0.01198)^2 = 0.976$, $f_{\text{Dalitz}}(\pi^0\gamma) = 0.988$

$f_{\text{conv}}(xx)$ is the probability that the final state xx does not contain a photon conversion before the H1 hodoscope ($f_{\text{conv}}(n\gamma) = (1 - 0.011)^n$).

$f_{\text{trig}}(xx)$ is the trigger efficiency for channel xx.

$f_{\text{pass}}(xx)$ is the first pass selection efficiency for the xx final state (only for $\pi^0\pi^0$ and $\pi^0\gamma$)

The acceptance and reconstruction efficiency, $P_{\pi^0\pi^0}$, is initially set to unity. A Monte Carlo simulation of the CCAL is then used to calculate the acceptance and reconstruction efficiency as a function of $\cos(\vartheta^*)$. The shape of the EM shower and the pedestal fluctuation in the CCAL counters are simulated,[60].

The $\pi^0\pi^0$ events are generated with a flat $\cos(\vartheta^*)$ distribution and a weight analog to the $\pi^0\pi^0$ differential cross section is assigned to each event based on the value of $\cos(\vartheta^*)$. After the simulated events are analyzed, the resulting $\cos(\vartheta^*)$ distribution is divided by the generated distribution to determine a new value for the acceptance and reconstruction efficiency, $P_{\pi^0\pi^0}$, in each $\cos(\vartheta^*)$ bin. The $\pi^0\pi^0$ differential cross section is then calculated again using Equation 5.1. The procedure is then repeated until the differential cross sections do not change,[59].

$\partial\sigma_{\pi^0\gamma}/\partial|\cos(\vartheta^*)|$

The simulated $\pi^0\pi^0$ events are also reconstructed using the $\pi^0\gamma$ analysis. The same procedure previously described for $P_{\pi^0\pi^0}$ is used to calculate, as a function of $\cos(\vartheta^*)$, the probability, $P^{\pi^0\pi^0}_{\pi^0\gamma}$, that $\pi^0\pi^0$ events will be reconstructed as $\pi^0\gamma$ events. The second term in Equation 5.3 is the contamination of the $\pi^0\gamma$ final state by the $\pi^0\pi^0$ final state with $F^{\pi^0\pi^0}_{\pi^0\gamma}$ representing the efficiency for detecting the $\pi^0\pi^0$ final state as a $\pi^0\gamma$.

$$\frac{\partial\sigma_{\pi^0\gamma}}{\partial|\cos(\vartheta^*)|} = \left[\frac{\Delta N_{\pi^0\gamma}}{L_{\pi^0\gamma}\Delta|\cos(\vartheta^*)|} - \frac{\partial\sigma_{\pi^0\pi^0}}{\partial|\cos(\vartheta^*)|}P^{\pi^0\pi^0}_{\pi^0\gamma}F^{\pi^0\pi^0}_{\pi^0\gamma}\right]/P_{\pi^0\gamma}F_{\pi^0\gamma} \tag{5.3}$$
$$F^{yy}_{xx} = f_{\text{Dalitz}}(yy)\times f_{\text{conv}}(yy)\times f_{\text{trig}}(xx)\times f_{\text{pass}}(xx)$$

Starting with simulated $\pi^0\gamma$ events, the acceptance and reconstruction probability distribution for the $\pi^0\gamma$ final state, $P_{\pi^0\gamma}$, is calculated in the same manner as $P_{\pi^0\pi^0}$. The differential cross sections represented by Equations 5.1 and 5.3 can now be used to calculate the contamination of the $\gamma\gamma$ final state by the $\pi^0\pi^0$ and $\pi^0\gamma$ final states.

5.2 The $\gamma\gamma$ Background Differential Cross Section

To estimate the background to the $\gamma\gamma$ differential cross section from $\pi^0\pi^0$ and $\pi^0\gamma$ events, the Monte Carlo generated $\pi^0\pi^0$ and $\pi^0\gamma$ events are analyzed for events satisfying the $\gamma\gamma$ event hypothesis. The criteria used to define the $\gamma\gamma$ hypothesis are

- Background Rejection

  1) there are no clusters found in the FCAL,
  2) there are no combinations of the highest energy clusters with low energy clusters that have invariant masses consistent with the mass of the π^0, $80\,\mathrm{MeV/c^2} \leq M_{1\vee 2,j} \leq 200\,\mathrm{MeV/c^2}$,

- Kinematical Consistency

  3) all events fit to the twobody hypothesis with χ^2 fit probability at least 0.10.

The reconstruction probability distributions, $P_{\gamma\gamma}^{\pi^0\pi^0}$ and $P_{\gamma\gamma}^{\pi^0\gamma}$, are again calculated by iteratively applying a weight analog of the event distribution found in the

simulated data sample. Equation 5.4 is used to calculate the background differential cross sections.

$$\frac{\partial\sigma_{\rm BKG}}{\partial|\cos(\vartheta^*)|} = \left[\frac{\partial\sigma_{\pi^0\gamma}}{\partial|\cos(\vartheta^*)|}P^{\pi^0\gamma}_{\gamma\gamma}F^{\pi^0\gamma}_{\gamma\gamma} + \frac{\partial\sigma_{\pi^0\pi^0}}{\partial|\cos(\vartheta^*)|}P^{\pi^0\pi^0}_{\gamma\gamma}F^{\pi^0\pi^0}_{\gamma\gamma}\right]/P_{\gamma\gamma}F_{\gamma\gamma} \tag{5.4}$$

The detection efficiencies, $F^{\pi^0\pi^0}_{\gamma\gamma}$, $F^{\pi^0\gamma}_{\gamma\gamma}$, and $F_{\gamma\gamma}$, are calculated using Equations 5.3 and 5.2.

The background differential cross section is calculated at each energy. A χ^2 fit to an even polynomial of the form,

$$p(x) = p_1 + p_2x^2 + p_3x^4 + p_4x^6$$

where $x \equiv |\cos(\vartheta^*)|$, is done for each energy. An even polynomial is sufficient for the description of the background since two body S-wave kinematics is required in the selection criteria. The results for each energy are tabulated in Table 5.1. In

Background Polynomials

$p(x) = p_1 + p_2x^2 + p_3x^4 + p_4x^6$

E_{cm} GeV	p_1	p_2	p_3	p_4
2.9113	0.575	-17.98	557.4	-1615.
2.9501	0.372	-6.916	270.6	-647.8
2.9749	0.241	-4.421	217.5	-565.2
2.9792	0.284	-11.10	291.9	-743.2
2.9812	0.250	-4.224	205.9	-513.7
2.9855	0.327	-9.733	226.8	-507.8
2.9896	0.251	-6.876	244.4	-681.4
2.9940	0.207	-5.432	210.8	-534.3
3.0050	0.171	-1.035	85.15	-123.8
3.0497	0.196	-8.903	182.4	-467.7
3.0975	0.133	-3.296	94.49	-233.7

Table 5.1: The polynomial coefficients describing the background for the 11 energies at which data were taken in the E760 η_c resonance scan.

Figure 5.1, the calculated background differential cross section and polynomial fit

for $\sqrt{s} = 3097$ MeV are shown along with the contributions from the $\pi^0\gamma$ and $\pi^0\pi^0$ final states.

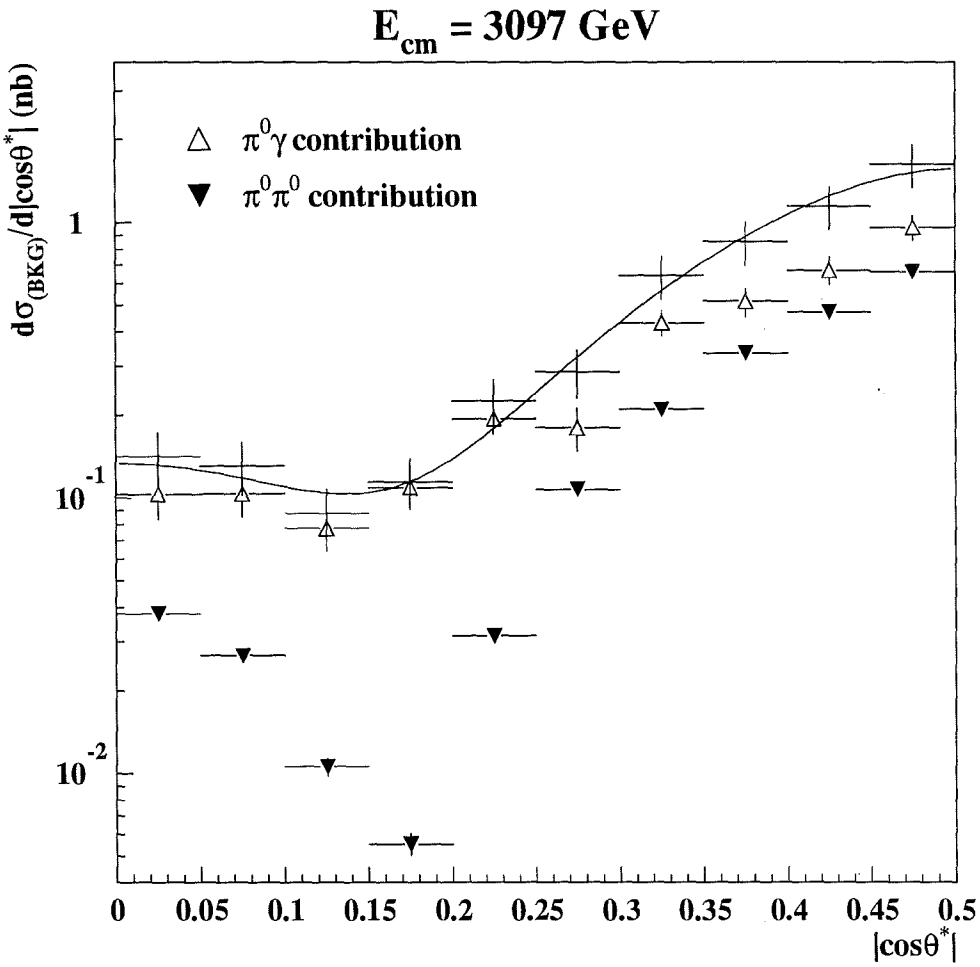

Figure 5.1: The calculated background for the data at $\sqrt{s} = 3097$ MeV. The contributions from the $\pi^0\gamma$ and $\pi^0\pi^0$ final states are shown separately.

The total number of events observed at each energy can now be described by the estimated background and physically motivated signal processes. For E760, the interesting signal processes in the data sample of $\gamma\gamma$ events are $\eta_c \to \gamma\gamma$ and $\bar{p}p \to \gamma\gamma$ which can be described as a function of energy and $|\cos(\vartheta^*)|$. The number of events labeled as background in the $\gamma\gamma$ sample is an estimate which has some

uncertainty. The following sections develop likelihood techniques for understanding this uncertainty and the effect on the fiducial volume.

5.3 Extended Maximum Likelihood and Fiducial Limits

A common class of estimation problem occurs when Poisson-generated events fall into two classes, signal or background, with the expected event distribution of one class known. For E760, the background differential cross section for $\gamma\gamma$ final states is estimated and the unnormalized event probability for $\gamma\gamma$ events,

$$F(x) = L\{g(x;\vec{a}) + b(x)\} \quad ,$$

is written as a function of $x \equiv |\cos(\vartheta^*)|$. The integrated luminosity, L, is an independently measured quantity and $\vec{a}$ will in general represent adjustable parameters describing the $\gamma\gamma$ signal event distribution, $g(x;\vec{a})$. The total number of background events is estimated from $b(x)$ as,

$$\mathcal{N}_{\mathrm{B}} = L \int_0^{x_c} dx\, b(x)\,,$$

where x_c represents the fiducial volume. The background event distribution is estimated, therefore systematic uncertainty in $\mathcal{N}_{\mathrm{B}}$ exists.

The systematic uncertainty in $\mathcal{N}_{\mathrm{B}}$ increases with increasing values of x_c and clearly decreases the accuracy of the signal measurement. With increasing values of x_c, more signal events are measured and the statistical accuracy of the signal measurement increases. These competing effects on the accuracy of the best estimate of signal processes can be computed within the framework of the extended maximum likelihood method (EMLM). The quadrature of these effects gives the total accuracy of the best estimate of the signal and will depend on x_c.

5.3.1 What is EMLM?

The EMLM was first proposed by Fermi and for many years Orear's Notes [61] has served as an introduction to the method. More recently, Barlow [62] has written an authoritative reference for the EMLM.

The standard maximum likelihood method (MLM) estimates a set of m unknown parameters $a_1, \ldots, a_m$ for N data values $x_1, \ldots, x_N$ observed by maximizing the likelihood

$$\mathcal{L} = \prod_{i=1}^{N} f(x_i; a_1 \cdots a_m) \ . \tag{5.5}$$

The probability density for the variable x is $f(x; a_1 \cdots a_m)$ and the best estimates $\hat{a}_1, \ldots \hat{a}_m$ are solutions of the equations

$$\sum_i \frac{\partial \ln f(x_i; a_1 \cdots a_m)}{\partial a_k} = 0 \quad \forall \quad k \ . \tag{5.6}$$

The probability density, $f(x; a_1 \cdots a_m)$, is normalized to unity.

$$\int dx \, f(x; a_1 \cdots a_m) = 1 \tag{5.7}$$

Relaxation of the normalization requirement is the essence of the EMLM.

The probability density, f, in Equation 5.7 is replaced with an unnormalized probability function F, where $dx \, F(x; a_1 \cdots a_m)$ is the absolute probability of getting an event in dx and the expected total number of events is

$$\overline{N} = \int_0^{x_c} dx \, F(x; a_1 \cdots a_m) \ . \tag{5.8}$$

The likelihood function in the EMLM for an ordered set of observations is

$$\mathcal{L} = \frac{e^{-\overline{N}}}{N!} \prod_{i=1}^{N} F(x_i; a_1 \cdots a_m) \ . \tag{5.9}$$

Analogous to the MLM, the expectation value of some statistic represented by a general function G is

$$\langle G \rangle = \sum_{N=1}^{\infty} \int \cdots \int dx_1 \cdots dx_N \, \mathcal{L}G(x_1 \cdots x_N) \; . \tag{5.10}$$

For expectation values in the EMLM, a summation over all normalizations is necessary since the absolute probability is not normalized. In the case of a simple function, as defined by Barlow [62],

$$G(x_1, \ldots, x_N) = \sum_{i=1}^{N} g(x_i) \tag{5.11}$$

the expectation will be

$$\begin{aligned}
\langle G \rangle &= \sum_{N=1}^{\infty} \int \frac{e^{-\overline{N}}}{N!} \prod_{j=1}^{N} dx_j \, F(x_j; a_1 \cdots a_m) \sum_{i=1}^{N} g(x_i) \\
&= \sum_{N=1}^{\infty} \left[\frac{e^{-\overline{N}}}{N!} \prod_{j \neq i} \int dx_j \, F(x_j) \right] \left[\sum_{i=1}^{N} \int dx_i \, F(x_i) g(x_i) \right] \\
&= \sum_{N=1}^{\infty} \left[\frac{e^{-\overline{N}}}{N!} \overline{N}^{N-1} \right] \left[N \int dx \, F(x; a_1 \cdots a_m) g(x)) \right] \\
&= \int dx \, F(x; a_1 \cdots a_m) g(x) \; ,
\end{aligned} \tag{5.12}$$

after substituting Equations 5.9 and 5.11 into Equation 5.10.

By using Equation 5.12, the expectation of the product of two simple functions may also be derived. Suppose that in addition to the simple function G, there is also a simple function, H, defined by

$$H(x_1, \ldots, x_N) = \sum_{i=1}^{N} h(x_i) \, .$$

To find $\langle GH \rangle$, first write

$$\left(\sum_j g(x_j) \right) \left(\sum_k h(x_k) \right) = \sum_k g(x_k) h(x_k) + \sum_{\substack{j,k \\ j \neq k}} g(x_j) h(x_k)$$

and then simplify by combining terms.

$$
\begin{aligned}
\langle GH\rangle &= \sum_{N=1}^{\infty}\int dx_1\cdots dx_N\,\mathcal{L}\sum_k g(x_k)h(x_k) \\
&\quad+\sum_{N=2}^{\infty}\int dx_1\cdots dx_N\,\mathcal{L}\sum_{\substack{j,k\\ j\neq k}} g(x_j)h(x_k) \\
&= \int dx\,F(x)g(x)h(x)+\sum_{N=2}^{\infty}\frac{e^{-\overline{N}}}{N!}\int\prod_i dx_i\,F(x_i)\sum_{\substack{j,k\\ j\neq k}} g(x_j)h(x_k) \\
&= \langle G\circ H\rangle \\
&\quad+\sum_{N=2}^{\infty}\frac{e^{-\overline{N}}}{N!}\int\prod_{\substack{i\neq k\\ i\neq j}} dx_i\,F(x_i)\sum_{\substack{j,k\\ j\neq k}}\int dx_j\,F(x_j)g(x_j)\int dx_k\,F(x_k)h(x_k) \\
&= \langle G\circ H\rangle \\
&\quad+\left[\sum_{N=2}^{\infty}\frac{e^{-\overline{N}}}{N!}\overline{N}^{N-2}\right]\left[N(N-1)\int dx\,F(x)g(x)\int dy\,F(y)h(y)\right] \\
&= \langle G\circ H\rangle+\left[\sum_{N=2}^{\infty}\frac{e^{-\overline{N}}}{(N-2)!}\overline{N}^{N-2}\right]\left[\int dx\,F(x)g(x)\int dy\,F(y)h(y)\right] \\
\langle GH\rangle &= \langle G\circ H\rangle+\langle G\rangle\langle H\rangle \qquad (5.13)
\end{aligned}
$$

The definition

$$\langle G\circ H\rangle\equiv\int dx\,F(x)g(x)h(x)$$

has been made to simplify notation.

An approximation to $\langle G/H\rangle$ can be made by using Equations 5.12 and 5.13 along with the definitions

$$\delta G\equiv G-\langle G\rangle \text{ and } \delta H\equiv H-\langle H\rangle \quad .$$

The ratio $\langle G/H\rangle$ can then be written as

$$\left\langle\frac{G}{H}\right\rangle=\left\langle\frac{\delta G+\langle G\rangle}{\delta H+\langle H\rangle}\right\rangle=\left\langle\frac{\delta G+\langle G\rangle}{\langle H\rangle\left(1+\frac{\delta H}{\langle H\rangle}\right)}\right\rangle \quad .$$

The approximation can be made by expanding the denominator in a series and keeping the first term. By definition, $\langle\delta G\rangle=0=\langle\delta H\rangle$ which simplifies the resulting

expansion to

$$\left\langle \frac{G}{H} \right\rangle \approx \frac{\langle G \rangle}{\langle H \rangle} - \frac{\langle \delta G \delta H \rangle}{\langle H \rangle^2} \quad .$$

Substituting the definitions of δG and δH and using the result in Equation 5.13, the approximation to $\langle G/H \rangle$ is written most simply as

$$\left\langle \frac{G}{H} \right\rangle \approx \frac{\langle G \rangle}{\langle H \rangle} \left[1 - \frac{\langle G \circ H \rangle}{\langle G \rangle \langle H \rangle} \right] \quad . \tag{5.14}$$

As will be seen in the subsequent sections, a physically meaningful EMLM probability is proportional to the integrated luminosity of the experiment. By counting the factors of integrated luminosity in Equation 5.14, the error term is seen to be inversely proportional to the integrated luminosity and is therefore expected to be small compared to unity.

The last general result for the EMLM which will be used is the asymptotic efficiency or the expected uncertainty, Δa, in a parameter a based on N measurements. For $F = F(x; a)$ with a some parameter, the asymptotic efficiency is,

$$(\Delta a)^2 = \left[\int_0^{x_c} dx \, \frac{1}{F} \left(\frac{\partial F}{\partial a} \right)^2 \right]^{-1} \quad . \tag{5.15}$$

Since the probability, $dx\, F(x)$, is not normalized, the number of observations, N, is not explicit in Equation 5.15. The explicit parameter which is related to the measurement statistics in Equation 5.15 is the fiducial limit, x_c.

5.3.2 Background Estimates in the EMLM

The EMLM probability for $\gamma\gamma$ events in E760 is written as:

$$F(x) = L\{g(x; \vec{a}) + b(x)\}. \tag{5.16}$$

Here L is the integrated luminosity, g is a signal event distribution as a function of $x \equiv |\cos(\vartheta^*)|$ with variable parameters represented by the vector $\vec{a}$. The

background event distribution is represented by $b(x)$ a polynomial which estimates the background event distribution.

The use of the EMLM will lead to the minimization of a log likelihood function.

$$-\log \mathcal{L} = \overline{N} + \log N! - \sum_{k=1}^{N} \log F(x_k) \tag{5.17}$$

with

$$\overline{N} = \int_0^{x_c} dx\, F(x) \tag{5.18}$$

where $\overline{N}$ is the total number of events expected with a $|\cos(\vartheta^*)|$ cutoff at x_c. The summation in Equation 5.17 is over N observed events at a particular energy. With little loss of generality, and certainly in the case of a ${}^1S_0$ Breit-Wigner resonance cross section, the signal distribution or cross section, $g(x;\vec{a}) = \sigma$, is assumed to be a constant with respect to x. The extremum of this log likelihood with respect to the signal, σ, is found by solving the equation

$$\frac{\partial(-log\mathcal{L})}{\partial\sigma} = 0 \tag{5.19}$$

which leads immediately to

$$\left.\frac{\partial\overline{N}}{\partial\sigma}\right|_{\sigma=\sigma^*} = \sum_{k=1}^{N} \frac{1}{F(x_k)} \left.\frac{\partial F(x_k)}{\partial\sigma}\right|_{\sigma=\sigma^*}.$$

The solution which satisfies this equation is the best estimate of the signal, σ^*. The derivatives can be written explicitly using Equations 5.16 and 5.18 as,

$$\left.\frac{\partial F}{\partial\sigma}\right|_{\sigma=\sigma^*} = L$$

and

$$\left.\frac{\partial\overline{N}}{\partial\sigma}\right|_{\sigma=\sigma^*} = \int_0^{x_c} dx \left.\frac{\partial F}{\partial\sigma}\right|_{\sigma=\sigma^*} = Lx_c \quad .$$

Making the appropriate substitutions and canceling the overall luminosity factor leaves,

$$x_c = \sum_{k=1}^{N} \left.\frac{1}{F(x_k)}\right|_{\sigma=\sigma^*}. \tag{5.20}$$

The value of x_c cannot be dependent on the value of the parameters, $\vec{p} = (p_1, \ldots, p_n)$, since the parameterization of the background is arbitrary. However, since σ^* clearly does depend on these parameters, $\partial\sigma^*/\partial p_j$, $j = 1, \ldots, n$ will be non-zero. Taking these considerations into account when differentiating Equation 5.20 with respect to the background parameters, p_j, gives the n equations

$$\frac{\partial x_c}{\partial p_j} = 0 = \sum_{k=1}^{N} \frac{\partial}{\partial p_j} \left(\frac{1}{F(x_k)} \right) \Bigg|_{\sigma=\sigma^*}$$

or

$$\sum_{k=1}^{N} \frac{1}{F^2} \frac{\partial F}{\partial p_j} \Bigg|_{\sigma=\sigma^*} = 0 \quad .$$

Now use Equation 5.16 to calculate $\partial F/\partial p_j$ and remember that $\partial\sigma^*/\partial p_j$ will be non-zero to get n equations which can be solved for each of the $\partial\sigma^*/\partial p_j$.

$$\frac{\partial \sigma^*}{\partial p_j} \sum_{k=1}^{N} \frac{1}{F^2} + \sum_{k=1}^{N} \frac{1}{F^2} \frac{\partial b(x)}{\partial p_j} \Bigg|_{x=x_k} = 0 \, , j = 1, \ldots, n \tag{5.21}$$

The desired quantity is the expectation value of $\partial\sigma^*/\partial p_j$ over many hypothetical experiments. This expectation value is found by first solving for $\partial\sigma^*/\partial p_j$ in Equation 5.21,

$$\frac{\partial \sigma^*}{\partial p_j} = - \frac{\sum_{k=1}^{N} \frac{1}{F^2} \frac{\partial b(x)}{\partial p_j} \Big|_{x=x_k}}{\sum_{k=1}^{N} \frac{1}{F^2}} \, , j = 1, \ldots, n \tag{5.22}$$

and averaging the result. Each sum in the right hand side of Equation 5.22 represents a simple function. The expectation of Equation 5.22 is well approximated by the ratio of the expectation values of the two sums. The error made by this approximation is estimated using Equation 5.14 and is found to be small. The final result for the expected values of the $\partial\sigma^*/\partial p_j$ is given in Equation 5.23.

$$\langle \frac{\partial \sigma^*}{\partial p_j} \rangle \cong - \frac{\int_0^{x_c} dx \, \frac{1}{F} \frac{\partial b(x)}{\partial p_j} \Big|_{x=x_k}}{\int_0^{x_c} dx \, \frac{1}{F}} \, , j = 1, \ldots, n \tag{5.23}$$

This variation with respect to the background parameters can now be used to estimate the total expected error in the best estimate of the signal, σ^*, due to errors in the background.

5.3.3 A Total Error on The Expected Signal

The function, $b(x)$ is a parametric fit to the background event distribution and there will be an associated error matrix, V_{ij}, $i, j = 1, \ldots, n$, for the parameters, p_j, $j = 1, \ldots, n$. Define the vector operator $\vec{\partial}_p$ as,

$$\vec{\partial}_p = \begin{pmatrix} \frac{\partial}{\partial p_1} \\ \frac{\partial}{\partial p_2} \\ \vdots \\ \frac{\partial}{\partial p_n} \end{pmatrix}.$$

The total expected error in the best estimate of the signal due to errors in the background can now be estimated as in Equation 5.24

$$(\Delta\sigma^*)^2_{\text{bkg}} \cong \langle \tilde{\vec{\partial}}_p \sigma^* \rangle V \langle \vec{\partial}_p \sigma^* \rangle \tag{5.24}$$

The value of x_c is not yet chosen. This is equivalent to not knowing how many data will be used in any succeeding analyses.

The best estimate of the statistical accuracy based only on the probability function, F, is found using Equation 5.15.

$$(\Delta\sigma^*)^2_{\text{stat}} = \left[\int_0^{x_c} dx \, \frac{1}{F} \left(\frac{\partial F}{\partial \sigma} \bigg|_{\sigma=\sigma^*} \right)^2 \right]^{-1} \tag{5.25}$$

Summing the contributions from Equations 5.24 and 5.25 in quadrature gives an estimate of the total error in the signal.

$$\begin{aligned} (\Delta\sigma^*)^2_{\text{total}} &= (\Delta\sigma^*)^2_{\text{stat}} + (\Delta\sigma^*)^2_{\text{bkg}} \\ &= \left[\int_0^{x_c} dx \, L^2 \frac{1}{F} \right]^{-1} + \langle \tilde{\vec{\partial}}_p \sigma^* \rangle V \langle \vec{\partial}_p \sigma^* \rangle \end{aligned} \tag{5.26}$$

Using Equation 5.16, the luminosity, L, is substituted for $\partial F/\partial\sigma$ in Equation 5.25 to explicitly show the dependence on the luminosity in Equation 5.26.

The dependence of $\Delta\sigma^*_{\text{total}}$ on the determination of the background is now explicit. The first term, $\Delta\sigma^*_{\text{stat}}$, decreases with increasing x_c and the second term changes with x_c according to Equation 5.23. The existence of a physical extremum depends on the relative size of these terms, making the determination of the background event distribution and the associated error matrix, V, of primary importance.

5.4 Background Estimation and Systematic Errors

Not only the values of the background parameters at each energy, but the respective error matrices are important. The associated error matrix for each set of fit parameters represents the correlations between the parameters describing the polynomial. Each of these error matrices can be modified to include systematic errors which arise from the determination of the background. Errors that are random uncertainties in the number of background events in each $|\cos(\vartheta^*)|$ bin are labeled as "incoherent" errors. Errors that are correlated uncertainties in the number of background events in each $|\cos(\vartheta^*)|$ bin are labeled as "coherent" errors. Coherent errors may, for example, correspond to a systematic change by the same percentage in each $|\cos(\vartheta^*)|$ bin. Once the dependence of the best estimator of the signal on each of the background parameters is calculated, the error matrix will be used to determine the contribution from the background model to the total error on the estimated signal.

There are several sources of systematic error which arise from the determination of the background. First there is a statistical error that is carried through from the measurements of the $\pi^0\gamma$ and $\pi^0\pi^0$ differential cross sections. This error is determined in the analysis leading to the background [59]. Two other important sources of systematic error are the actual CCAL cluster energy threshold and the determination of the feed down factors, $P^{yy}_{\gamma\gamma}$ and $F^{yy}_{\gamma\gamma}$, from the $\pi^0\gamma$ and $\pi^0\pi^0$ processes into the $\gamma\gamma$ cross section.

5.4.1 CCAL Energy Threshold

With a lower CCAL cluster energy threshold, more events are identified as background and excluded. By lowering(raising) the threshold, the background cross section is decreased(increased). The energy response of the CCAL [50, Figure 9] to photons with energy $\leq$ 100 MeV is known to be nonlinear. Also, for CCAL cluster energy thresholds between 50 MeV and 100 MeV, the ratio of background to signal in the data remains constant. A sample of low energy photons with energies sufficiently constrained by kinematics is not available from the data to make a study of the low energy response of the CCAL. However, electromagnetic showers from isolated low energy photons are mostly contained in one CCAL module and real shower fluctuations into a nearest neighbor module at the level of $\sim$ 5 MeV are not seen due to the pedestal subtracted readout of the CCAL. For a CCAL cluster energy threshold of 20 MeV, this 5 MeV corresponds to a 25% systematic error which is consistent with previous linearity studies [50, §4].

A determination [63] of the background differential cross section using a 25 MeV CCAL cluster energy threshold has been done for the data at 2975 MeV. There is a 12% increase in each $|\cos(\vartheta^*)|$ bin of the background differential cross

section when the CCAL cluster threshold is changed from 20 to 25 MeV. The bin by bin ratio of the differential background cross sections at $E_{\rm cm} = 2975$ MeV for CCAL cluster thresholds of 20 and 25 MeV are shown in Figure 5.2. Systematic errors in the CCAL cluster energy threshold will affect the background differential cross section coherently, *ie.* the central value of each $|\cos(\vartheta^*)|$ bin increases or decreases by the same amount. The value of 12% is an estimate of the FWHM of the distribution for the systematic error in the background cross sections due to the nonlinear low energy response of the CCAL.

5.4.2 $\pi^0\gamma$ Asymmetries

Systematic error in the feed down probabilities could be introduced by the Monte Carlo simulation and the method of calculation. An estimate of this error can be made by examination of the asymmetry in $\partial\sigma_{\pi^0\gamma}/\partial\cos(\vartheta^*)$ after the background estimate has been subtracted. The final background subtracted differential cross section is expected to be forward-backward symmetric according to charge conjugation symmetry. Figure 5.3 is a histogram of the signed asymmetries for the data used in the η_c analysis. The 110 entries (10 bins of $|\cos(\vartheta^*)|$ at each of 11 energies) are normally distributed around zero, indicating that this is an incoherent error. Each $|\cos(\vartheta^*)|$ bin is affected independently by this systematic error.

The average fractional statistical error of the background cross section measurement for $|\cos(\vartheta^*)| \leq 0.25$ is 19.4% and for $0.25 < |\cos(\vartheta^*)| \leq 0.50$ is 9.7%. An estimate of the asymmetry must take into account the statistical significance of the background cross section measurements in each $|\cos(\vartheta^*)|$ bin. One method is represented by Figure 5.4 which is an ideogram of the absolute value of the asymmetry in each $|\cos(\vartheta^*)|$ bin of the $\pi^0\gamma$ cross section at each energy in this

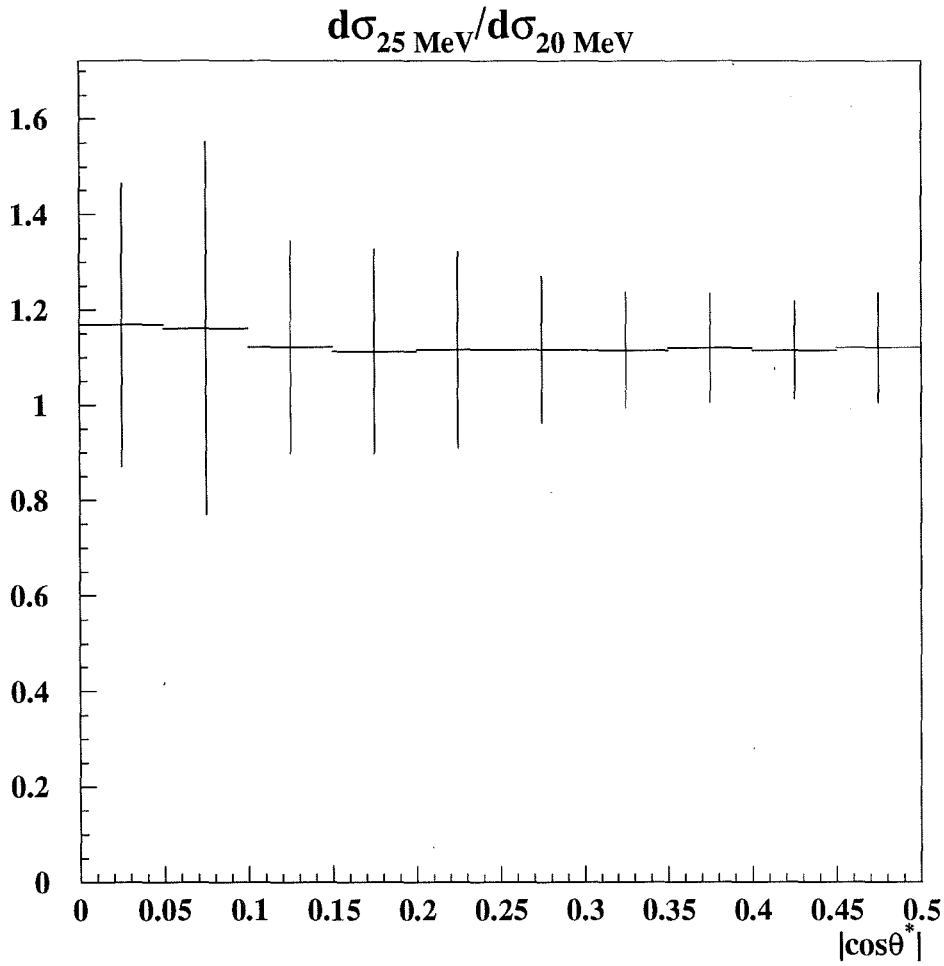

Figure 5.2: This is a histogram of the ratio of the $\gamma\gamma$ background determination at 2975 MeV for CCAL cluster energy thresholds of 25 MeV and 20 MeV. The differential cross section for the 25 MeV threshold is larger in every $|\cos(\vartheta^*)|$ bin. The weighted average of the ordinates is 1.12.

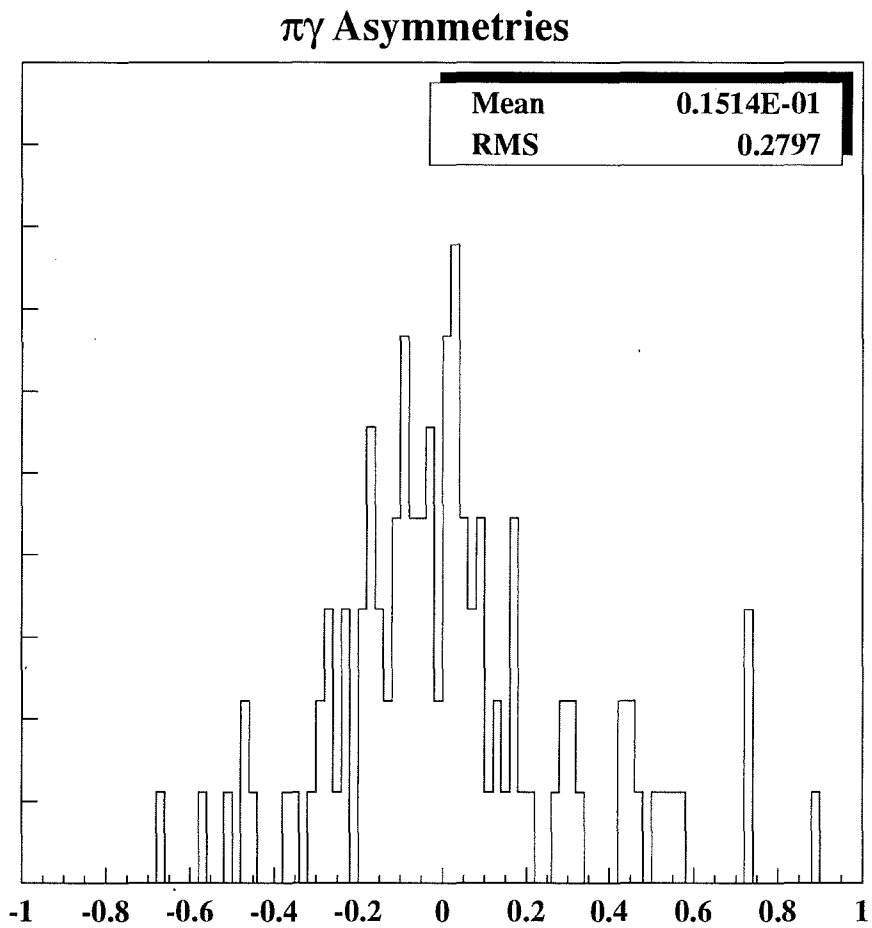

Figure 5.3: This is a histogram of the $\pi^0\gamma$ asymmetry, $[(-)-(+)]/[(-)+(+)]$. Each of the 110 entries is one of the 10 asymmetry values determined from the differential $\pi^0\gamma$ cross sections at each of the 11 energies used in the η_c analysis.

analysis. Each cosine bin at each energy contributes a normal distribution with mean the absolute value of the asymmetry and width the error on the value of the asymmetry. The area of each distribution is inversely proportional to the error assigned each asymmetry. Such an ideogram estimated this systematic error with the mean being related to a weighted average. The mean of the ideogram can be taken to represent an $\sim 15\%$ systematic error in the determination of the $\pi^0\gamma$ differential cross section. The $\pi^0\gamma$ differential cross section contributes more than 60% of the $\gamma\gamma$ background. A conservative estimate is made by taking this systematic error to represent an additional fractional error independent of the statistical error in the $\gamma\gamma$ background estimate in each $|\cos(\vartheta^*)|$ bin at each energy.

5.4.3 Development of The Error Matrix

As indicated in the previous section, the systematic errors can be classified as acting coherently or incoherently on the differential background cross sections. The final form of the error matrix used to determine the systematic contribution of the background model to the total error on the estimated signal treats the systematic threshold error as a coherent error. The residual statistical error and the asymmetry error are treated as incoherent errors.

Incoherent errors are introduced into the error matrix of the background parameters by treating the uncertainties in each $|\cos(\vartheta^*)|$ bin as random, and performing a fit in the usual manner. Following the results from the previous sections, the error determined from the asymmetry of the $\pi^0\gamma$ differential cross sections is added in quadrature to the statistical error carried through from the measurements of the $\pi^0\gamma$ and $\pi^0\pi^0$ differential cross sections for each $|\cos(\vartheta^*)|$ bin. The resulting error matrix from the fit then includes both systematic errors.

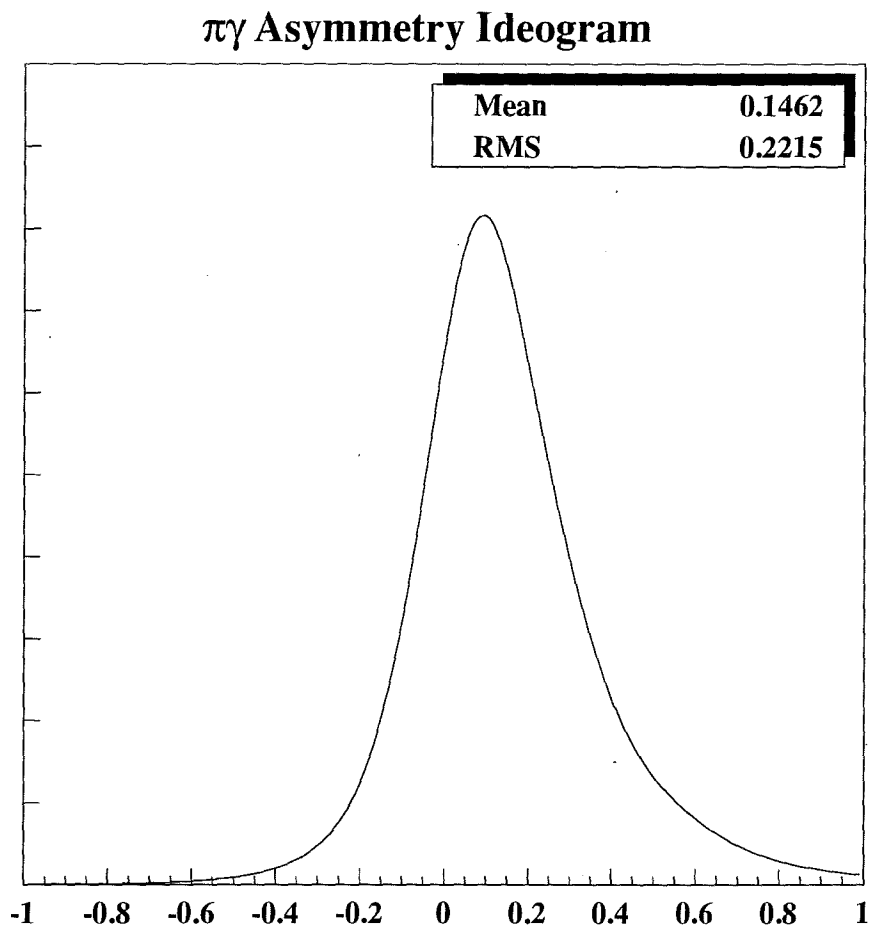

Figure 5.4: The mean of this ideogram corresponds to a weighted average with weights inversely proportional to the error. The peak position of the ideogram is less than the mean.

The systematic error due to the choice of CCAL cluster energy threshold acts coherently on the differential background cross sections. Each $|\cos(\vartheta^*)|$ bin is increased by the same percentage for a change in the CCAL cluster energy threshold. In the case of this coherent error, the percentage change in the background parameterization can be written as,

$$\begin{aligned} p(x) &\rightarrow (1+\alpha)p(x) \\ &= (p_1+\alpha p_1)+(p_2+\alpha p_2)x^2+(p_3+\alpha p_3)x^4+(p_4+\alpha p_4)x^6 \end{aligned}$$

with α being a real number in the interval (-1,1). The contribution to the error on each parameter from this coherent error is αp_i. If V_{ij} originally represents the error matrix based on only incoherent errors, the extra contribution from coherent errors is,

$$V_{ij} \rightarrow V_{ij} + \alpha^2 p_i p_j .$$

5.5 Results for Fiducial Limits

The signal cross section in Equation 5.16 is taken to be the η_c resonance represented by a Breit-Wigner resonance formula,

$$g = \frac{d\sigma_{\mathrm{BW}}}{dx} = \left(\frac{\pi}{4k^2}\right)\frac{B_{\mathrm{in}}B_{\mathrm{out}}\Gamma^2}{(\sqrt{s}-M)^2+(\Gamma/2)^2},$$

at each energy. To use Equation 5.26, the expected signal must be calculated regardless of E760 results for the η_c resonance. The η_c resonance parameters in Table 5.2 are taken from the 1992 Review of Particle Properties.

Figure 5.5 is a typical plot of Equation 5.26. The two terms on the right hand side of Equation 5.26 are plotted along with the sum. The value of $x = |\cos(\vartheta^*)|$ at which $(\Delta\sigma^*)^2_{\mathrm{total}}$ is a minimum is the desired fiducial limit, x_c. This

η_c Resonance Parameters

Mass (GeV/c^2)	Γ (GeV)	$B_{in}B_{out}$
2.9788	10.3×10^{-3}	6.8×10^{-7}

Table 5.2: The Particle Data Group best world averages for the η_c resonance parameters.

represents the limit at which improvements in the statistical accuracy of the measurement begin to be dominated by the accumulation of uncertainty in the background estimation. The values of x_c at each energy are in Table 5.3.

The effect on x_c of increasing or decreasing the signal cross section is also tabulated in Table 5.3. As expected, the largest effect is found at the energies near 2.9788 GeV/c^2. At the peak of the resonance, as defined in Table 5.2, a change in the signal cross section by a factor of 2 has at most a 6% effect on the value of x_c.

Probably the most interesting property of the results is the relationship of integrated luminosity and the x_c value. The energies with the larger integrated luminosities have smaller $\cos(\vartheta^*)$ cutoff values. This is a consequence of the increased statistical significance of the data.

5.6 Likelihood Function

For E760, the unnormalized event probability for $\gamma\gamma$ events at the jth energy,

$$F_j(x;\vec{a}) = \epsilon_j L_j \left(g_j(x;\vec{a}) + b_j(x)\right) ,$$

is written as a function of $x \equiv |\cos(\vartheta^*)|$. The factor $\epsilon_j L_j$ is the effective luminosity at the jth energy. g_j and b_j represent the signal and the background differential cross sections at the jth energy respectively.

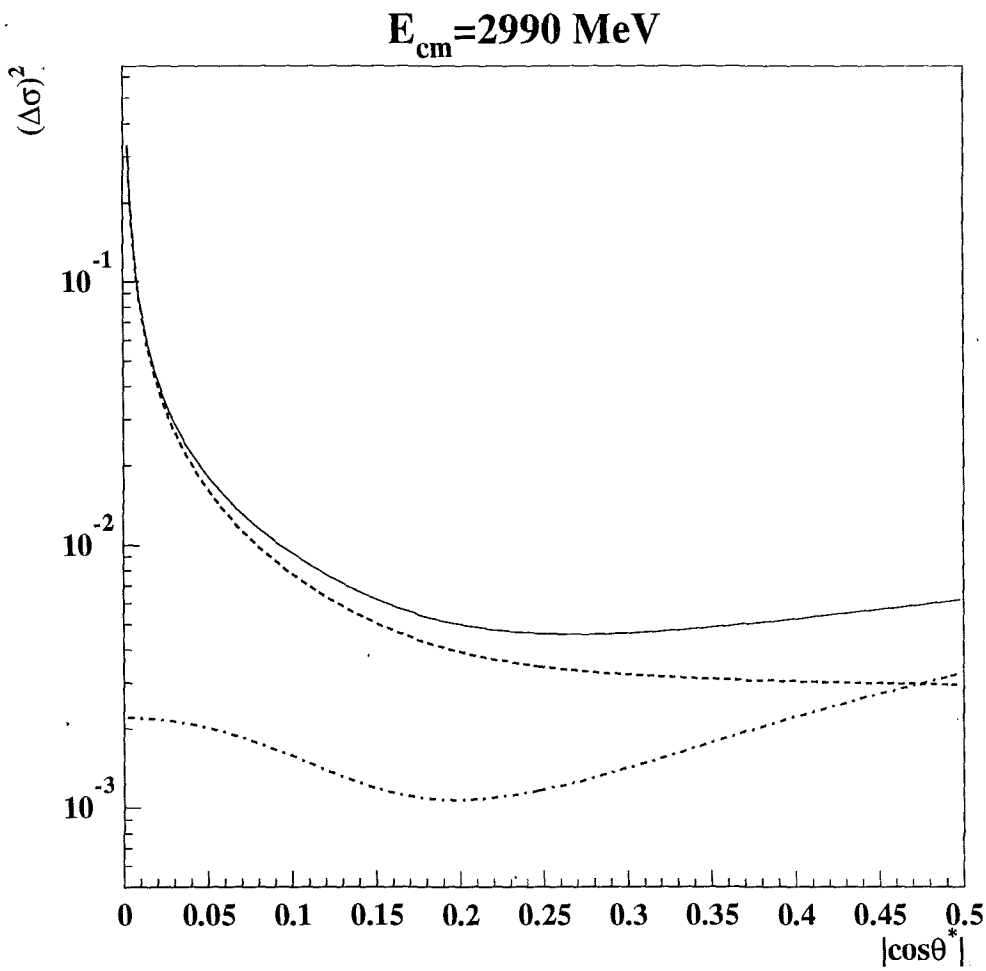

Figure 5.5: A typical plot of Equation 5.26 along with the two terms contributing to the sum. The dashed line is $(\Delta\sigma^*)^2_{\rm stat}$, the dot-dash line is $(\Delta\sigma^*)^2_{\rm bkg}$.

A Priori $\cos(\vartheta^*)$ Cutoff

L $(\mathrm{nb})^{-1}$	E_{cm} (GeV)	$x_c(\sigma)$	$x_c(0.50\sigma)$	$x_c(2\sigma)$
49.35	2.9113	0.31	0.31	0.31
197.85	2.9501	0.27	0.27	0.27
423.49	2.9749	0.28	0.26	0.29
163.48	2.9792	0.33	0.31	0.35
393.43	2.9812	0.28	0.27	0.30
201.15	2.9855	0.31	0.31	0.33
512.50	2.9896	0.25	0.25	0.26
310.13	2.9940	0.27	0.27	0.28
177.92	3.0050	0.32	0.32	0.32
119.86	3.0497	0.33	0.33	0.33
690.92	3.0975	0.27	0.27	0.27

Table 5.3: The $\cos(\vartheta^*)$ cutoff value and the cutoff value at 50% and 200% of the expected signal are given for all 11 energies used in the η_c analysis.

The background differential cross section is described by a polynomial at each energy.

$$\begin{aligned} b_j(x) &= \frac{d\sigma_{\mathrm{BKG},j}}{dx} \\ &= p_{1,j} + p_{2,j}x^2 + p_{3,j}x^4 + p_{4,j}x^6 \end{aligned}$$

The signal differential cross section at each energy, g_j, is described by contributions from a Breit-Wigner resonance and a $\gamma\gamma$ continuum.

$$g_j(x) = \left(\frac{d\sigma_{\mathrm{BW},j}}{dx} + \frac{d\sigma_{\gamma\gamma,j}}{dx}\right)$$

$$\frac{d\sigma_{\mathrm{BW},j}}{dx} = \left(\frac{\pi}{4k^2}\right) \frac{B(\eta_c \to \bar{p}p)(\Gamma^2_{\gamma\gamma}/B(\eta_c \to \gamma\gamma))}{(\sqrt{s_j} - M)^2 + (\Gamma_{\gamma\gamma}/2B(\eta_c \to \gamma\gamma))^2} \tag{5.27}$$

$$\frac{d\sigma_{\gamma\gamma,j}}{dx} = A\left(\frac{s_0}{s_j}\right)^5 \tag{5.28}$$

Dimensional counting rules [27, 28] for the power law behavior of exclusive processes inspired the functional form for the $\gamma\gamma$ continuum cross section. A flat differential

cross section is justified by the low statistics and an apparent lack of significant structure [33, 64] for the E760 fiducial volume. The parameter s_0 =3097 MeV is the scale of this experiment.

The expected number of events at each energy is,

$$\begin{aligned} \overline{n}_j &= \epsilon_j L_j \int_0^{x_{c,j}} dx\, F_j(x;\vec{a}) \\ &= \epsilon_j L_j \int_0^{x_{c,j}} dx\, \left(g_j(x;\vec{a}) + b_j(x)\right) \ . \end{aligned}$$

The joint extended maximum likelihood for all the events is,

$$\mathcal{L} = \prod_{j=1}^{11} e^{-\bar{n}_j} \prod_{i=1}^{\mathrm{N}_j} F_j(x_i;\vec{a}) \ .$$

This likelihood is optimized to find the best values for the signal parameters $\vec{a}$ (=$B(\eta_c \to \gamma\gamma)$, $\Gamma_{\gamma\gamma}$, M, and A). The total number of events measured at each energy is N_j.

5.6.1 η_c Resonance and $\gamma\gamma$ Continuum

In this analysis, a $\gamma\gamma$ cross section constant with respect to $x = |\cos(\vartheta^*)|$ is used in the model of the total cross section. As shown in [65], the slope of the differential cross section for $\gamma\gamma \to \bar{p}p$ is small for $x_c \leq 0.35$. Table 5.4 has the results for a nonnegative $\gamma\gamma$ continuum.

Table 5.5 contains the result of the likelihood analysis with the parameter A free to take on any real value. In this case, the best fit parameters give a nonphysical result for the $\gamma\gamma$ continuum.

There are nonzero correlations between the fit parameters. The parameter $B_{\eta_c\to\gamma\gamma}$ is correlated to the parameter $\Gamma_{\gamma\gamma}$ with a coefficient -0.088 in fit I and 0.106

η_c Resonance Parameters and $\gamma\gamma$ Continuum, I

Mass (MeV/c^2)	$\Gamma_{\gamma\gamma}$(KeV)	$B(\eta_c \to \gamma\gamma) \times 10^4$	A(pb)
$2988.1^{+3.1}_{-2.6}$	$6.9^{+2.3}_{-1.6}$	$3.03^{+0.65}_{-0.56}$	0^{+10}

Table 5.4: The η_c resonance and a $\gamma\gamma$ continuum which is a nonnegative constant differential cross section with a $(1/s)^5$ energy dependence are used to model the data. The errors are statistical errors only.

in fit II. The η_c mass and partial width have correlation coefficients 0.253 and 0.245 in fits I and II respectively. In fit II, the parameters $B_{\eta_c \to \gamma\gamma}$, $\Gamma_{\gamma\gamma}$, and M are correlated with A with coefficients -0.399, -0.651, and -0.031 respectively.

5.6.2 η_c Resonance

As shown in the previous section, a nonzero $\gamma\gamma$ continuum is inconsistent with the data sample and the background determination. Table 5.8 contains the best fit parameters when the $\gamma\gamma$ continuum is set to zero in the likelihood function.

The parameter $B(\eta_c \to \gamma\gamma)$ is negatively correlated to the parameter $\Gamma_{\gamma\gamma}$ ($\rho = -0.088$). Figures 5.6, 5.8, and 5.7 show the likelihood contours when there is no $\gamma\gamma$ continuum cross section ($A = 0$) in the model.

The s dependence of the background cross section is not determined by this likelihood analysis. Therefore, the η_c resonance shape is drawn on the histogram of

η_c Resonance Parameters and $\gamma\gamma$ Continuum, II

Mass (MeV/c^2)	$\Gamma_{\gamma\gamma}$ (KeV)	$B(\eta_c \to \gamma\gamma) \times 10^4$	A(pb)
$2988.1^{+3.2}_{-2.6}$	$9.8^{+4.8}_{-2.8}$	$3.51^{+0.66}_{-0.62}$	-41^{+26}_{-24}

Table 5.5: The η_c resonance and a $\gamma\gamma$ continuum term which is an unrestricted constant with a $(1/s)^5$ energy dependence are used to model the data. The errors are statistical errors only.

Correlation Matrix, I

	Mass	$\Gamma_{\gamma\gamma}$	$B(\eta_c \to \gamma\gamma) \times 10^4$	A
Mass	1	0.253	-0.007	0.001
$\Gamma_{\gamma\gamma}$	0.253	1	-0.088	-0.008
$B(\eta_c \to \gamma\gamma) \times 10^4$	-0.007	-0.088	1	-0.006
A	0.001	-0.008	-0.006	1

Table 5.6: The correlation coefficients for the fit parameters presented in Table 5.4.

Correlation Matrix, II

	Mass	$\Gamma_{\gamma\gamma}$	$B(\eta_c \to \gamma\gamma) \times 10^4$	A
Mass	1	0.245	0.018	-0.031
$\Gamma_{\gamma\gamma}$	0.245	1	0.106	-0.651
$B(\eta_c \to \gamma\gamma) \times 10^4$	0.018	0.106	1	-0.399
A	-0.031	-0.651	-0.399	1

Table 5.7: The correlation coefficients for the fit parameters presented in Table 5.5.

η_c Resonance Parameters

Mass (MeV/c^2)	$\Gamma_{\gamma\gamma}$ (KeV)	$B(\eta_c \to \gamma\gamma) \times 10^4$	A(pb)
$2988.1^{+3.1}_{-2.6}$	$6.9^{+2.3}_{-1.6}$	$3.03^{+0.65}_{-0.56}$	0 (fixed)

Table 5.8: The η_c resonance is used to model the data.

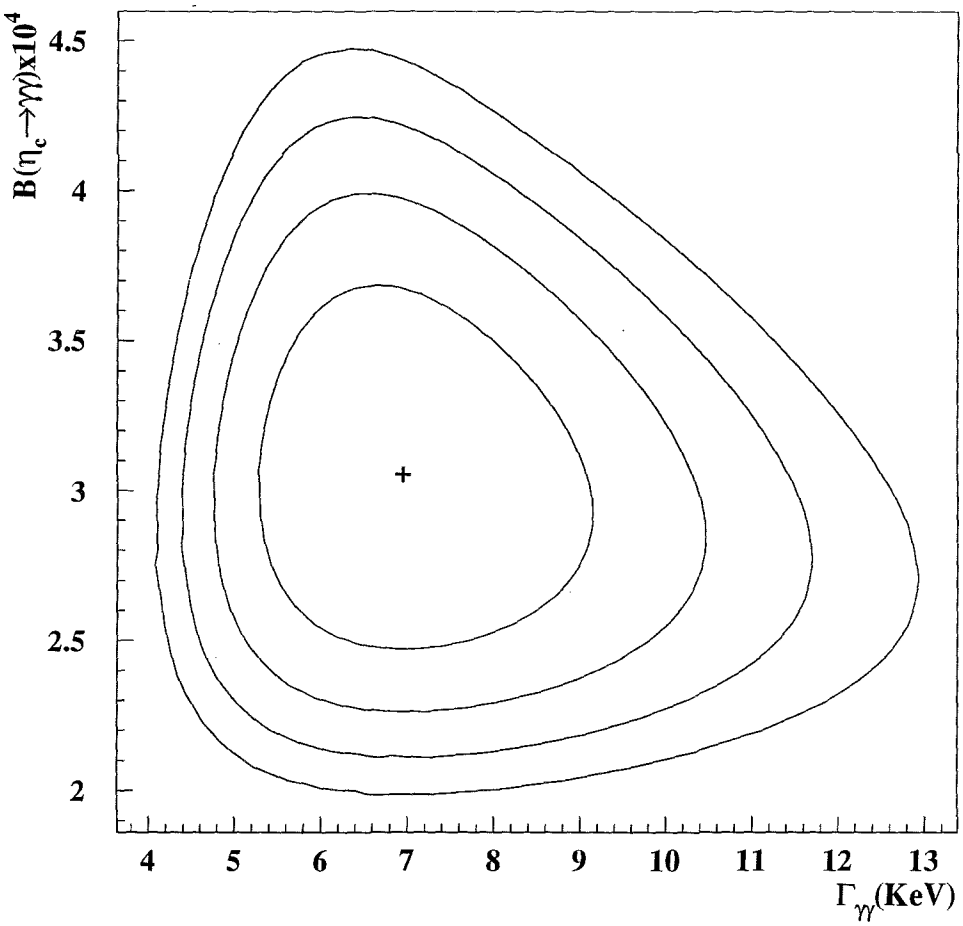

Figure 5.6: The extremes of the projection onto each axis of the contours represent the 1, 2, 3, and 4 standard deviations of the variable. The correlation coefficient is -0.088.

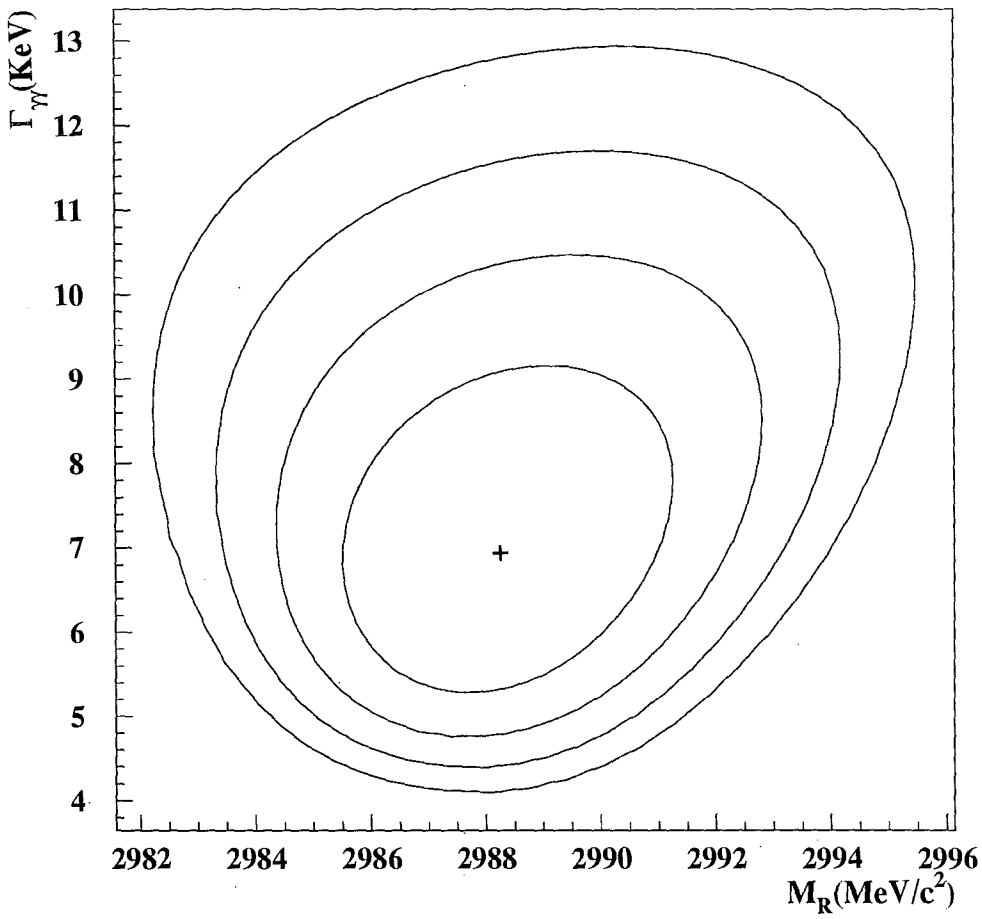

Figure 5.7: The extremes of the projection onto each axis of the contours represent the 1, 2, 3, and 4 standard deviations of the variable. The correlation coefficient is 0.254.

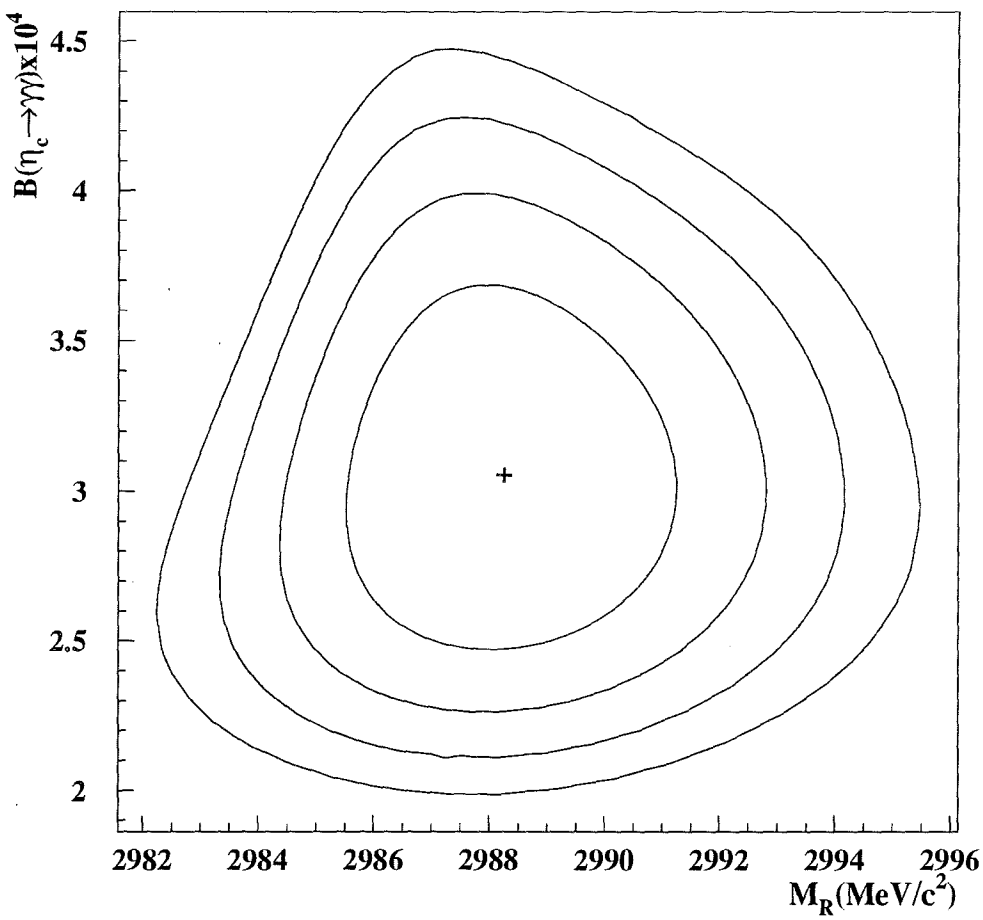

Figure 5.8: The extremes of the projection onto each axis of the contours represent the 1, 2, 3, and 4 standard deviations of the variable. The correlation coefficient is -0.007.

the background subtracted total cross section at each of the 11 energies in Figure 5.9.

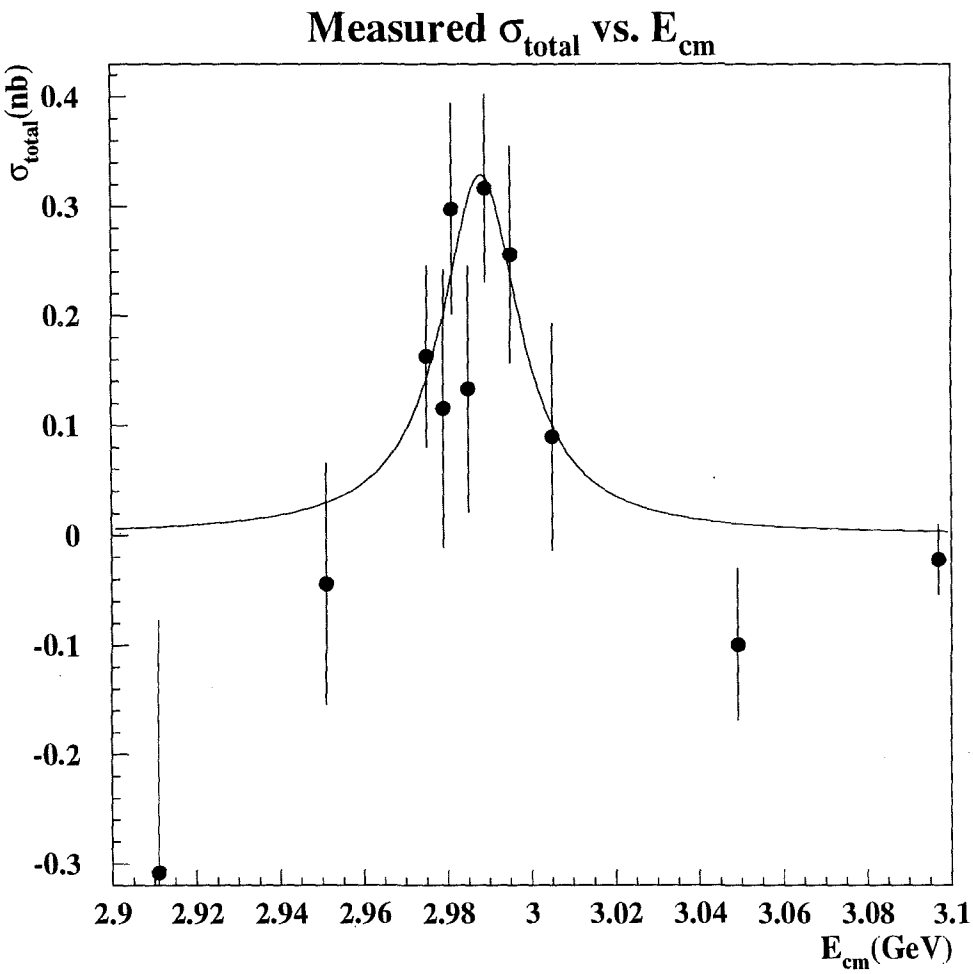

Figure 5.9: The points show the background subtracted total cross section at each energy. For energies 2911, 2950, 3050, and 3097 MeV, the background subtracted cross sections are negative. The curve represents the best fit values for the η_c resonance parameters and the $\gamma\gamma$ continuum set to zero.

5.6.3 Goodness-of-Fit

The Kolmogorov-Smirnov (K-S) test is applicable to unbinned distributions and is useful here to evaluate the goodness of the fit at each energy. The 11

independent K-S probabilities, α_j, can be combined using

$$\alpha' = -2 \ln \prod_{j=1}^{11} \alpha_j$$

to give a statistic which is distributed as a $\chi^2(22)$,[66]. The α_j and α' for a model with no $\gamma\gamma$ continuum cross section ($A = 0$) are found in Table 5.9. Converting α' to the appropriate χ^2 probability gives a confidence level of 19%.

K-S Test

$\sqrt{s}$	K-S statistic	K-S probability
2911	0.324	0.579
2950	0.202	0.567
2974	0.110	0.707
2979	0.217	0.293
2981	0.173	0.114
2985	0.173	0.547
2989	0.252	0.004
2994	0.171	0.353
3005	0.247	0.316
3050	0.339	0.793
3097	0.162	0.819

Table 5.9: For these 11 independent probabilities, α' is 27.47. The confidence level based on a χ^2 distribution with 22 degrees of freedom ($\chi^2/n = 1.25$) is $\approx 19\%$.

Chapter 6

Charged Event Selection and Likelihood Analysis

During the 1991 Fermilab fixed target run, E760 accumulated $\approx$30 pb^{-1} of data. The majority of the available luminosity was used for a resonance scan of the η_c and searches for the η_c' and h_c resonances. Since the E760 detector and trigger are designed to search for high mass electromagnetic showers, the data sample always contains the exclusive e^+e^- channel.

6.1 The Data

The data analysed are from the first physics trigger, GM4. All events passing the hardware trigger were written to tape. The devices used to trigger the experiment are the H1 and H2 hodoscopes, the Čerenkov detector, the calorimeters (CCAL and FCAL), and the forward charge veto counters. The trigger level logic for the first physics trigger is the logical OR of the following triggers written in terms of detector level logic.

2Č: $(\mathrm{PBG1})\otimes\#\mathrm{H1} \leq 4 \otimes \#\mathrm{H2} \leq 4 \otimes (\mathrm{h^+h^-}) \otimes (\mathrm{e^+e^-})$

1Č: $(\mathrm{PBG1})\otimes\#\mathrm{H1} \leq 2 \otimes \#\mathrm{H2} = 2 \otimes (\mathrm{h^+h^-}) \otimes (\mathrm{e^+})\otimes(\mathrm{COPL})$

0Č: $\#H1 \leq 2 \otimes \#H2 = 2 \otimes (\overline{FCHOR}) \otimes (h^+h^-) \otimes (COPL)$

Data summary tapes (DSTs) of these data were made based on the summary data appended by the ACP analysis program [54]. The filtering for these DSTs required the logical sum of the following criteria.

- An invariant mass between any two CCAL clusters greater than 2.0 GeV.
- The relative ϕ and ϑ of the two highest energy clusters satisfy two body kinematics for $\gamma\gamma$, $\bar{p}p$, or $\pi^+\pi^-$ final states.

The integrated luminosity and the beam energies for the data sample are summarized in Table 6.1.

$\bar{p}p \rightarrow e^+e^-$ Data Sample

s (GeV^2)	8.82 ± 1.37	12.43 ± 0.20	12.85 ± 1.51
L (pb^{-1})	2.886 ± 0.09	16.1 ± 0.45	6.089 ± 0.17

Table 6.1: The integrated luminosity, L, and the value of s at which the data were taken. The given errors in L are the combined systematic errors from the total elastic cross section measurements and the solid angle of the detector. The statistical errors are an order of magnitude less. The errors in s are the rms deviations.

6.2 Selecting Events

Previous analyses of these data [67] for the exclusive e^+e^- channel have relied greatly on the inner charged detectors for E760. The offline selection presented here is based primarily on the electromagnetic response of the CCAL. The beam energy is measured precisely and the errors made in the CCAL measurement of the energy and angles of an electromagnetic shower are known well enough to justify a kinematic fit.

The e^+e^- events for each energy point are counted. In the final sample

- CCAL Requirements

  1) there are only 2 clusters in the CCAL with energy greater than 100 MeV and labeled as ontime,
  2) the cluster masses of the two highest energy clusters are each consistent with a single photon, $20 \leq M_{cl} \leq 95$ MeV/c^2,

- Background Rejection

  3) there are no clusters found in the FCAL,
  4) the charged tracking at the trigger level corresponds to the two highest energy clusters,
  5) there are no combinations of the highest energy clusters with low energy clusters that have invariant masses consistent with the mass of the π^0, 80 MeV/c^2 $\leq M_{1\vee 2,j} \leq$ 170 MeV/c^2,

- Kinematical Consistency

  6) all events fit to the twobody hypothesis with χ^2 fit probability at least 0.10.

Selection criterion #4 differs from the neutral event selection previously described in §4.2. The e^+e^- events are required to correspond to the charged tracking at the trigger level as represented by the trigger logic presented in the previous section. As shown in Figure 3.1, the coincidence between the H1 and H2 hodoscopes is required for the two highest energy CCAL clusters. Coincidence in the Čerenkov detector is required for at least one of the CCAL clusters representing the e^+e^- event.

The study of the selection efficiency less criterion #4, charged trigger - CCAL correspondence, is identical to that found in §4.3.1. From a sample of 4583 J/ψ events, 3315 events pass the selection criteria for e^+e^- events. The selection efficiency is 0.723 ± 0.007. Since Criterion #4 requires that the trigger be associated with the event as defined in the CCAL, the efficiency for criterion #4 enters the total efficiency through the calculation of the h^+h^- and e^- detector level logic. The final number of events at each energy is in Table 6.2.

Selected e^+e^- events

s (GeV^2)	x_c	# events
8.82	0.45	13
12.43	0.60	16
12.85	0.61	8

Table 6.2: The number of events at each energy point with $|\cos(\vartheta^*)| < x_c$ for the exclusive e^+e^- final state. The limit on $|\cos(\vartheta^*)|$ at each energy represents the active volume of the Čerenkov detector.

6.3 Detection Efficiencies

The first physics trigger was designed to select high mass e^+e^- final states. Detection efficiencies of several detectors, in addition to hardware logic efficiencies, are needed for the calculation of the total trigger efficiency. Each of the subtrigger efficiencies is calculated with the following formulas according to the logic vectors given in §6.1.

$$\epsilon_{2\check{C}} = \epsilon_{\mathrm{PBG}} * \epsilon_{\#\mathrm{H1}\leq 4 \otimes \#\mathrm{H2}\leq 4} * \epsilon_{hh} * \epsilon_{ee}$$

$$\epsilon_{1\check{C}} = \epsilon_{\mathrm{PBG}} * \epsilon_{\#\mathrm{H1}\leq 2 \otimes \#\mathrm{H2}=2} * \epsilon_{hh} * \epsilon_{e} * \epsilon_{\mathrm{COPL}}$$

$$\epsilon_{0\check{C}} = \epsilon_{\#H1\leq 2 \otimes \#H2=2} * \epsilon_{\overline{FCAL}} * \epsilon_{hh} * \epsilon_{COPL}$$

The remainder of this section is a discussion of the different detector level efficiencies that will be used to calculate the subtrigger efficiencies, $\epsilon_{2\check{C}}$, $\epsilon_{1\check{C}}$, and $\epsilon_{0\check{C}}$.

6.3.1 H2 Detection Efficiency

The hodoscope H1 has an eight-fold azimuthal symmetry and the hodoscope H2 has a thirty-two-fold azimuthal symmetry. The cracks between elements in H1 and H2 were aligned when installed. A previous study [68] has determined that H2 is rotated $\approx 1.18 \pm 0.003$ mrad with respect to H1. Detection inefficiencies occur for particles passing close to the edges of the elements of H1 and H2.

An unbiased sample of charged tracks is needed to study these detection inefficiencies. Since the 2 Čerenkov subtrigger allows for charged track multiplicities greater than two, there are events in the first physics trigger with charged tracks that did not cause the trigger. Isolated charged tracks of this sort are not biased due to the trigger. The selection of these unbiased isolated charged tracks uses the straw tubes and the RPC/MWPC. The criteria are:

- no associated signal from the Čerenkov detector, i.e. choose only those tracks that do not form the trigger,
- an associated straw tube signal,
- no adjacent H2 elements, i.e. isolated charged track,
- fiducial volume, $15° \leq \theta_{\text{lab}} \leq 60°$,
- linear fit probabilities in the $x - y$ and ρ-z planes greater than 0.1,
- and impact parameters, b_{xy} and $b_{\rho z}$, chosen to be consistent with tracks originating within the interaction region.

- For $E_{\text{cm}} = 2.9$ GeV, $|b_{xy} + 0.24| < 0.43$, $|b_{\rho z} - 0.19| < 0.07$
- For $E_{\text{cm}} = 3.1$ GeV, $|b_{xy} + 0.36| < 0.38$, $|b_{\rho z} - 0.25| < 0.07$
- For $E_{\text{cm}} = 3.5$ GeV, $|b_{xy} + 0.29| < 0.58$, $|b_{\rho z} - 0.25| < 0.06$
- For $E_{\text{cm}} = 3.6$ GeV, $|b_{xy} + 0.20| < 0.54$, $|b_{\rho z} - 0.21| < 0.09$

The requirements on the χ^2 fit probability of the measurements from the charged particle detectors to a straight line in the x-y and ρ-z planes and no adjacent H2 elements are designed to select unambiguous charged tracks. Charged tracks originating in the interaction region are selected by the impact parameter criteria. The impact parameter is the minimum distance of the surveyed vertex from the best fit line to the detector measurements in the plane. Because the surveyed vertex is not necessarily the actual vertex, offsets are applied before a cut on the distribution is made. A 1.41σ cut on the distributions of the impact parameters at each energy gives a statistically significant sample while assuring that the charged track originates in the interaction region.

The calculation of where the charged track passed through the H2 elements assumes that $\phi = 0$ occurs at the edge of an H2 element. Each H2 element subtends ≈ 196 mrad of arc. The variable,

$$x = \frac{\phi - 0.196(\text{H2 element \# - 1})}{0.196}$$

is between 0 and 1 for each charged track. A second order polynomial, $y(x) = a_0 + a_1 x + a_2 x^2$, is fit to the histogram of x at each energy point. The detection efficiency, ϵ_h, for a single charged track is calculated as in Equation 6.1.

$$\epsilon_h = \frac{\int_0^1 y(x)\,dx}{\int_0^1 y_{\text{max}}\,dx} \tag{6.1}$$

The results for different $E_{\rm cm}$ are presented in Table 6.3. Each subtrigger demands two charged tracks which is equivalent to demanding two elements of H2. Therefore the efficiency of the (h^+h^-) logic, ϵ_{hh}, is the square of ϵ_h.

Arm Topology Efficiencies

$E_{\rm cm}$ GeV	a_0	a_1	a_2	ϵ_h	ϵ_{hh}
2.9	621.8	218.3	-212.5	0.97 ± 0.006	0.95 ± 0.012
3.1	534.2	78.53	-102.3	0.98 ± 0.006	0.96 ± 0.011
3.5	1937	139.6	-35.21	0.96 ± 0.004	0.92 ± 0.008
3.6	1524	733.8	-651.4	0.97 ± 0.004	0.94 ± 0.008

Table 6.3: Results of fit to $2^{\rm nd}$ order polynomial. The efficiencies for single and double arm topologies are in last two columns.

6.3.2 Čerenkov Detection Efficiency

Although no information from the Čerenkov detector is used in the offline selection of events, this detector is used in the hardware selection of events as is apparent from its role in the charged trigger. There exists approximately 1 pb^{-1} of data taken at the J/ψ mass that incorporates all three of the charged triggers listed at the beginning of this chapter. The different requirements of the hodoscopes for each trigger can be made equivalent using the pattern unit data in the offline. Therefore, with a clean sample of J/ψs selected without recourse to the Čerenkov detector data, we are able to determine the inefficiency incurred by the 1 and 2 electron requirements. This sample of 2575 clean J/ψs has only two ontime clusters in the central calorimeter and a fit probability of at least 0.10. There is a discrepancy between the trigger logic and the pattern unit data, but the error is small ($\approx 0.039\%$).

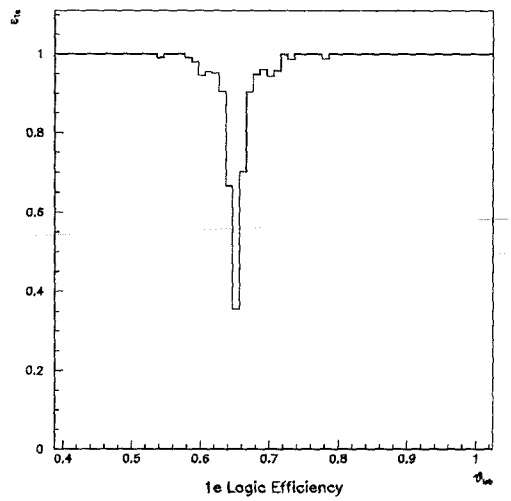

Figure 6.1: The one electron detection efficiency as a function of θ_{lab}.

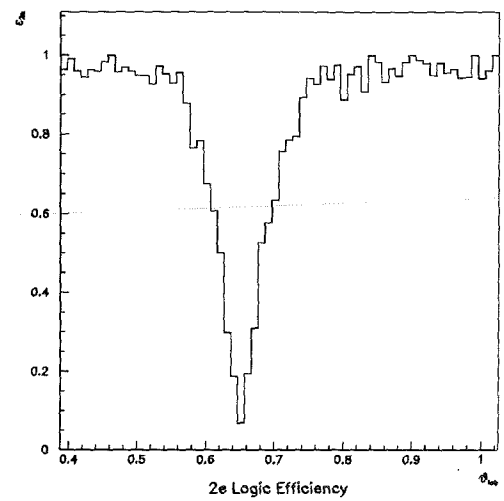

Figure 6.2: The two electron detection efficiency as a function of θ_{lab}.

From the clean sample of J/ψs, the one and two electron detection efficiencies as a function of θ_{lab} can be determined (Figures 6.1 and 6.2). The inefficiency in the middle of the fiducial volume of the detector can be explained by the septum separating the two gases of the Čerenkov detector. Since this effect is geometrical, we can expect the effect to depend on the velocity of the center of momentum in the laboratory. Using the information in Figures 6.1 and 6.2 and an event generator with a flat angular distribution, the one and two electron detection efficiencies are found at E_{cm} different from the J/ψ mass. The total efficiencies determined with the data and simulated events are presented in Table 6.4.

Čerenkov Detection Efficiencies

	Data	Simulation			
$E_{\text{cm}}(GeV)$	3.09	2.989	3.09	3.525	3.61
$\epsilon_e(\%)$	97.3 ± 0.2	99.4 ± 0.04	97.8 ± 0.08	100	100
$\epsilon_{ee}(\%)$	85.0 ± 0.5	77.2 ± 0.2	82.7 ± 0.2	74.0 ± 0.24	74.4 ± 0.2

Table 6.4: Čerenkov efficiency at different E_{cm}

6.3.3 Hodoscope Multiplicities

Requirements on the hodoscope multiplicities are a source of inefficiencies in the trigger. Additional hodoscope elements will be present in an event for several reasons.

- pileup signals for H1 and H2
- δ rays from the interaction of the antiproton beam and the atomic electrons which enter H1
- δ rays from the interaction of a final state electron with the matter before H2

By considering the different triggers, efficiencies of the hodoscope multiplicity requirements can be estimated without regard to the specific processes involved. Also, the sources of extra elements in the two hodoscopes are independent.

The efficiency for the requirement $\#\mathrm{H1} \leq 2 \otimes \#\mathrm{H2} = 2$ can be obtained by simply counting the number of events in the (2Č) trigger that satisfy this requirement. This efficiency is calculated at both the J/ψ and ψ' resonances using the exclusive decay into e^+e^-. The result for the clean sample of J/ψs is $\epsilon_{\#\mathrm{H1}\leq 2\otimes\#\mathrm{H2}=2} = 0.8742 \pm 0.0065$. The result [69] for 163 exclusive decays of the ψ' is $\epsilon_{\#\mathrm{H1}\leq 2\otimes\#\mathrm{H2}=2} = 0.761 \pm 0.033$. The difference in the two results for this efficiency are due to the differences in the interaction rates. The η_c data were taken with interaction rates similar to those for the J/ψ data. The ψ' data represent the same interaction rates used for the η_c' and h_c data.

An estimate of the efficiency for the $\#\mathrm{H1} \leq 4 \otimes \#\mathrm{H2} \leq 4$ requirement takes two steps. First, the probability of having at least one extra hit in either hodoscope is estimated. This is done by counting the number of (2Č) events that have three or more hits in H1 and the number that have three or more hits in H2. At least three

extra hits in either H1 or H2 are needed for a signal event to be rejected by the $\#\mathrm{H1} \leq 4 \otimes \#\mathrm{H2} \leq 4$ requirement. Second, the probability of having at least three extra hits in a hodoscope is estimated to be the cube of the probability for having at least one extra hit in the hodoscope. Therefore, the probability of a signal event being rejected is the sum of the probabilities for at least three extra hits in a hodoscope. The efficiency of the $(\#\mathrm{H1} \leq 4 \otimes \#\mathrm{H2} \leq 4)$ requirement is the conjugate probability. The final result for the $(\#\mathrm{H1} \leq 4 \otimes \#\mathrm{H2} \leq 4)$ requirement, 0.9992 ± 0.0006, is the same for the clean J/ψ and exclusive ψ' samples.

The results for the trigger efficiencies at the detector level are presented in Table 6.5. Each separate subtrigger is calculated as the product of the appropriate detector level efficiencies.

Detector Level Logic

E_{cm} GeV	ϵ_{hh}	ϵ_{e}	ϵ_{ee}	$\epsilon_{\#\mathrm{H1}\leq 2\otimes\#\mathrm{H2}=2}$
2.9	0.95 ± 0.012	0.994 ± 0.0004	0.77 ± 0.002	0.87 ± 0.01
3.5	0.92 ± 0.01	1	0.74 ± 0.002	0.76 ± 0.03
3.6	0.94 ± 0.01	1	0.74 ± 0.002	0.76 ± 0.03

$\epsilon_{\#\mathrm{H1}\leq 4\otimes\#\mathrm{H2}\leq 4}$	ϵ_{PBG}
0.9992 ± 0.0006	0.995 ± 0.0014

Table 6.5: Detector level logic efficiencies for each E_{cm} of interest.

6.3.4 PBG and Coplanarity Efficiencies

An additional trigger was added to the data from which the clean sample of J/ψs are taken. This two coplanar electron (2ce) trigger,

$$(2\mathrm{ce}) : \#\mathrm{H1} \leq 4 \otimes \#\mathrm{H2} \leq 4 \otimes (\mathrm{h^+h^-}) \otimes (\mathrm{e^+e^-}) \otimes (\mathrm{COPL}),$$

was implemented to study the PBG logic efficiency. By comparing this trigger with the (2Č) trigger with the hodoscope requirements made equivalent, 13 events are

found that satisfy the (2ce) trigger. Upon examination, these events can be categorized as missed events. This indicates that the efficiency of the PBG logic is 0.995 ± 0.0014. Comparison of the (0Č) and (2Č) triggers indicates that the coplanarity logic is completely efficient.

6.4 Trigger Efficiency

The detector level logic efficiencies are combined to form the charged trigger efficiencies. The total efficiency for each subtrigger at each center of momentum energy is in Table 6.6. The total trigger efficiency for the two body charged final state is calculated from the hardware level logic efficiencies as indicated in Equation 6.2.

$$\epsilon_{\text{trigger}} = \epsilon_{2\check{C}} + \epsilon_{1\check{C}} - \epsilon_{1\check{C}} * \epsilon_{2\check{C}} \tag{6.2}$$

Trigger Level Logic

E_{cm}(GeV)	$\epsilon_{1\check{C}}$	$\epsilon_{2\check{C}}$	$\epsilon_{\text{trigger}}$
2.9	0.82 ± 0.01	0.73 ± 0.01	0.95 ± 0.003
3.5	0.80 ± 0.01	0.68 ± 0.01	0.94 ± 0.003
3.6	0.81 ± 0.01	0.69 ± 0.01	0.94 ± 0.003

Table 6.6: Trigger level logic efficiencies for each E_{cm} of interest.

6.5 Backgrounds

There are three main sources of background for the reaction $\bar{p}p \rightarrow e^+e^-$. Hadronic events with a two body final state are the primary source of background.

Specifically, the $\pi^+\pi^-$ final state has kinematics similar to that of the e^+e^- final state. The rejection of this background depends on the different response of the E760 detector to pions and electrons.

The large cross-section for neutral final states that simulate a $\gamma\gamma$ final state will enter as a background to $\bar{p}p \to e^+e^-$ when one or more of the γ's converts in the matter before the Čerenkov detector. This will allow the event to be recorded as a charged event. The last source of background is from the tails of the J/ψ distribution which is calculable from our measurement of the resonance parameters.

6.5.1 Hadronic Rejection Factor

Even though the pion mass is 260 times the electron mass, the final state kinematics of $\bar{p}p \to e^+e^-$ and $\bar{p}p \to \pi^+\pi^-$ are similar. A Monte Carlo simulation generating two electrons in the final state with Gaussian angular resolutions $\sigma_\theta = 4$ mrad and $\sigma_\phi = 7$ mrad is used to demonstrate the kinematic similarity between the $\pi^+\pi^-$ and e^+e^- final states. The variable of interest in this case is the akinematic, $\Delta\theta = \theta_{\text{predicted}} - \theta_{\text{measured}}$, for the final state as calculated for different mass assumptions, Fig. 6.3. Calculations assuming a kaon or proton mass indicate that these two body hadronic final states will constitute a background 2-3 orders of magnitude less than pions.

The rejection of the $\pi^+\pi^-$ final state for this analysis is at the trigger level. Specifically, the detector response as seen by the trigger electronics determines the rejection factor. To study the E760 detector response to the $\pi^+\pi^-$ final state, the second physics trigger (GM5) is used since there is no requirement made on the Čerenkov detector or the CCAL, §3.4.

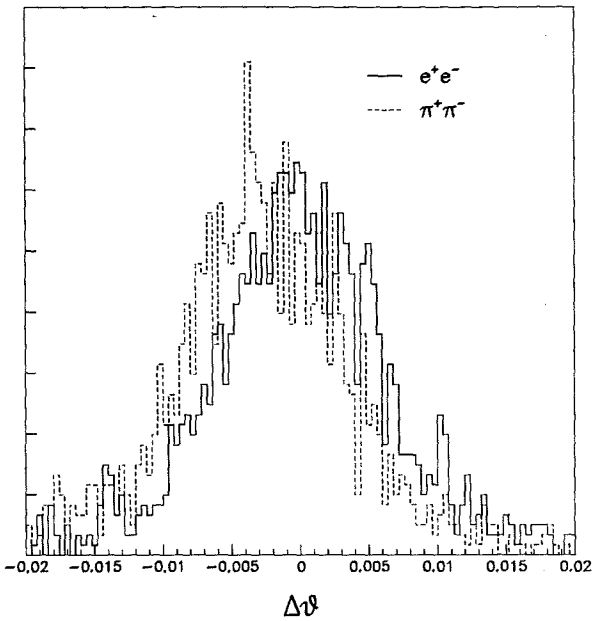

Figure 6.3: Akinematic variable calculated for e^+e^- final state using a pion mass assumption and an electron mass assumption.

The selection of hadronic events from the second physics trigger (GM5) that have similar kinematics to that of pions must be based on the angles and not the energies of the final state particles since the CCAL does not measure hadronic energies. The selection criteria have been refined to:

- $|\Delta\theta_{\text{proton}}| > 0.1$ mrad, akinematic calculated assuming protons in the final state.
- $|\Delta\theta_{\text{pion}}| < 0.1$ mrad, akinematic calculated assuming pions in the final state.
- $|\Delta\phi| < 0.05$ mrad, the final state must be coplanar.
- no forward calorimeter signal and only two charged tracks with associated CCAL clusters. This suppresses the $\pi^+\pi^-\pi^0$ final state.

A two constraint fit was done and found to be superfluous to the above criteria. These events are biased due to the hierarchical nature of the physics

triggers. Events labeled by the second physics (GM5) trigger cannot have satisfied the first physics (GM4) trigger. For this reason, the events selected with the above criteria are searched for events in which at least one of the pions has an associated cluster energy in the range $|E_{\text{cluster}} - 455| < 45$ MeV in the CCAL. This energy range encompasses the peak of the distribution of hadronic energy deposited in the CCAL by pions, Fig. 6.4. The other pion track is used to determine the overall $\pi^+\pi^-$ event rejection factor by searching for those that have some likelihood of being mistaken for an electron.

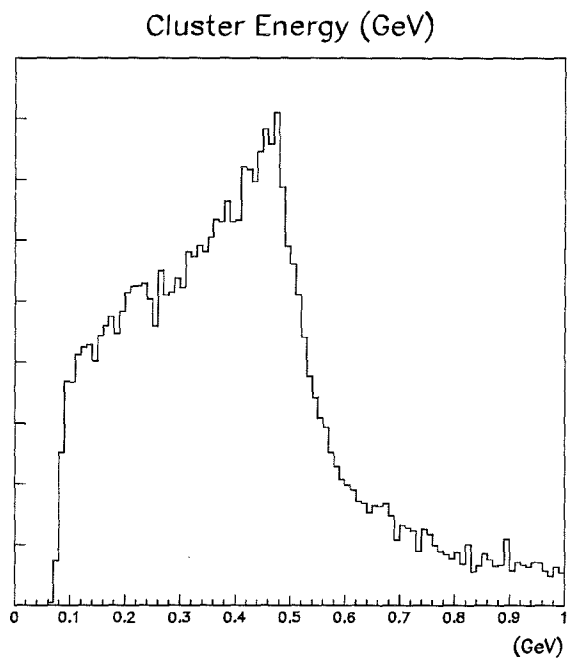

Figure 6.4: Hadronic response of the CCAL for events selected as pions.

The following two criteria are used to determine the similarity of a pion to an electron at the trigger level.

(E_{R1}) $\delta_E = |\frac{(E_{\text{measured}} - E_{\text{expected}})}{E_{\text{expected}}}| < 0.10$, the measured energy of the CCAL cluster within 10% of that expected for the e^+e^- final state.

(E_{R2}) |#Čerenkov photo-electrons| > 0.5, normalized number of photo-electrons from the Čerenkov detector associated with the cluster.

A contingency table analysis [70] was performed to determine any correlation between δ_E and the number of Čerenkov detector photo-electrons. The result is that the two variables have a zero χ^2 probability of being associated. The criteria E_{R1} and E_{R2} are used to calculate the rejection factor due to the CCAL, R_{CCAL}, and the Čerenkov detector, $R_{\check{C}}$, respectively. A summary of the rejection factors is found in Table 6.7. Since both pion tracks must simulate electrons to be considered as background, the total rejection factor at the trigger level is $(R_{\check{C}} \times R_{CCAL})^2$.

Pion Rejection Factors

# of candidate tracks	# tracks with E_{R1}	# tracks with E_{R2}
4659	11	214

R_{CCAL}	$R_{\check{C}}$	$(R_{\check{C}} \times R_{CCAL})^2$
$(2.4 \pm 0.7) \times 10^{-3}$	$(4.6 \pm 0.3) \times 10^{-2}$	$(1.3 \pm 0.8) \times 10^{-8}$

Table 6.7: The detector rejection factors and the total rejection factor for the $\pi^+\pi^-$ final state.

6.5.2 Estimation of $\pi^+\pi^-$ Background Cross Section

An estimation of the $\bar{p}p \to \pi^+\pi^-$ differential cross section is needed to determine the background level for $\bar{p}p \to e^+e^-$. While the total cross section for $\bar{p}p \to \pi^+\pi^-$ is known at $\sqrt{s} = 3.077$ GeV [71], the differential cross section is needed to estimate what part of the total may be detected by E760. The differential cross sections for $\bar{p}p \to \pi^+\pi^-$ are found in the literature for several different values of $\sqrt{s}$.

$s = 6.42$ GeV^2

$\cos\vartheta^*$	$\frac{d\sigma}{d(\cos\vartheta^*)}(\mu\text{b})$
0.0526	4.89 ± 1.70
0.1513	4.89 ± 1.70
0.2500	5.28 ± 1.70
0.3553	8.07 ± 3.18
0.4539	11.88 ± 4.32
0.5526	10.4 ± 3.52
0.6513	6.59 ± 2.95
0.7566	4.83 ± 2.44
0.8553	5.17 ± 2.61
0.9539	10.28 ± 3.52

Table 6.8: Differential cross section measurements for the process $\bar{p}p \rightarrow \pi^+\pi^-$ at $s = 6.42$ GeV^2, Fields, *et al.*[72].

The data in the literature [72] [73] [74] are in Tables 6.8, 6.9, 6.10 respectively. The data from [73] and [74] are given as differential cross sections with respect to t, the Mandelstam invariant. Conversion of these data to differential cross sections with respect to $\cos\vartheta^*$ involves only a kinematic factor. In the case of [72], a factor of 8π is needed to convert the differential cross section into (μb) from (μb/sr). The extra factor of 2^2 indicates a different normalization between the data of Fields and those of Eide and Buran.

According to Brodsky [75], the differential cross section scales with the variable s according to Equation 6.3.

$$\frac{d\sigma}{d(\cos\vartheta^*)} \simeq \frac{1}{s^7} f(\cos\vartheta^*) \tag{6.3}$$

The scale factors between $\sqrt{s} = 3.077$ GeV and $s = 6.42$, 11.307, 13.546 (GeV)^2 are 0.066, 3.46, 12.27 respectively. The data from Eide and Fields are plotted in Figure 6.5.

$s = 11.307$ GeV^2

$\cos\vartheta^*$	$\frac{d\sigma}{d(\cos\vartheta^*)}(\mu\text{b})$	$\cos\vartheta^*$	$\frac{d\sigma}{d(\cos\vartheta^*)}(\mu\text{b})$
0.9215	13.605 ± 3.284	0.5698	3.425 ± 0.891
0.9002	15.950 ± 2.815	0.5272	2.815 ± 0.985
0.8789	12.667 ± 2.346	0.4845	4.457 ± 1.501
0.8576	14.543 ± 2.346	0.4206	3.894 ± 1.454
0.8363	10.321 ± 1.877	0.1648	0.230 ± 0.117
0.8149	10.790 ± 1.877	-0.2615	0.1642 ± 0.084
0.7936	7.037 ± 1.407	-0.6239	0.1642 ± 0.075
0.7723	7.975 ± 1.407	-0.7944	0.9383 ± 0.422
0.7510	6.568 ± 1.407	-0.8371	2.2518 ± 0.61
0.7297	6.568 ± 1.877	-0.8797	2.956 ± 0.751
0.6977	2.674 ± 0.704	-0.9117	7.975 ± 1.877
0.6551	2.909 ± 0.798	-0.9330	7.975 ± 1.877
0.6124	4.035 ± 0.938	-0.9543	7.975 ± 2.346

Table 6.9: Differential cross section measurements for the process $\bar{p}p \to \pi^+\pi^-$ at $s = 11.307$ GeV^2, Eide, *et al.*[73].

There is an obvious disagreement in the data for $|\cos\vartheta^*| > 0.6$. The forward peak is due to the onset of baryon exchange [73] which occurs when $s \approx 7$ (GeV)^2. Below this threshold, the cross section is dominated by direct channel effects. Baryon exchange is expected to dominate direct channel processes for small $|t|$ above the 7 (GeV)^2 threshold. The scaled data from Fields, Eide and Buran are combined in Figure 6.6. Only the data with $|\cos\vartheta^*| < 0.6$ from Fields are used in Figure 6.6.

The total cross section at $\sqrt{s} = 3.077$ GeV is measured to be $7 \pm 5\mu$b [71]. Less than 10% of the total cross section for $\bar{p}p \to \pi^+\pi^-$ impinges upon the E760 detector, as can be seen from Figure 6.6b. Using the total rejection factor from the previous section, the total background cross section from $\bar{p}p \to \pi^+\pi^-$ is less than 0.01 pb for $\sqrt{s} = 3.077$ GeV. This can be taken as an upper limit at all E760

$s = 13.546$ GeV^2

$\cos\vartheta^*$	$\frac{d\sigma}{d(\cos\vartheta^*)}(\mu\text{b})$	$\cos\vartheta^*$	$\frac{d\sigma}{d(\cos\vartheta^*)}(\mu\text{b})$
0.933	3.904 ± 0.76	0.649	0.915 ± 0.37
0.916	3.787 ± 0.76	0.615	0.373 ± 0.26
0.899	5.477 ± 0.93	0.546	0.221 ± 0.13
0.882	4.836 ± 0.87	-0.555	0.093 ± 0.07
0.865	4.079 ± 0.82	-0.667	0.117 ± 0.08
0.847	3.438 ± 0.76	-0.753	0.28 ± 0.12
0.830	3.496 ± 0.82	-0.814	0.565 ± 0.23
0.813	3.03 ± 0.82	-0.848	0.682 ± 0.27
0.787	1.305 ± 0.41	-0.882	0.548 ± 0.23
0.753	1.002 ± 0.32	-0.917	1.049 ± 0.27
0.718	0.868 ± 0.32	-0.960	1.049 ± 0.23
0.683	0.822 ± 0.32		

Table 6.10: Differential cross section measurements for the process $\bar{p}p \to \pi^+\pi^-$ at $s = 13.546$ GeV^2, Buran, *et al.*[74].

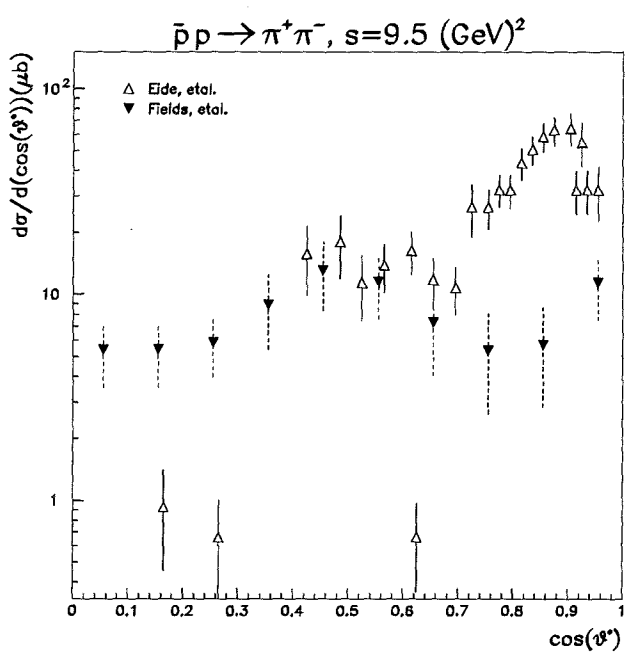

Figure 6.5: Differential cross section data from [73] and [72] scaled to $s = 9.5$ GeV^2.

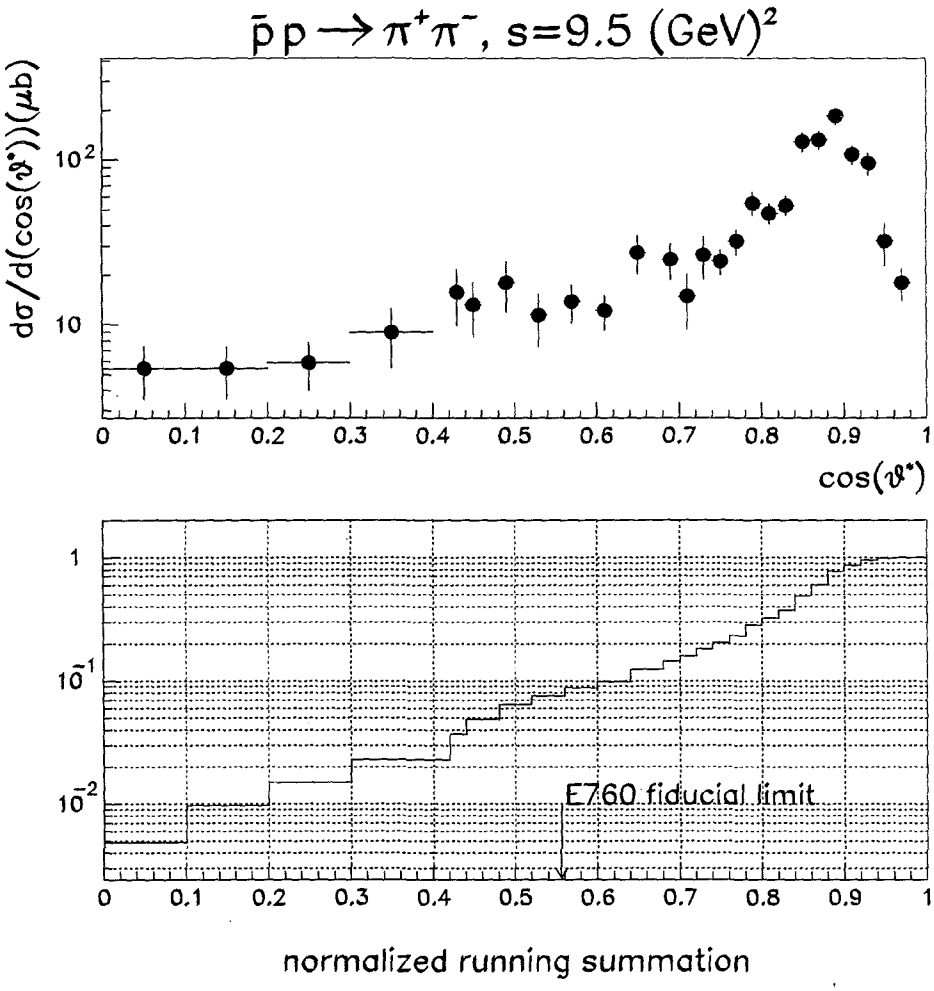

Figure 6.6: The combined scaled data from Eide and Buran and from Fields for $|\cos(\vartheta^*)| < 0.6$ are presented in (a). The percentage of the total cross section available to E760 is shown in (b).

energies since the total cross section is known to decrease with increasing center of mass energy.

6.5.3 Tails Of The J/ψ Distribution

The e^+e^- final state can be produced via single photon intermediate state or a resonantly produced vector meson, J/ψ. When considering only the total cross sections, these two virtual processes are indistinguishable. Therefore, the exchange of an intermediate vector meson is considered a background process.

The magnitude of the cross section for this background can be easily calculated using a Breit-Wigner resonance formula. In Equation 6.4

$$\sigma_{\mathrm{BW}}(s) = \frac{(2J+1)}{(2S+1)(2S+1)} \left\{ \frac{4\pi(\hbar c)^2}{(s-4(m_p c^2)^2)} \frac{B_{\mathrm{in}} B_{\mathrm{out}} \Gamma_{\mathrm{R}}^2}{[(\sqrt{s} - M_{\mathrm{R}} c^2)^2 + \Gamma_{\mathrm{R}}^2/4]} \right\}, \tag{6.4}$$

S is the spin of the proton, B_{in} and B_{out} are the branching ratios for the formation and decay channels respectively, and M_{R}, J and Γ_{R} are the mass, total spin and width of the resonance. The cross section is dependent on the total center of mass energy, $\sqrt{s}$. The results for the J/ψ resonance parameters from E760 are show in Table 6.11 and used in the calculation.

E760 final results for J/ψ resonance.

Width (keV)	$B(\bar{p}p \to J/\psi)B(J/\psi \to e^+e^-)$	Mass (MeV)[a]
$99 \pm 12 \pm 6$	$(1.14^{+0.16}_{-0.12} \pm 0.10) \times 10^{-4}$	3096.93 ± 0.3

[a] The J/ψ mass is quoted from the Particle Data Group [76].

Table 6.11: E760 results for the J/ψ resonance parameters [77].

The result of the calculation indicates that the largest background contribution is at $\sqrt{s} = 2.95$ GeV and is $\approx 4 \times 10^{-5}$ pb. This is a negligible amount of background.

6.5.4 Two Photon Conversions

In §5.1, the estimation of $\gamma\gamma$ events simulated by $\pi^0\pi^0$ and $\pi^0\gamma$ events is discussed. This neutral background will also be a background to the e^+e^- final state when both the photons convert into an e^+e^- pair in the material before the H1 hodoscope or ≈ 0.05 cm from each projected exit point. Photon conversions in this material will satisfy the trigger requirement of two charged particle tracks.

A Monte Carlo simulation [57] was used to determine the average probability that a photon will convert within the required volume. The result, $(1.7 \pm 0.01)\%$, is consistent with calculations using the known geometry and radiation lengths. Since both photons must convert to satisfy the charged trigger, the event probability for being in the charged trigger is $(0.029)\%$.

The differential cross section of neutral events which satisfy the $\gamma\gamma$ requirements is estimated at each energy used in this analysis. This differential cross section multiplied by the conversion probability is used in the likelihood analysis to represent this background.

6.6 Results and Likelihood Analysis

The active volume of the E760 detector in the center of mass is calculated to be $|\cos(\vartheta^*)|_{\max} \leq 0.45$, 0.60, and 0.61 for $s = 8.82$, 12.43, and 12.85 GeV^2 respectively where ϑ^* is the center of mass polar angle. The differential cross section for the process $\bar{p}p \to e^+e^-$ [78] in terms of the Sachs proton form factors, G_E and G_M, and center of mass variables is

$$\frac{d\sigma}{d(\cos\vartheta^*)} = \frac{\pi\alpha^2(\hbar c)^2}{8EP} \times \left[|G_M|^2(1+\cos^2\vartheta^*) + \frac{4m_p^2}{q^2}|G_E|^2\sin^2\vartheta^* \right] \quad . \tag{6.5}$$

Here q^2, E, and P are respectively the momentum transfer squared, the center of mass energy and momentum. Equation 6.5 integrated over the active volumes gives the total cross sections which correspond to the number of events counted at each energy. Table 6.12 lists the measured cross sections based on the efficiency corrected luminosities. Using these corrected cross sections and the integral of Equation 6.5,

$$\sigma_{\text{corr}} = \frac{\pi\alpha^2(\hbar c)^2}{8EP}\left[A|G_M|^2 + \frac{4m_p^2}{q^2}B|G_E|^2\right], \tag{6.6}$$

where

$$A = 2\int_0^{|\cos(\vartheta^*)|_{\max}} (1+\cos^2\vartheta^*)\, d(\cos(\vartheta^*))$$

and

$$B = 2\int_0^{|\cos(\vartheta^*)|_{\max}} (\sin^2\vartheta^*)\, d(\cos(\vartheta^*)),$$

G_M is calculated for the two assumptions (a) $G_M = G_E$ and (b) $G_E = 0$.

Measured Results For e^+e^- Events

s	L	σ_{corr}	A	B	G_M	
GeV^2	pb^{-1}	pb			(a)	(b)
8.82	2.9	$6.5^{+2.3}_{-1.8}$	0.96	0.84	0.032 ± 0.005	0.038 ± 0.006
12.43	16.1	$1.5^{+0.5}_{-0.3}$	1.34	1.06	$0.017^{+0.003}_{-0.002}$	$0.019^{+0.003}_{-0.002}$
12.85	6.1	$2.0^{+0.9}_{-0.7}$	1.37	1.07	0.020 ± 0.004	0.022 ± 0.004

Table 6.12: Results for the proton form factor as calculated from the measured number of events and efficiency corrected luminosities, i.e. $\sigma_{\text{corr}} = N/\epsilon L$. The errors on the cross sections reflect the counting statistics.

The $\gamma\gamma$ background is the largest background by an order of magnitude. For the $|\cos(\vartheta^*)|$ limits, the total cross section at each energy is 0.126, 0.021, and 0.057 pb for $s = 8.82$, 12.43, and 12.85 GeV^2 respectively. This corresponds to < 0.3 events for $s = 8.82$ and 12.43 and < 0.06 events for $s = 12.85$. Because there is also information on the shape of the $\gamma\gamma$ background, a likelihood function of the variable, $x \equiv |\cos(\vartheta^*)|$ may be written. The unnormalized event probability for the

e^+e^- events at the jth energy is,

$$F_j(x;\vec{a}) = \epsilon_j L_j \left(g_j(x;C) + b_j(x)\right)$$

The factor $\epsilon_j L_j$ is the effective luminosity at the jth energy. g_j and b_j represent the signal and background differential cross sections at the jth energy point respectively. The parameter C will be determined by the likelihood fit to the data.

In this instance, the signal cross section is just Equation 6.5. With the Equations 1.1 and 1.7, the proton form factor, G_M, can be written as

$$G_M(q^2) = \frac{16\pi^2}{81} C \frac{1}{q^4} \left(\ln \frac{q^2}{\Lambda^2}\right)^{-58/27}$$

so that the signal cross section can be written with the energy dependence explicit up to a single proportionality constant, C.

As in §5.6, the background from neutral events is represented by a polynomial fit to the Monte Carlo simulation of the differential cross section at each energy, ($x \equiv \cos\vartheta^*$).

$$p_j(x) = p_{1,j} + p_{2,j}x^2 + p_{3,j}x^4 + p_{4,j}x^6$$

Therefore, the total event probability at each energy may be written as

$$F_j(x) = \epsilon_j L_j (\frac{d\sigma}{dx} + 2.9 \times 10^{-4} p_j(x)) \,,$$

where 2.9×10^{-4} is the square of the conversion probability for photons in the material before the detectors which define the trigger. In order to write the likelihood function, the total number of events at each energy, $\overline{n}_j$, is estimated as the integral of the event probability over the active volume of the detector.

$$\bar{n}_j = \epsilon_j L_j \int_0^{x_{c,j}} F_j(x;C)\, dx \,,$$

η_c Results

M_{η_c} (MeV/c^2)	$2988.1^{+3.1}_{-2.6}$
$\Gamma_{\gamma\gamma}$ (KeV)	$6.9^{+2.3}_{-1.6} \pm 2.3$
$B(\eta_c \to \gamma\gamma) \times 10^4$	$3.03^{+0.65}_{-0.56} \pm 1$
Γ_{total} (MeV)	$22.6^{+10.3}_{-6.3}$
$B(\eta_c \to \bar{p}p)B(\eta_c \to \gamma\gamma) \times 10^8$	$36.3^{+7.8}_{-6.7}$
$B(\eta_c \to \bar{p}p)\Gamma_{\gamma\gamma}$ (eV)	$8.2^{+2.8}_{-1.9}$
$\Gamma_{\gamma\gamma}$ (KeV)	$6.9^{+2.3}_{-1.6}$

These are the results for the likelihood analysis in §5.6. The resonance
: same for each of the 3 possible sets of fit parameters. The systematic
the value for $B(\eta_c \to \bar{p}p)$ is shown.

y different from previous measurements, Figure 7.1. To extract the
th, $\Gamma_{\gamma\gamma}$, and branching fraction, $B(\eta_c \to \gamma\gamma)$, the Particle Data Group
average for $B(\eta_c \to \bar{p}p)$, $(12 \pm 4) \times 10^{-4}$, is used. This is the principal
ystematic error on the partial width and branching fraction
nts. Figure 7.2 compares this measurement of the partial width, $\Gamma_{\gamma\gamma}$, to
asurements.

ıg the world averages for the Z boson mass, $m_Z = 91.187$ GeV/c^2, and
coupling constant, $\alpha_s(m_Z) = 0.117$, the value of $\alpha_s(m_c)$ can be calculated
$\overline{MS}$ renormalization scheme. Values of $\alpha_s(m_c)$ for several choices of m_c
ı Table 7.2. The choice of 1.49 GeV/c^2 for the mass of the charm quark
2 corresponds to half the mass of the η_c charmonium resonance. The
.85 GeV/c^2 for the mass of the charm quark in Table 7.2 corresponds to
ıodel results for the mass of the charm quark.

Chapter 7

Inferences and Comparisons

The processes

$$\bar{p}p \rightarrow \eta_c(^1S_0) \rightarrow \gamma\gamma$$

$$\bar{p}p \longrightarrow \gamma\gamma$$

$$\bar{p}p \longrightarrow e^+e^-$$

have been studied in detail. Measurements of each process are given with estimates and sources of the systematic errors. The significance of these measurements with regard to previous data and theoretical considerations is presented.

7.1 η_c Results

The likelihood function in §5.6 can be minimized with respect to several sets of parameters which consist of the resonance mass and a combination of the branching fractions, $B(\eta_c \rightarrow \bar{p}p)$ and $B(\eta_c \rightarrow \gamma\gamma)$, and the total width of the resonance. Table 7.1 contains the results for each set of parameters. The set of fit parameters with the smallest correlations is M_{η_c}, $\Gamma_{\gamma\gamma}$, and $B(\eta_c \rightarrow \gamma\gamma)$.

The effective luminosity is measured with better than 5% accuracy. This corresponds to a systematic error in the resonance parameters which is negligible compared to the statistical significance of the data. The mass measurement is

η_c Results

M_{η_c} (MeV/c^2)	$2988.1^{+3.1}_{-2.6}$
$\Gamma_{\gamma\gamma}$ (KeV)	$6.9^{+2.3}_{-1.6} \pm 2.3$
$B(\eta_c \to \gamma\gamma) \times 10^4$	$3.03^{+0.65}_{-0.56} \pm 1$
Γ_{total} (MeV)	$22.6^{+10.3}_{-6.3}$
$B(\eta_c \to \bar{p}p)B(\eta_c \to \gamma\gamma) \times 10^8$	$36.3^{+7.8}_{-6.7}$
$B(\eta_c \to \bar{p}p)\Gamma_{\gamma\gamma}$ (eV)	$8.2^{+2.8}_{-1.9}$
$\Gamma_{\gamma\gamma}$ (KeV)	$6.9^{+2.3}_{-1.6}$

Table 7.1: These are the results for the likelihood analysis in §5.6. The resonance mass is the same for each of the 3 possible sets of fit parameters. The systematic error from the value for $B(\eta_c \to \bar{p}p)$ is shown.

significantly different from previous measurements, Figure 7.1. To extract the partial width, $\Gamma_{\gamma\gamma}$, and branching fraction, $B(\eta_c \to \gamma\gamma)$, the Particle Data Group (PDG) [76] average for $B(\eta_c \to \bar{p}p)$, $(12 \pm 4) \times 10^{-4}$, is used. This is the principal source of systematic error on the partial width and branching fraction measurements. Figure 7.2 compares this measurement of the partial width, $\Gamma_{\gamma\gamma}$, to several measurements.

Using the world averages for the Z boson mass, $m_Z = 91.187$ GeV/c^2, and the strong coupling constant, $\alpha_s(m_Z) = 0.117$, the value of $\alpha_s(m_c)$ can be calculated within the $\overline{MS}$ renormalization scheme. Values of $\alpha_s(m_c)$ for several choices of m_c are given in Table 7.2. The choice of 1.49 GeV/c^2 for the mass of the charm quark in Table 7.2 corresponds to half the mass of the η_c charmonium resonance. The choice of 1.85 GeV/c^2 for the mass of the charm quark in Table 7.2 corresponds to potential model results for the mass of the charm quark.

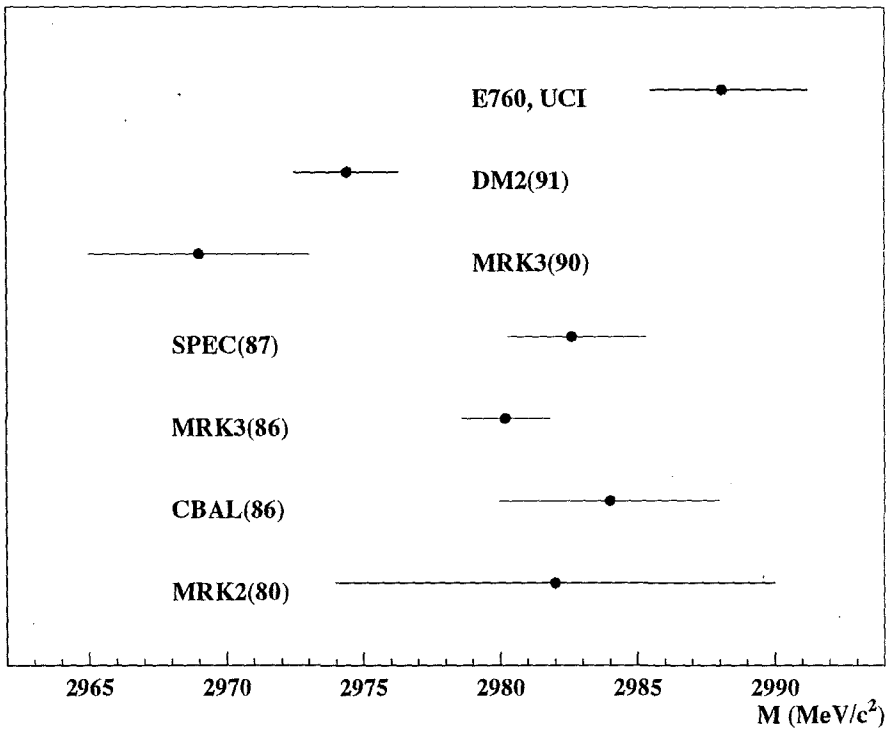

Figure 7.1: The result for the resonance mass is presented along with several other results used to determine the Particle Data Group [76] world average, 2978.8 ± 1.9 MeV/c^2.

Since the partial width $\Gamma_{\gamma\gamma}$ is small compared to the total width, the branching fraction, $1/B(\eta_c \to \gamma\gamma)$, approximates the ratio $\Gamma_{gg}/\Gamma_{\gamma\gamma}$ found in Equation 1.6. Solving the cubic equation for the strong coupling constant gives $\alpha_s(m_c) = 0.28 \pm 0.04$. The error represents the combination of statistical and systematic errors for this experiment. This experimental result compares favorably with the values in Table 7.2 within the experimental errors. The theoretical errors in Equation 1.6 from neglecting relativistic corrections may be comparable to the experimental errors.

By assuming that the square of the wave function at the origin, $|\Psi(0)|^2$, is the nearly same for both the J/ψ and the η_c resonances up to relativistic effects, the

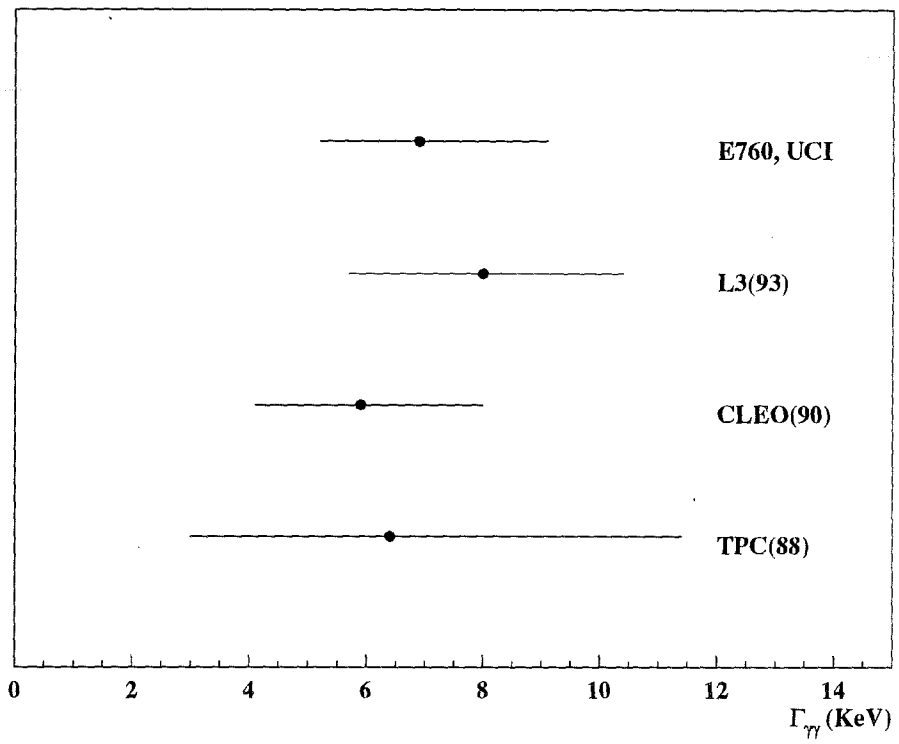

Figure 7.2: The result for $\Gamma_{\gamma\gamma}$ is presented along with several other results used to determine the Particle Data Group [76] world average, $6.6^{+2.4}_{-2.1}$ keV.

	$\alpha_s(m_c)$
$m_c = 1.49$ GeV/c^2	0.347
$m_c = 1.85$ GeV/c^2	0.307
$m_c = 2.0$ GeV/c^2	0.295

Table 7.2: The running strong coupling constant in the $\overline{MS}$ scheme at different values for the mass of the charm quark and for $\Lambda_{\rm QCD} = 200$ MeV.

ratio,

$$\frac{\Gamma(\eta_c \to \gamma\gamma)}{\Gamma(J/\psi \to e^+e^-)} = \frac{4}{3}\left[1 + \frac{\pi^2 - 4}{3}\frac{\alpha_s}{\pi}\right]\left(1 + C\frac{v^2}{c^2}\right) \quad ,$$

can be solved for $C\frac{v^2}{c^2}$ to estimate the magnitude of the relativistic corrections. The result is $C\frac{v^2}{c^2} = -0.16 \pm 0.72$ where the error is from the systematic error quoted for $\Gamma(\eta_c \to \gamma\gamma)$ in Table 7.1. The value for $\Gamma(J/\psi \to e^+e^-)$ is taken to be the PDG average, 5.26 KeV.

7.2 Exclusive Electromagnetic Final States

Figure 7.3 shows the values of the proton magnetic form factor for the assumption $|G_M| = |G_E|$ as the quantity $q^4|G_M|/\mu_p$ vs. q^2 where μ_p is the proton magnetic moment. The magnitude of the measurements is consistent with a ratio of 3 between the time-like and the space-like data for similar momentum transfers. This may indicate that the range of momentum transfers in this experiment is still not an asymptotic region for the proton form factor and/or that nonperturbative effects are still large.

As indicated in §5.6, a nonzero $\gamma\gamma$ continuum is inconsistent with the data. A 90% confidence level upper limit of 29 pb for the parameter A in Equation 5.28 is found using these data. This value for the $\gamma\gamma$ continuum cross section for $|\cos(\vartheta^*)| \leq 0.30$ is related to the process $\gamma\gamma \to \bar{p}p$ by

$$\sigma(\bar{p}p \to \gamma\gamma) = \frac{1}{2}\left(\frac{p_\gamma}{p_p}\right)^2 \sigma(\gamma\gamma \to \bar{p}p)\,. \tag{7.1}$$

Equation 7.1 is a consequence of detailed balance. The factor of 1/2 arises from identical particles in the final state of the reaction on the left hand side of Equation 7.1. Using the momentum correction factor of 1.58 at $\sqrt{s} = 3.097$ GeV,

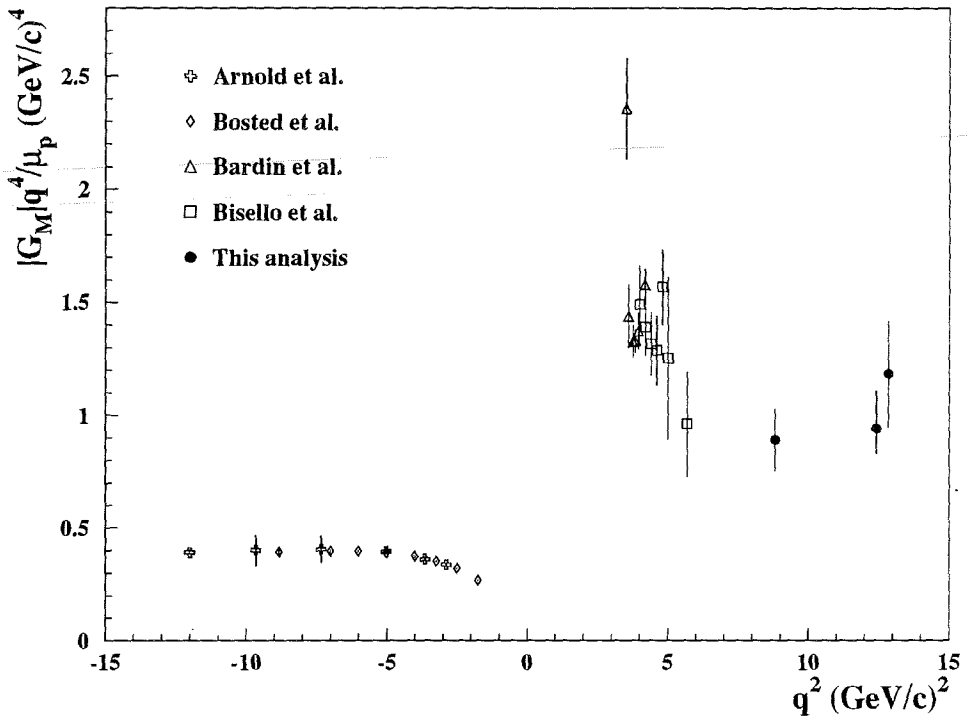

Figure 7.3: The quantity $q^4|G_M|/\mu_p$ is plotted versus q^2 for space-like and time-like momentum transfers with $|q^2| < 15$ (GeV/c)^2.

the 90% upper limit for the process $\gamma\gamma \to \bar{p}p$ is found to be 37 pb at $\sqrt{s} = 3.097$ GeV.

The results for the process $\gamma\gamma \to \bar{p}p$ found in [64, p.100] are presented as cross sections for $|\cos(\vartheta^*)| \leq 0.60$. From the reported shape, approximately 30% of this cross section is found for $|\cos(\vartheta^*)| \leq 0.30$ which corresponds to a value of 33^{+27}_{-21} pb. The errors have been scaled by 30% also. The experimental limit of 37 pb and this measurement are consistent.

7.3 Comparison of Exclusive Electromagnetic Final States

An upper limit for the ratio,

$$R_{\gamma\gamma/e^+e^-} = \frac{\sigma(\bar{p}p \to \gamma\gamma)}{\sigma(\bar{p}p \to e^+e^-)},$$

for $|\cos(\vartheta^*)| \leq 0.30$ and $\sqrt{s} = 2.97$ GeV is found to be $R_{\gamma\gamma/e^+e^-} < 6$. This upper limit is difficult to compare with the theoretical predictions provided in Hyer's paper [33, Table III] where Hyer has calculated $R_{\gamma\gamma/e^+e^-}$ for $0 < \cos(\vartheta^*) < 0.866$ and $\sqrt{s} = 5$ GeV. By referring to [33, Figure 12], estimates for $R_{\gamma\gamma/e^+e^-}$ can be made. For several different parameterizations of the proton valence quark wave functions [29, 79, 30, 32], Hyer predicts $R_{\gamma\gamma/e^+e^-}$ in the range 0.65 to 7.4. While the experimental result $R_{\gamma\gamma/e^+e^-} < 6$ is consistent with Hyer's predictions, precision tests of the proton wave function by measuring $R_{\gamma\gamma/e^+e^-}$ await more data and further theoretical considerations.

Bibliography

[1] S. VAN DER MEER, *Stochastic damping of betatron oscillations in the isr*, Tech. Rep. CERN/ISR-PO/72-31, CERN, 1972. D. MOHL, G. PETRUCCI, L. THORNDAHL, and S. VAN DER MEER, Physics and Technique of Stochastic Cooling, *Physics Reports (Physics Letters C)*, **58** (1980)73–119.

[2] S. WEINBERG, A Model of Leptons, *Physical Review Letters*, **19** (1967)1264. A. SALAM, *Elementary particle theory: Relativistic groups and analyticity*, in (8th Nobel Symposium), A. N. Svartholm and Wiksel, eds., Stockholm, 1968.

[3] S. GLASHOW, J. ILIOPOULOS, and L. MAIANI, *Physical Review*, **D2** (1970)1285.

[4] J. AUBERT *et al.*, Experimental Observation of a Heavy Particle J, *Physical Review Letters*, **33** (1974)1404.

[5] J. AUGUSTIN *et al.*, Discovery of a Narrow Resonance in e^+e^- Annihilation, *Physical Review Letters*, **33** (1974)1406.

[6] W. BRAUNSCHWEIG *et al.*, Observation of the two-photon cascade $3.7 \to 3.1 + \gamma\gamma$ via an intermediat state P_c, *Physics Letters*, **B57** (1975)407.

[7] G. FELDMAN *et al.*, $\psi(3684)$ radiative decays to high-mass states, *Physical Review Letters*, **35** (1975)821.

[8] W. TANENBAUM *et al.*, Observation of an intermediate state in $\psi(3684)$ radiative cascade decay, *Physical Review Letters*, **35** (1975)1323.

[9] H. POTH, ed., *Proceedings of the joint CERN-KfK Workshop on Physics with Cooled Low Energetic Antiprotons*, vol. KfK 2386, May 1979.

[10] BAGLIN *et al.*, Formation of the χ_1 and χ_2 Charmonium Resonances in $\bar{p}p$ Annihilation and Measurements of Their Masses and Total Widths, *Physics Letters*, **B172** (1986)455.

[11] M. MACRI, *Gas jet targets*, Tech. Rep. CERN 85-15, CERN Accelerator Summer School 1983, 1985.

[12] E. EICHTEN, K. GOTTFRIED, T. KINOSHITA, J. KOGUT, K. LANE, and T. YAN, Spectrum of charmed quar-antiquark bound states, *Physical Review Letters*, **34** (1975)369. ——, Charmonium: The model, *Physical Review*, **D17**

(1978)3090. ——, Charmonium: Comparison with experiment, *Physical Review*, **D21** (1980)203.

[13] T. APPELQUIST and H. POLITZER, Heavy quarks and e^+e^- annihilation, *Physical Review Letters*, **34** (1975)43.

[14] W. LUCHA, F. SCHÖBERL, and D. GROMES, Bound states of quarks, *Physics Reports*, **200** (1991)127.

[15] A. KRONFELD and P. MACKENZIE, Progress in QCD Using Lattice Gauge Theory, *Annual Review of Nuc. and Part. Science*, **43** (1993)793–828.

[16] A. EL-KHADRA, Lattice QCD, *Physics in Collisions '94*, (1994). Invited talk presented at the International Symposium *Physics in Collisions '94*, Tallahassee, Florida.

[17] C. DAVIES, K. HORNBOSTEL, G. LEPAGE, A. LIDSEY, J. SHIGEMITSU, and J. SLOAN, A Precise Determination of α_s from Lattice QCD, *Physics Letters*, **B345** (1995)42–48.

[18] G. SCHULER, *Quarkonium production and decays*, Tech. Rep. CERN-TH.7170/94, Theory Division, CERN, February 1994. p. 28.

[19] W. KEUNG and I. MUZINICH, Beyond the static limit for quarkonium decays, *Physical Review*, **D27** (1983)1518.

[20] R. BARBIERI, G. CURCI, E. D'EMILIO, and E. REMIDDI, Strong Radiative Corrections to Annihilations of Quarkonia in QCD, *Nuclear Physics*, **B154** (1979)535–546.

[21] W. KWONG, P. MACKENZIE, R. ROSENFELD, and J. ROSNER, Quarkonium Annihilation Rates, *Physical Review*, **D37** (1988)3210.

[22] G. BODWIN, E. BRAATEN, and G. LEPAGE, Rigorous QCD Analysis of Inclusive Annihilation and Production of Heavy Quarkonium, *Physical Review*, **D51** (1995)1125–1171.

[23] H. KAHN and P. HOODBHOY, A Systematic Gauge Invariant Approach to Heavy Quarkonium Decay, **HEPPH-9501409** (1995). e-Print Archive.

[24] M. ROSENBLUTH, High Energy Elastic Scattering of Electrons on Protons, *Physical Review*, **79** (1950)615.

[25] R. ARNOLD *et al.*, Measurement of Elastic Electron Scattering from the Proton at High Momentum Transfer, *Physical Review Letters*, **57** (1986)174.

[26] G. BARDIN *et al.*, Measurement of the Proton Electromagnetic Form-Factor Near Threshold in the Timelike Region, *Physics Letters*, **B255** (1991)149.

[27] G. LEPAGE and S. BRODSKY, Exclussive Processes in Perturbative Quantum Chromodynamics, *Physical Review*, **D22** (1980)2157.

[28] S. BRODSKY and G. FARRAR, Scaling Laws for Large-Momentum-Transfer Processes, *Physical Review*, **D1** (1975)1309.

[29] V. CHERNYAK and I. ZHITNITSKY, Nucleon Wave Function and Nucleon Form-Factors in QCD, *Nuclear Physics*, **B246** (1984)52.

[30] I. KING and C. SACHRAJDA, Nucleon Wave Functions and QCD Sum Rules, *Nuclear Physics*, **B279** (1987)785.

[31] V. CHERNYAK, A. OGLOBLIN, and I. ZHITNITSKY, Wave Functions of Octet Baryons, *Zeitschrift fur Physik*, **C42** (1989)569.

[32] M. GARI and N. STEFANIS, Electromagnetic Form-Factors of the Nucleon from Perturbative QCD and QCD Sum Rules, *Physics Letters*, **B175** (1986)462. ——, Quark Distribution Amplitudes for the Nucleon from Perturbative QCD and QCD Sum Rules, *Physical Review*, **D35** (1987)1074.

[33] T. HYER, Sudakov effects in $p\bar{p}$ annihilation, *Physical Review*, **D47** (1993)3875.

[34] P. KROLL, *Electromagnetic form factors at large momentum transfer*, Tech. Rep. WU-B 94-17, Universität Wuppertal, August 1994. Invited talk presented at the Intern. Conf. on Physics with GeV-Particle Beams, Jülich (1994).

[35] S. BILENKY, C. GIUNTI, and V. WATAGHIN, *The process $\bar{p}p \to e^+e^-$ with polarized initial particles and proton form factors in the time-like region*, Tech. Rep. DFTT 13/93, Dipartimento di Fisica Teorica, Università di Torino, March 1993.

[36] E. TITCHMARSH, *The Theory of Functions*, Oxford University Press, 1939. M. SUGAWARA and A. KANAZAWA, Subtractions in Dispersion Relations, *Physical Review*, **123** (1961)1895. N. MEĬMAN, Asymptotic Equality of the Total Cross Sections of Particle and Anti-Particle, *English Translation of Soviet Physics ZETF*, **16** (1963)1609.

[37] L. MAGNEA and G. STERMAN, Analytic Continuation of the Sudakov Form-Factor in QCD, *Physical Review*, **D42** (1990)4222–4227.

[38] FERMI NATIONAL ACCELERATOR LABORATORY, *Design report tevatron 1 project*, tech. rep., Universities Research Association, Inc., September 1984.

[39] E. COURANT and H. SNYDER, Theory of the Alternating-Gradient Synchrotron, *Annals of Physics*, **3** (1958)1–48.

[40] W. WENG and S. MANE, *Fundamentals of particle beam dynamics and phase space*, in The Physics of Particle Accelerators, M. Month and M. Dienes, eds., vol. I, (1992)3–45.

[41] J. MARRINER and D. MCGINNIS, *An introduction to stochastic cooling*, in The Physics of Particle Accelerators, M. Month and M. Dienes, eds., vol. I, (1992)693–761.

[42] D. MÖHL, *Stochastic cooling for beginners*, Tech. Rep. CERN 84-15, December 1984. p. 97.

[43] V. BHARADWAJ *et al.*, *Operation of the fermilab accumulator for medium energy proton-antiproton physics*, in Proceedings of the European Particle Accelerator Conference, June (1990)617–619.

[44] M. CHURCH, S. HSUEH, P. RAPIDIS, and S. WERKEMA, *Energy and energy width measurement in the fnal antiproton accumulator.* E760 internal memo. #273.

[45] S. WERKEMA, *Re-analysis of the summer 1990 ψ' scans using beam energies derived from a new orbit length calculation.* E760 internal memo. #260, and possibly a subsequent FNAL technical report.

[46] S. TROKENHEIM, M. SARMIENTO, K. K. SETH, and L. BARTOSZEK, A $\bar{p}p$ luminosity monitor for Fermilab experiment E760, *Nuclear Instruments and Methods*, **A355** (1995)308–319. S. TROKENHEIM and K. K. SETH, *Effects of beam movement on luminosity monitor measurements.* E760 internal memo, March 1993. # 300. S. TROKENHEIM, *The final word on e760 luminosities.* E760 internal memo, January 1994. # 309.

[47] C. BIINO *et al.*, A large acceptance threshold Cherenkov counter for Experiment 760 at Fermilab, *Nuclear Instruments and Methods*, **A317** (1992)135–142.

[48] R. CALABRESE *et al.*, A cylindrical MWPC and radial projection chamber for the E760 experiment, *Nuclear Instruments and Methods*, **A227** (1989)116–120.

[49] M. HASAN *et al.*, The Fermilab E760 Forward Electromagnetic Calorimeter, *Nuclear Instruments and Methods*, **A295** (1990)73.

[50] L. BARTOSZEK *et al.*, The E760 Lead Glass Central Calorimeter: Design and Initial Test Results, *Nuclear Instruments and Methods*, **A301** (1991)47–60.

[51] C. BOOTH *et al.*, Differences Between $\bar{p}p$ and pp Interactions at 8.8 GeV/c and Their Relationship to $\bar{p}p$ Annihilations, *Physical Review*, **D27** (1983)2015.

[52] K. BÖCKMANN *et al.*, Elastic Scattering, Pion Production, and Annihilation into Pions in Antiproton-Proton Interactions at 5.7 GeV/c, *Nuovo Cimento*, **A44** (1966)316.

[53] R. RAY, J. ROSEN, M. MASUZAWA, and J. ZHAO, A trigger for the Fermilab E760 lead glass calorimeter, *Nuclear Instruments and Methods*, **A307** (1991)254–264.

[54] K. E. GOLLWITZER, *The Charmonium $^1P_1$ State* (h_c) *Produced In Antiproton-Proton Annihilations*, PhD thesis, University of California, Irvine, 1993.

[55] J. E. FAST, *Two photon decays of charmonium states produced in proton-antiproton annihilations*, PhD thesis, University of California, Irvine, 1992.

[56] R. R. MIKA MASUZAWA, *A study of systematics at the η_c*. E760 internal memo, 1994. # 295.

[57] G. G. MCGRATH, *Conversions in the E760 inner detectors.* E760 internal memo, January 1994. No Number.

[58] G. GOVI *et al.*, *Determination of the $\pi^0\gamma$ cross section.* E760 internal memo, June 1992. No Number.

[59] G. ZIOULAS, *Measurement of the $\pi^0\pi^0$ and $\pi^0\gamma$ cross sections and contributions to $\gamma\gamma$ background.* E760 internal memo, April 1993. No Number. G. BLANFORD *et al.*, *Measurement of the $\pi^0\pi^0$ and study of the background.* E760 internal memo, March 1994. # 315.

[60] K. GOLLWITZER, *The CCAL shower Monte Carlo.* E760 internal memo, March 1994. # 312.

[61] J. OREAR, *Notes on statistics for physicists.* UCRL-8417, August 1958. Printed for the U.S. Atomic Energy Commission.

[62] R. BARLOW, Extended maximum likelihood, *Nuclear Instruments and Methods in Physics Research*, **A297** (1990)496–506.

[63] G. ZIOULAS. George was kind enough to do this study at Fermilab while putting the final touches on the CCAL Monte Carlo simulation.

[64] B. H. ONG, *Measurement of the Cross-Section for the Two-Photon Production of Proton Antiproton Pairs and Electron-Pion Separation with the Spaghetti Calorimeter*, PhD thesis, University of California, San Diego, 1993.

[65] CLEO COLLABORATION, *Measurement of the Cross-Section for $\gamma\gamma \to \bar{p}p$*, Tech. Rep. CLNS 93/1245, Cornell Electrion-positron Storage Ring, August 1993.

[66] EADIE, DRIJARD, JAMES, ROOS, and SADOULET, *Statistical Methods In Experimental Physics*, North-Holland Publishing Company, 1971ch. 11, 282–284.

[67] T. ARMSTRONG *et al.*, Proton Electromagnetic Form Factors in the Time-Like Region from 8.9 to 13.0 GeV^2, *Physical Review Letters*, **70** (1993)1212.

[68] J.ZHAO, *Analysis of alignment of H1 and H2.* E760 internal memo, February 1990. # 206.

[69] A. SMITH, *A measurement of* $\mathrm{br}(\psi' \to e^+e^-)$. E760 internal memo, July 1993. # 307.

[70] PRESS, FLANNERY, TEUKOLSKY, and VETTERLING, *Numerical Recipes, The Art Of Scientific Computing*, Cambridge University Press, 1986ch. 13, 476–484.

[71] V. FLAMINIO *et al.*, *Compilation of cross-sections III: p and $\bar{p}$ induced reactions*, Tech. Rep. CERN-HERA 84-01, CERN, April 1984.

[72] T. FIELDS *et al.*, Comparison Of New Data On $\bar{p}p \to \pi^+\pi^-$ And Other Two Meson States At 2.3GeV/c, *Physics Letters*, **40B** (1972)503–506.

[73] A. EIDE *et al.*, Elastic Scattering And Two-Body Annihilations At 5GeV/c, *Nuclear Physics*, **B60** (1972)173–220.

[74] T. BURAN *et al.*, Antiproton-Proton Annihilation Into $\pi^+\pi^-$ And K^+K^- At 6.2GeV/c, *Nuclear Physics*, **B116** (1976)51–64.

[75] S. J. BRODSKY, *Probing QCD in low energy $\bar{p}p$ collisions*, Tech. Rep. SLAC-PUB-4010, Stanford Linear Accelerator Center, Stanford University, Stanford, CA, 94305, June 1986.

[76] PARTICLE DATA GROUP, Review of Particle Properties, *Physical Review*, **D50** (1994).

[77] T. ARMSTRONG *et al.*, Measurement of the J/ψ and ψ' Resonance Parameters in $\bar{p}p$ Annihilation, *Physical Review*, **D47** (1993)772.

[78] L. HAND, D. MILLER, and R. WILSON, Electric and Magnetic Form Factors of the Nucleon, **35** (1963)335.

[79] V. CHERNYAK, A. OGLOBLIN, and I. ZHITNITSKY, Wave Functions of Octet Baryons, *Soviet Journal of Nuclear Physics*, **48** (1988)536.